RSC Advances

REVIEW

View Article Online
View Journal | View Issue

Cite this: *RSC Adv.*, 2023, **13**, 30798

Comprehensive review of micro/nanostructured $ZnSnO_3$: characteristics, synthesis, and diverse applications

Moksodur Rahman,[ab] Muhammad Shahriar Bashar,[b] Md. Lutfor Rahman[b] and Faisal Islam Chowdhury*[a]

Received 12th August 2023
Accepted 14th September 2023

DOI: 10.1039/d3ra05481k

rsc.li/rsc-advances

Generally, zinc stannate ($ZnSnO_3$) is a fascinating ternary oxide compound, which has attracted significant attention in the field of materials science due to its unique properties such high sensitivity, large specific area, non-toxic nature, and good compatibility. Furthermore, in terms of both its structure and properties, it is the most appealing category of nanoparticles. The chemical stability of $ZnSnO_3$ under normal conditions contributes to its applicability in various fields. To date, its potential as a luminescent and photovoltaic material and application in supercapacitors, batteries, solar cells, biosensors, gas sensors, and catalysts have been extensively studied. Additionally, the efficient energy storage capacity of $ZnSnO_3$ makes it a promising candidate for the development of energy storage systems. This review focuses on the notable progress in the structural features of $ZnSnO_3$ nanocomposites, including the synthetic processes employed for the fabrication of various $ZnSnO_3$ nanocomposites, their intrinsic characteristics, and their present-day uses. Specifically, we highlight the recent progress in $ZnSnO_3$-based nanomaterials, composites, and doped materials for their utilization in Li-ion batteries, photocatalysis, gas sensors, and energy storage and conversion devices. The further exploration and understanding of the properties of $ZnSnO_3$ will undoubtedly lead to its broader implementation and contribute to the advancement of next-generation materials and devices.

1. Introduction

The creation and fabrication of materials at the nanoscale have witnessed a significant breakthrough in the 21st century, revolutionizing numerous industries, including photocatalysis, energy storage and conversion systems, biosensors, and biological applications. Binary metal-oxides, such as TiO_2, ZnO, and SnO_2, which are known for their favourable optical and electrical properties, have been extensively investigated and widely applied in various sectors, such as photovoltaic devices,[1] thin-film displays,[2] electrochromic systems,[3] and gas sensing technologies.[4] Nevertheless, the practical application of these materials is impeded by their poor thermal and chemical stability when exposed to different environments.

Accordingly, to overcome this limitation and improve their characteristics, researchers are actively engaged in the development of ternary oxides, such as $ZnSnO_3$ and In–Zn–O.[5–7] Among them, nanostructures of $ZnSnO_3$ (various nano shapes, such as wires, rods, rings, tubes, cubes, and spheres) have attracted considerable interest owing to their advantageous chemical sensitivity, wide energy bandgap, high transmittance percentage, electron mobility, low price, non-toxicity, and earth abundance.[5,8–13] The performance of energy storage devices and catalysis is greatly affected by the morphology, structure, and physical characteristics of the active electrode materials. Furthermore, LN-type $ZnSnO_3$, which possesses a high spontaneous polarization (theoretical value $P_r \approx 59\ \mu C\ cm^{-2}$), has been experimentally observed in epitaxial thin films with a value of $P_r \approx 47\ \mu C\ cm^{-2}$.[14] These films demonstrate superior photocatalytic activity and exhibit piezoelectric properties.

$ZnSnO_3$ possesses remarkable morphological properties, making it an attractive material with diverse energy and biological applications. The synthesis and fabrication techniques employed greatly influence the morphological characteristics of $ZnSnO_3$. Various factors, such as the capping agent, surfactant, reaction temperature, annealing temperature, concentration of metal precursors, and reaction time, play a crucial role in the development of different synthetic processes.[15–17] Researchers have reported the synthesis of well-organized $ZnSnO_3$ nanopowders, composites, and films using a range of methods. These methods include solid-state,[18] sol–gel,[19,20] ion-exchange,[21] high temperature calcination,[22,23] thermal evaporation,[24,25] magnetron sputtering,[26–29] hydrothermal process,[8,12] laser ablation,[30] and vapor deposition.[31] The different crystal structures of $ZnSnO_3$, such as that with the $Pm\bar{3}m$, $R\bar{3}$, and $R3c$ space groups, have been extensively investigated. The perovskite structure (with the $Pm\bar{3}m$

---

[a] Department of Chemistry, University of Chittagong, Chattogram, Bangladesh. E-mail: faisal@cu.ac.bd

[b] Bangladesh Council of Scientific and Industrial Research (BCSIR), Dhaka, Bangladesh

space group) of $ZnSnO_3$, together with its face-centred cubic and orthorhombic phases can be achieved through the calcination of various $ZnSn(OH)_6$ precursors. Recent studies have focused on the advancements in $ZnSnO_3$ nanostructures for energy and biological applications. However, considering the limited literature to date on this subject, the present review serves as a necessary contribution to bridge the knowledge gap.

This review presents the latest progress in the field of $ZnSnO_3$-based nanomaterials, composites, and doped materials, focusing on their application in the key areas of energy and biology. $ZnSnO_3$-based materials have attracted significant interest due to their potential application in energy storage and conversion technologies, such as lithium/sodium-ion batteries and dye-sensitized solar cells. Additionally, they demonstrate promising prospects as catalysts for the removal of dye/organic pollutants and as gas sensors for various biological uses. This review provides comprehensive insights into the advancements and potential of $ZnSnO_3$-based materials in these specific domains.

2. Crystal structure and physical properties

$ZnSnO_3$ exhibits various types of crystal structures, including perovskite, ilmenite, $LiNbO_3$-type, $CdSnO_3$-type, $HgSnO_3$-type, and post-perovskite with the $Pm\bar{3}m$, $R\bar{3}$, $R3c$, $Pnma$, $R3c$, and $Cmcm$ space groups, respectively, which are all feasible.

$ZnSnO_3$ with the $Pm\bar{3}m$, $R\bar{3}$, and $R3c$ space groups has been the subject of numerous study. The perovskite structure (with $Pm\bar{3}m$ space group) of $ZnSnO_3$ includes face-centred cubic (FCC) and orthorhombic phases, which is typically synthesized by annealing different $ZnSn(OH)_6$ precursors. In terms of surface energy, $ZnSnO_3$ crystals with an FCC structure generally exhibit the order of (111) < (100) < (110). This demonstrates that the normal surfaces of $ZnSnO_3$ crystals tend to exhibit (111) facets, while facets with higher surface energies such as {100} or {110} may not appear during realistic thermodynamic growth processes.[32]

Zinc tin oxide/zinc stannate occur in two individual oxides with distinct crystal structures and varying Zn/Sn ratios. These oxides are known as orthorhombic or perovskite $ZnSnO_3$ and cubic spinel-type Zn_2SnO_4.[33] Based on the available data, Zn_2SnO_4 demonstrates higher thermal stability compared to $ZnSnO_3$. Zn_2SnO_4 possesses a cubic spinel arrangement, which has been previously established as the most thermodynamically stable form. Alternatively, $ZnSnO_3$ is formed under non-equilibrium conditions, such as high pressure, suggesting its thermodynamic metastability as a crystal phase. The formation of metastable $ZnSnO_3$ requires high pressure and energy conditions. The phase transition from metastannate to orthostannate begins at approximately 500 °C, with an activation energy of around 0.965 eV. Subsequently, recrystallization occurs, leading to the formation of the orthostannate phase with an inverse spinel structure, which is typically observed at around 750 °C. This investigation provides valuable insights into the behaviour of perovskite $ZnSnO_3$ undergoing a phase change to inverse spinel Zn_2SnO_4 during calcination.[33]

Moksodur Rahman received his Master's Degree in Physical Chemistry from the University of Chittagong, Bangladesh in 2020. Currently, he holds the position of Postgraduate Research Fellow at the Bangladesh Council of Scientific and Industrial Research (BCSIR). His research focuses on creating innovative nanocomposites tailored for various applications, such as humidity sensing, catalysis, and nanopigments. He looks forward to embracing the exciting challenges and opportunities that the future holds.

Dr Faisal Islam Chowdhury obtained M.Sc. in Chemistry with 1st class first position. He awarded two Ph.D. degrees (Ph.D. in Experimental Physics from University of Malaya in 2018 and Ph.D. in Chemistry from University of Chittagong in 2010 for his pioneering works on ionic liquid doped noble gel polymer electrolytes applied to dye-sensitized solar cells and molecular interaction in binary liquid mixtures, respectively. He has more than 17 years of experience in teaching and research. He is currently a Professor of Chemistry at University of Chittagong. He worked as a Visiting Research Fellow at Center for Ionics, Department of Physics, University of Malaya, Malaysia in 2019. In 2022, Dr Chowdhury completed CW-LSE on LQM course at VERIFIN, Helsinki University, Finland. He awarded Best Presenter Award in ISMAI 2016, Kuala Lumpur, Malaysia and Research Excellence award 23 in High Impact Factor Journal Publication, Research Festival, University of Chittagong. Also, he established Nanotechnology, Renewable Energy and Catalysis Laboratory (NRCL) and ACS Student Chapter, University of Chittagong Bangladesh and is serving as PI and faculty advisor, respectively. His areas of expertise cover Dye-sensitized solar cells (DSSC), Nanotechnology, Li-ion battery, Polymer electrolytes, Computational Chemistry, Solution chemistry. Dr Chowdhury has successfully undertaken numerous research projects funded by prestigious institutions such as the University of Malaya, Malaysia, University of Chittagong, Bangladesh, University Grants Commission (UGC), Bangladesh, Ministry of Science and Technology, Bangladesh, and the American Chemical Society, USA. He published 37 articles and 10 book chapters. He has published 40 research/review articles in high-impact ISI/Scopus-cited Journals and 10 book chapters published by Elsevier/Woodhead Publishing. He has total citations of 566, h-index of 14, and i10-index of 16.

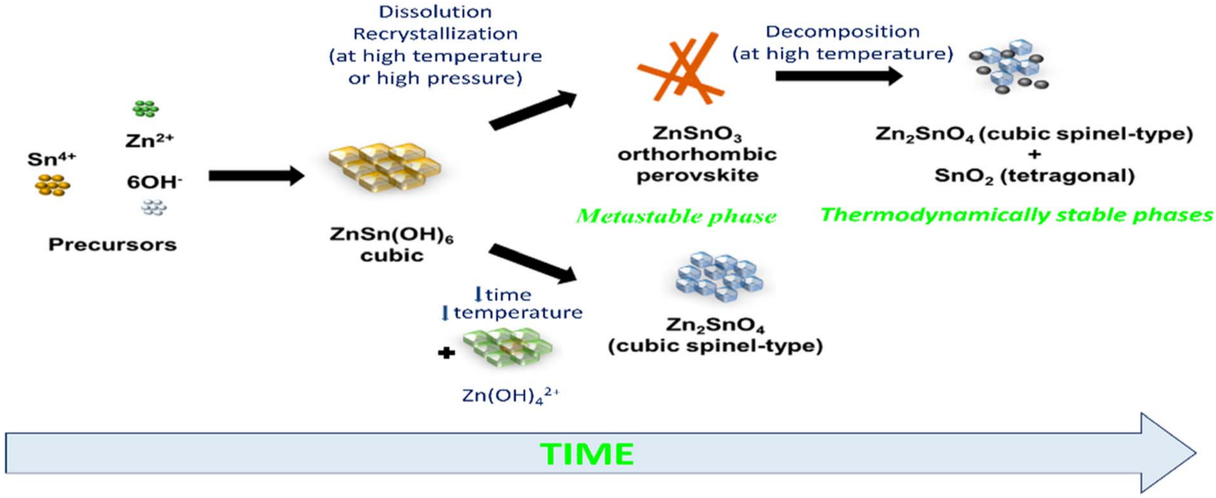

Fig. 1 Schematic illustration of phase rearrangements during the hydrothermal process of zinc stannate nanostructures as a function of reaction energy and synthesis time.[34]

Previous studies have indicated that metastable $ZnSnO_3$ structures tend to degrade at temperatures exceeding 500 °C. However, Rovisco *et al.* demonstrated that breakdown can take place at much lower temperatures (*e.g.*, 220 °C for 24 h) or longer reaction durations (*e.g.*, 200 °C for 36 h) because of the high energy involved in the hydrothermal technique.[34] This underscores the benefits of utilizing hydrothermal techniques to acquire metastable nanostructures composed of multiple components, such as $ZnSnO_3$, at reduced temperatures. It also underscores the requirement of carefully managing and comprehending all aspects of fabrication to attain the targeted structures successfully. The growth mechanisms of nanostructures throughout the reaction period pose a significant challenge in the synthesis of nanomaterials. Particularly, in the case of fabricating $ZnSnO_3$ nanowire, the metastable nature of this phase adds complexity to its complete comprehension.[34] By increasing the reaction time and overall energy available, the development of nanostructures and their corresponding phases can be observed, which is primarily due to the meticulous optimization of the physio-chemical parameters employed in this study. Their primary objective was to generate $ZnSnO_3$ nanowires, but the formation of Zn_2SnO_4 nanostructures was also observed, particularly under the conditions of very short synthesis durations, lower temperatures, and smaller reaction volumes. This observation implies that the formation of Zn_2SnO_4 requires comparatively less energy. The aforementioned procedure is illustrated in Fig. 1.

The $LiNbO_3$-type configuration (*R*3*c*) is distinguished by the substantial displacement of Zn atoms, which is caused by the robust covalent bonds formed between Zn and three oxygen atoms. This bonding configuration gives rise to piezoelectric, ferroelectric, pyroelectric, and non-linear optical properties. The crystal lattice of $ZnSnO_3$ in the LN-type arrangement, as depicted in Fig. 2a, is comprised of interconnected octahedral units. Interlocking occurs between the Zn octahedra, where each octahedron shares its corners with another octahedron of the same type. Similarly, Sn octahedra exhibit corner sharing, forming connections with other Sn octahedral structures. The cation arrangement follows a pattern of Sn–Zn-vacancy-Sn-Zn-vacancy-Sn, aligned along the *z*-axis. In $ZnSnO_3$, the bond valence sums for Zn, Sn, and O were calculated to be 1.79, 4.08, and 1.96, respectively. Notably, the Zn–O bond in $ZnSnO_3$ is found to be under-bonded compared to the ideal values. The Sn–O distances in $ZnSnO_3$ were observed to be 0.2005 nm (×3) and 0.2094 nm (×3), deviating from the distances typically observed in perovskite-type stannates, which feature SnO_6 octahedra.[35]

Fig. 2b illustrates the presence of two octahedral structures, where one is composed of ZnO_6 and the other SnO_6. The SnO_6 and ZnO_6 octahedra are connected to the neighbouring octahedra through shared edges and faces. Fig. 2c illustrates a single ZnO_6 and SnO_6 cluster. The Zn–O bonding lengths consist of three long bonds (approximately 0.2308 nm) on the upper side and three short bonds (approximately 0.2040 nm) on the bottom side, which are labelled as la and lb in the ZnO_6 cluster, respectively. The Sn–O bonding lengths in the SnO_6 cluster, labelled as lc and ld, consist of three short bonds (approximately 0.2008 nm) on the upper side and three long bonds (approximately 0.2093 nm) on the lower side. Fig. 2d shows individual clusters of ZnO_6 and SnO_6, highlighting the variation in bonding length along the *z*-axis. In the ZnO_6 cluster, the Zn ion exhibits a displacement (δ_{Zn}) of 0.5 Å, while in the SnO_6 cluster, the Sn ion has a displacement (δ_{Sn}) of 0.2 Å. Along the *z*-axis, the Zn ion experiences a larger displacement than the Sn ion, resulting in the creation of spontaneous polarization, which is the origin of piezoelectricity in this material.[36,37]

In ref. 38 and 39, density functional theory (DFT) and the extended gradient estimation were employed to investigate the structural, electrical, and optical properties of $ZnSnO_3$. The analysis of the electronic structures revealed that $ZnSnO_3$ is a semiconductor characterized by a direct band gap of 1.0 eV. The examination of the optical spectra revealed that inter-band

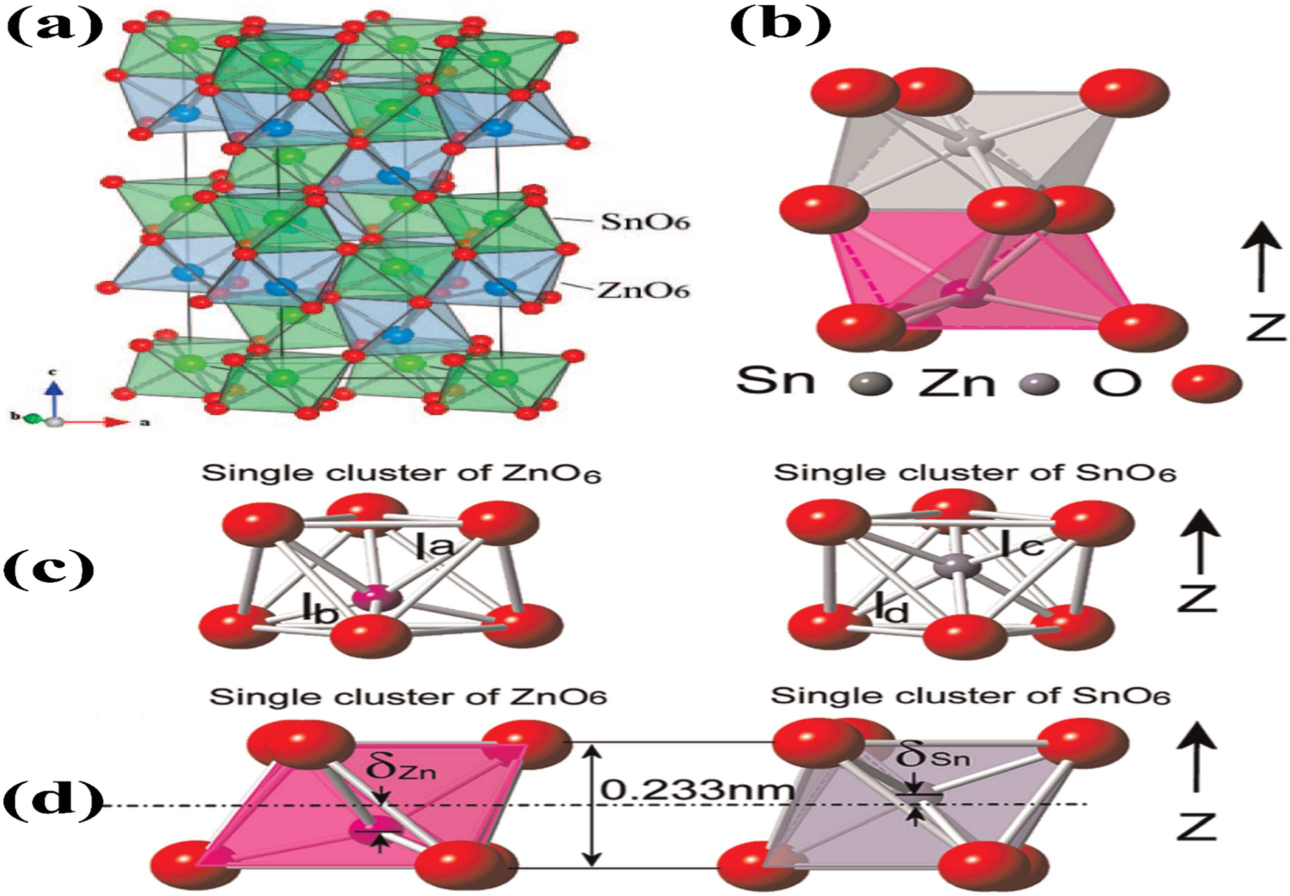

Fig. 2 (a) Crystal structure of $ZnSnO_3$ is visualized in a three-dimensional image, revealing the arrangement of atoms in an octahedral framework [reprinted with permission from *J. Am. Chem. Soc.* 2008, **130**, 21, 6704–6705. Copyright 2008, the American Chemical Society]. (b) Lower side of the structure consists of ZnO_6 octahedra, while the upper side is formed by SnO_6 octahedra. (c) Separate and distinct clusters of ZnO_6 and SnO_6. (d) Displacement of Zn ions (δ_{Zn}) and Sn ions (δ_{Sn}) from their equilibrium positions along the *z*-axis causes a variation in the bonding length between oxygen (O) and Zn (O–Zn–O) or Sn (O–Sn–O) atoms, respectively.[48]

transitions occur in the $ZnSnO_3$ compound. These transitions occur between the O 2p levels in the valence band (VB) and either the Sn 5s level or the higher CB Zn 3d levels in the lower energy level. Additionally, inter-band transitions were observed between the O 2p levels and either the Sn 5p or Zn 4p conduction bands (CB) in the higher energy level. These transitions contributed to the computed optical spectra.

Dielectric properties are also crucial properties for the application of nanoparticles as dielectric materials.[40–42] $ZnSnO_3$ materials display excellent electromagnetic wave attenuation characteristics and a wide frequency range, making them suitable for various applications such as ground-penetrating radar systems, microwave absorbers, communication systems, and energy storage devices.[43–45] To obtain the real (ε_1) and imaginary (ε_2) part of the dielectric constant, the Kramers–Kronig equation was utilized.[46] Given that $ZnSnO_3$ possesses a hexagonal shape, the evaluation was focused on incoming light polarized along the [1 0 0] and [0 0 1] crystallographic axes. They observed that there was no significant anisotropy in both the real and imaginary parts of the equation. The peaks in ε_2 were associated with electron excitation. Furthermore, the computed static dielectric constant, $\varepsilon_1(0)$, of $ZnSnO_3$ along the [1 0 0] and [0 0 1] directions was determined to be 4.05 and 3.96 eV, respectively.[39] These results are significantly lower than that of $BaTiO_3$ (5.12) and $PbZrO_3$ (5.34), indicating the distinct dielectric behaviour of $ZnSnO_3$ compared to these materials.[47]

$ZnSnO_3$ also exhibits superior ferroelectric properties. Shin *et al.* conducted research on the ferroelectric characteristics of $ZnSnO_3$.[49] They examined the hysteresis loop of a $Pt/ZnSnO_3/SrRuO_3$ capacitor at a measurement frequency of 10 kHz to investigate its ferroelectric properties. This exhibited a coercive electric field of 130 kV cm^{-1} and improved remnant polarization of 47 C cm^{-2} ($2P_r$ of 94 C cm^{-2}). The epitaxial $ZnSnO_3$ demonstrated a saturation polarization of 58 C cm^{-2}, which was marginally higher than the residual polarization. This observation suggests the presence of a well-formed crystalline structure in the material. To gain a deeper understanding, they investigated the hysteresis loops across a range of frequencies. This analysis aimed to examine the behaviour of the capacitor at various frequency regimes. As depicted in Fig. 3a, the coercivity increased gradually as the measurement frequency increased. Additionally, a square pulse with a voltage of 5 V was employed

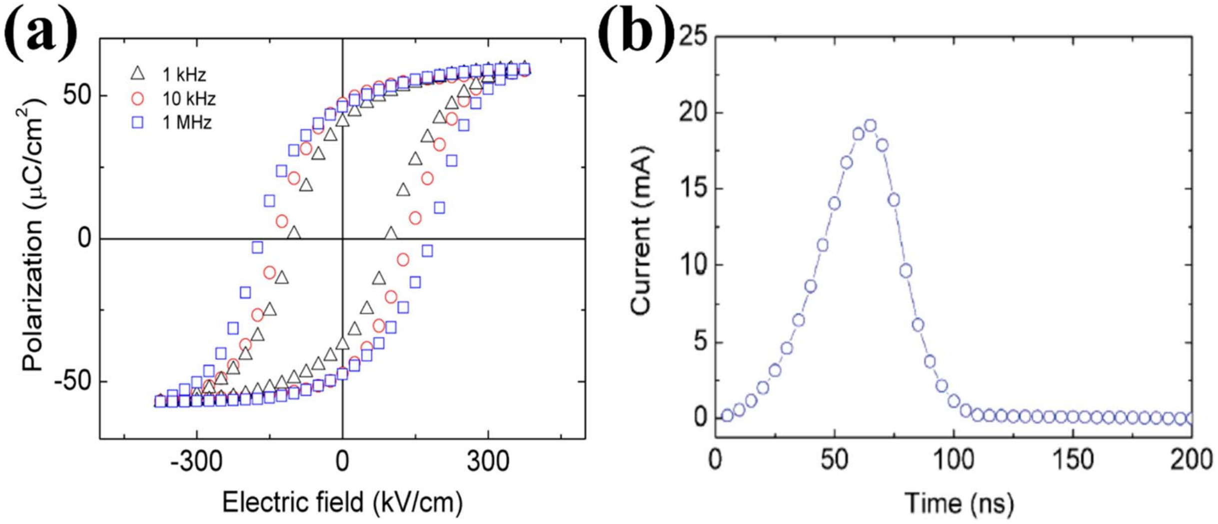

Fig. 3 (a) Hysteresis loops of the Pt/$ZnSnO_3$/$SrRuO_3$ capacitor observed at different measurement frequencies. (b) Switching-current as a bias of 5 V. The fast-switching behaviour is within 100 ns.[49]

to evaluate the switching current. The switching behaviour was found to be rapid, with a fast-switching time of 100 ns, as shown in Fig. 3b. This indicates that the capacitor can transition between states efficiently and quickly.

To model the interactions between ions and electrons, projector expanded wave potentials were employed, considering the effects of both ions and electrons.[49] The exchange and correlation energies of the electrons were calculated using a local density approximation, providing insights into their behaviour in the system. The estimated lattice constants were $a = 5.24$ Å and $c = 13.88$ Å per formula unit cell, with a cell volume of 54.92 Å. Fig. 4 presents the measurements of the deviations of Zn and Sn ions from the oxygen octahedral core. The data revealed that the rearrangement of the A cation (Zn) was 0.55 Å, which exceeds the rearrangement of the B cation (Sn) at 0.21 Å. This disparity can be attributed to the larger available space in the A site, facilitating greater movement for the Zn atom. The difference in rearrangement arises from the fact that Zn, which has a covalent radius of 1.31 Å, is smaller in size compared to Sn, with a covalent radius of 1.41 Å.[49] Employing the Berry phase technique, a polarization value of 60 C cm^{-2} was determined along the pseudo cubic[109] direction. This value closely matches both their experimental findings and the results obtained from analytical measurements based on the ionic rearrangements and atomic valences.

The preferred ground-state structure of $ZnSnO_3$ was found to be the LN-type ($LiNbO_3$-type) phase, given that it exhibits a lower total energy compared to the IL-type (ilmenite-type) structure. The energy difference between the LN and IL phases is merely 0.09 eV per unit of formula, indicating the potential occurrence of a structural shift from the LN to the IL when exposed to high pressure or temperature. However, investigations by Gao *et al.* revealed that the total energy–volume curves of the LN and IL phases do not cross when subjected to compression, indicating that the structural transition is unlikely to occur under high pressure.[39]

Fig. 5a illustrates the calculated E–V curves for different structures. When $T = 0$ K, the LN structure exhibits the lowest total energy among the feasible structures. Alternatively, the cubic perovskite structure has a considerably higher total energy, with a difference of up to 3.76 eV per formula unit compared to the LN-type structure. This substantial energy variation implies that the formation of the cubic perovskite phase of $ZnSnO_3$ is challenging to achieve under normal conditions. Additionally, the combined energy of the $CdSnO_3$-type phase crosses paths with both the IL and LN phases, indicating the possibility of structural changes in severe settings.[50–52]

Moreover, Fig. 5b illustrates the evaluation of the total energy variation in $ZnXO_3$ compounds (where, X = Si, Ge, Sn, and Pb) between the IL and LN structures. The results indicate a monotonic decrease in the total energy difference moving from Si (0.60 eV) to Ge (0.37 eV) to Sn (0.09 eV) phases, proposing that the IL phase is strenuously more favourable than the LN phase for these elements. However, for the Pb-containing phase, the LN phase is more energetically favourable than the IL phase. In the range where the zero-point energy (ZPE) correction becomes significant for assessing the relative structural stability, the overall energy gap between $ZnSnO_3$ in ionic liquid (IL) and layered perovskite (LN) forms is comparatively insignificant. The ZPE calculated from the partial density of states (PDOS) was found to be 0.23 eV per unit for the IL-type structure and 0.31 eV per unit for the LN structure. When accounting for ZPE, the overall energy gap between the IL and LN structures is approximately 0.005 eV per unit. This implies that there is a possibility for these two phases to exist together under normal environmental conditions.[50,53–55]

The lattice parameters of a semiconductor are typically affected by multiple parameters, as follows:[56–59] (i) the concentration of free electrons, which affects the deformation

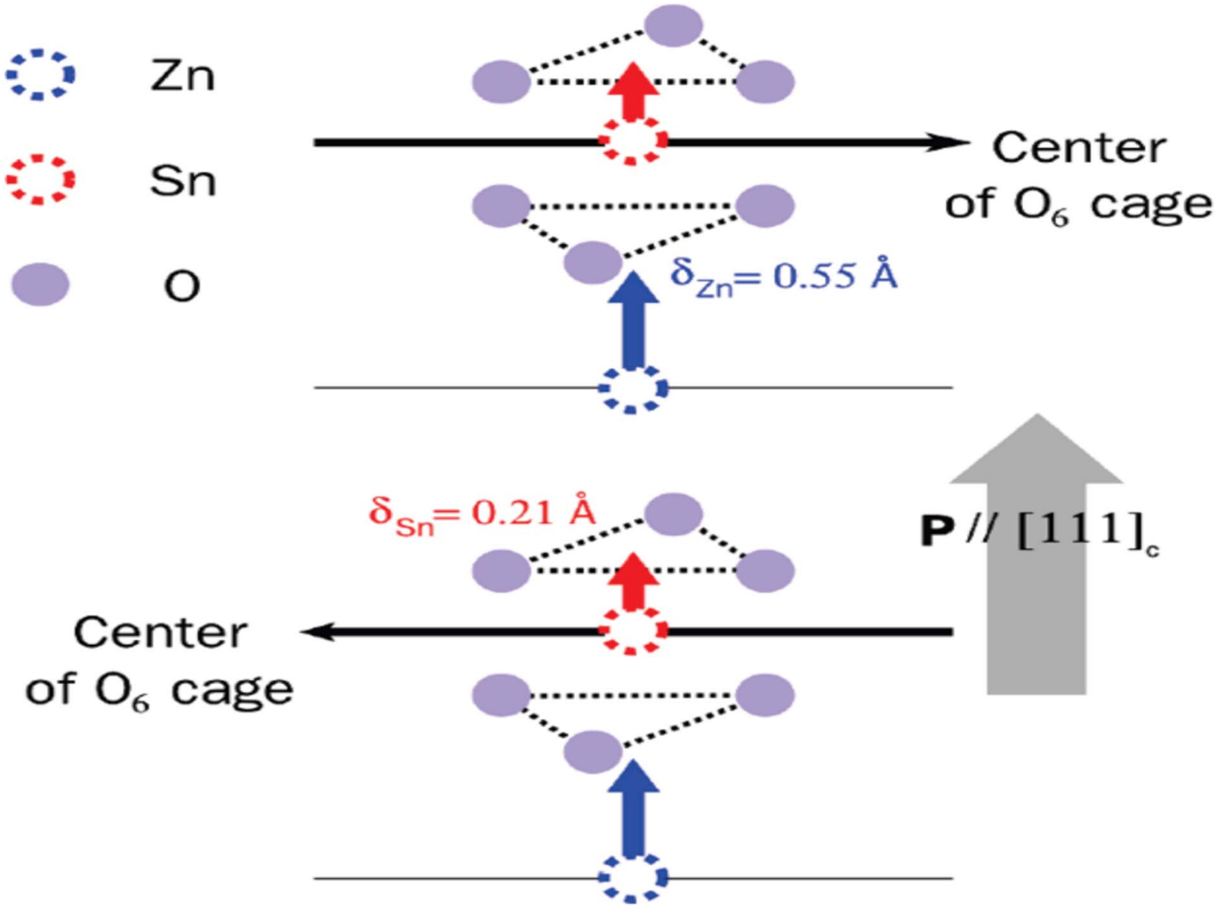

Fig. 4 Ionic rearrangements of Zn and Sn in the *R*3*c* phase of $ZnSnO_3$.[49]

potential of the conduction-band minimum occupied by these electrons, (ii) the concentration of foreign atoms and defects and their difference in ionic radius compared to the host matrix ion, (iii) external strains caused by factors such as substrate-induced stress, and (iv) temperature. To accurately determine the lattice parameters of a crystalline material, high-resolution X-ray diffraction (HRXRD) is commonly employed. The bond method is utilized with a combination of symmetrical and asymmetrical reflections to measure and analyse the lattice parameters.[60–63] In the case of $ZnSnO_3$, the calculated lattice parameters are provided in Table 1.

In ref. 50, the formation enthalpy [$\Delta H = E_{\text{total}}(\text{ZnSnO}_3) - \{E_{\text{total}}(\text{ZnO}) + E_{\text{total}}(\text{SnO}_2)\}$] was estimated to gain insights into the impact of different synthesis pathways in experiments. The calculated formation enthalpies for all the proposed $ZnSnO_3$ phases are positive, as shown in Table 1. This indicates that $ZnSnO_3$ is not energetically favourable and cannot be produced through solid-state fabrication pathways such as combining ZnO and SnO_2 under normal environmental conditions. However, experimental evidence suggests that these polymorphs have the potential to remain stable when subjected to extreme conditions, such as elevated pressure and temperature. To comprehend the structural transition of $ZnSnO_3$, the enthalpy variation between heterogeneous component oxides such as (ZnO + SnO_2), ((Zn_2SnO_4 + SnO_2)/2), IL- and LN-type phases was also estimated. This analysis is depicted in Fig. 5c and d). Below 5.9 GPa, the heterogeneous component oxides (h-ZnO + SnO_2) are more favourable than the various potential phases. In the range of 5.9 to 7.1 GPa, the heterogeneous component oxides of Zn_2SnO_4 + SnO_2 become increasingly favourable, aligning with experimental results at intermediate pressure levels. At low temperatures and >7.1 GPa, the LN-type $ZnSnO_3$ phase is more favourable than its constituent phases, which is consistent with experimental data, suggesting the formation of LN-type $ZnSnO_3$ at 7 GPa. At a pressure of 34.5 GPa, the LN-type phase undergoes a transition to the orthorhombic $CdSnO_3$-type phase, which is significantly higher than the transition pressures observed for $ZnGeO_3$ (15.6 GPa) and $MgGeO_3$ (17.9 GPa).[51,57,64]

Elastic constants are significant parameters that provide insight into the crystallite structure and bonding strength among atoms. In hexagonal structures such as $ZnSnO_3$, the elastic parameters exhibit positive values and adhere to the stability requirement outlined by Born–Huang, suggesting the elastic stability of both the LN and IL phases. Table 2 presents the elastic constants for various space groups.

The structural properties of $ZnSnO_3$ can be understood based on density functional theory (DFT) calculations. The $ZnSnO_3$ supercells used in the study consist of 60 atoms ($Zn_{12}Sn_{12}O_{36}$). The VB of $ZnSnO_3$ primarily consists of Zn $3d^{10}4s^2$ states, Sn $5s^25p^2$ states, and O $2s^2p^4$ states. Fig. 6a and

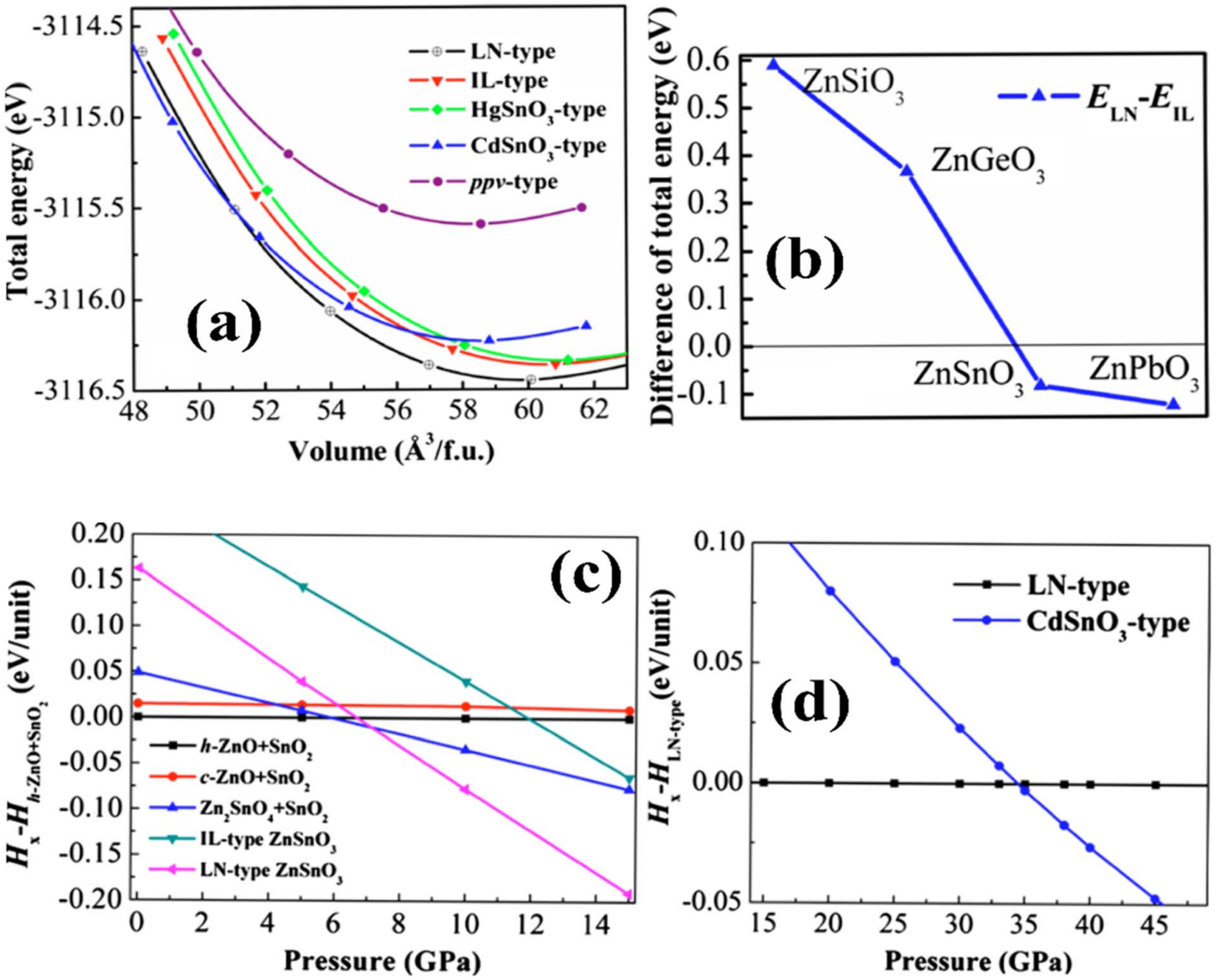

Fig. 5 (a) E–V curve for six feasible phases. (b) Energy variation in $ZnXO_3$. (c) Enthalpy variation among heterogenous component oxides. (d) Enthalpy variation in LN-type and $CdSnO_3$-type phases.[65]

Table 1 Previously reported lattice constants, total energy (ΔE), and heat of formation (ΔH) of $ZnSnO_3$ for various space groups

	Lattice constants					
Space group	a (Å)	b (Å)	c (Å)	ΔE (eV/f.u.)	ΔH_f (eV/f.u.)	Ref.
$R3c$	5.387(5.262)	14.344(14.003)	—	0	0.15	35 and 50
$R\bar{3}$	5.419(5.284)	14.384(14.091)	—	0.09	0.23	
$Pm\bar{3}m$	4.086	—	—	3.76	3.90	
$R\bar{3}c$	3.429	14.387	—	0.11	0.25	
$Pnma$	5.422	7.994	5.428	0.22	0.36	
$Cmcm$	3.082	9.934	7.653	0.85	1.00	

b illustrate the supercells and the determined density of states (DOS) and partial density of states (PDOS) of $ZnSnO_3$.[67]

The energy band at [−18.4, −15.3] eV in the VB is largely filled by O 2s states interspersed with few Sn 4d levels. The energy range of approximately [−8.1, −5.5] eV displays bands that can be attributed to the presence of Sn 5s states, together with a combination of O 2p and Zn 3d states. On the other hand, within the range of [−5.5, −3.4] eV, the dominating factor is the Zn 3d states, accompanied by O 2p states and a small contribution from Sn 5p states. At the upper end of the valence band ([3.4, 0] eV), the O 2p state takes precedence and dominates. However, it is accompanied by a mixture of Zn 3d and minor presence of Sn 4d states, suggesting substantial hybridization between these states. The Sn 5s and Zn 4s states dominate the CB area of [1, 5.5] eV, but Sn 5p dominates the Zn 4p state when the energy is more than 5.5 eV. For energies less than 5.5 eV, the Zn PDOS is minimal, and thus negligible. Consequently, the Sn 5s and O 2p states should control the electrical

Table 2 Elastic constants of $ZnSnO_3$ for various space groups

Space group	C_{11}	C_{12}	C_{13}	C_{14}	C_{15}	C_{22}	C_{23}	C_{33}	C_{44}	Ref.
$R3c$	310.4	137.1	100.8	1.4	—	—	—	175.3	77.3	66
$R\bar{3}$	268.8	132.8	78.8	14.7	14.3	—	—	185.9	2.6	
$Pm\bar{3}m$	284.4	74.1	—	—	—	—	—	—	33.8	
$Pnma$	290.8	103.8	116.7	—	—	247.9	100.4	273.3	74.7	
$Cmcm$	316.9	51.8	47.8	—	—	210.4	77.5	223.9	239.5	

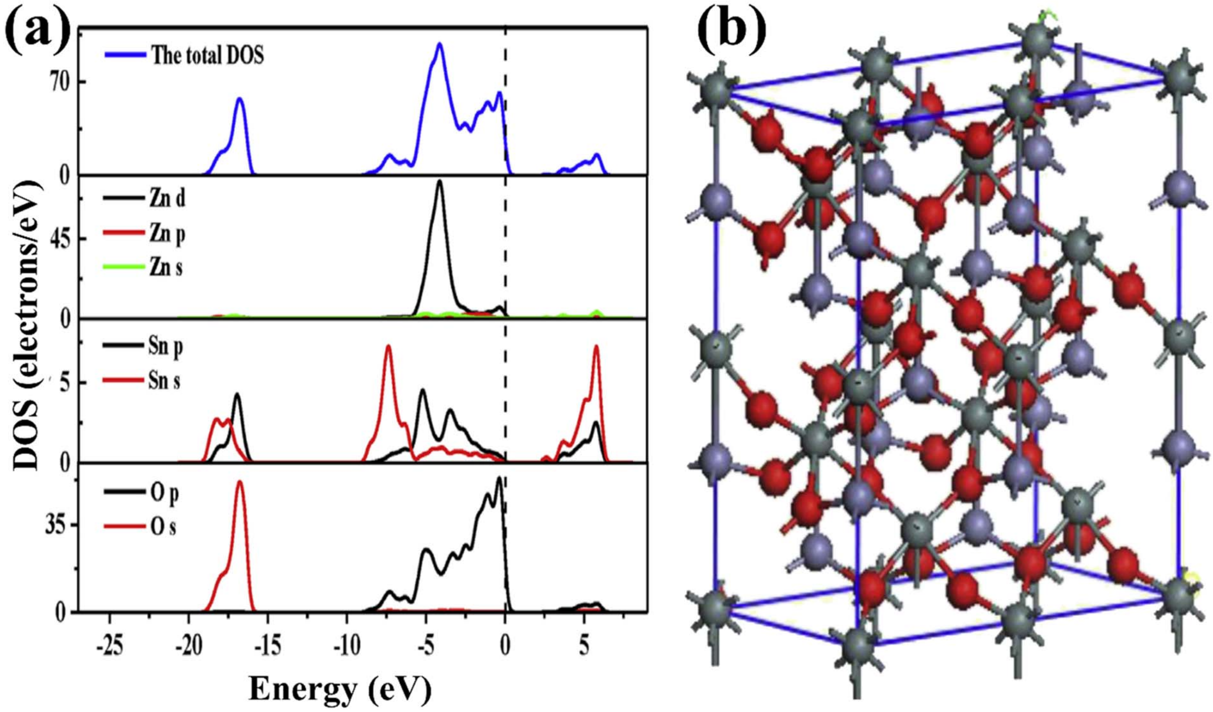

Fig. 6 (a) DOS and PDOS for $ZnSnO_3$. (b) Supercells of $Zn_{12}Sn_{12}O_{36}$.[69]

characteristics of $ZnSnO_3$. Both the top of the VB and the bottom of the CB are located at the Γ-point. Consequently, a direct band gap of 1.0 eV is generated, showing that $ZnSnO_3$ is a semiconductor. Due to the absence of an experimental band gap result for comparison, it is important to note that DFT often underemphasizes the energy gap of semiconductor solids.[67,68]

3. Synthesis technique/routes

Over the past few decades, several synthetic techniques have been employed to synthesize micro/nanostructures of $ZnSnO_3$. However, to achieve the controlled synthesis of these structures and expand their practical applications, it is crucial to comprehensively summarize the emerging growth mechanisms and develop new techniques. The two primary methods used for the synthesis of nanostructures are solution-based and vapor phase approaches. The size, crystal phase, and crystallinity of the synthesized materials significantly impact their band-gap energies and the separation of charge carriers in semiconductor oxides. Therefore, the quality of the synthetic conditions plays a key function in determining the efficiency of semiconductor oxides. Comparing with various synthesis routes, the solution-based procedure emerges as a simple and low energy-consuming technique for the production of $ZnSnO_3$ nanomaterials. By modifying the experimental factors such as solvent, precursor ingredients, and reaction environments, precise control of the nanostructure morphologies can be achieved. This straightforward technique also enables greater control of the particle size of nanostructures. The solution-based methods employed for the synthesis of $ZnSnO_3$ nanostructures include hydrothermal,[8,12] sol–gel,[19,20] precipitation,[70] electrochemical-deposition,[36] solvothermal,[71] microwave,[72] wet chemical, and electrospinning method.[73] Among the different methods available, the simple sol–gel process is particularly appealing for the synthesis of $ZnSnO_3$ nanocomposites. This method offers several advantages, including low cost, reliability, good repeatability, and the ability to easily control the physical properties and morphologies.[32]

The activity of $ZnSnO_3$ can be enhanced through the precise control of various factors, including band gap, size, morphology, crystal structure, surface area, stability, reusability, and preparation of composite materials. Among them, the crystal structure and specific surface area play a crucial role in improving the performance of $ZnSnO_3$. A significant parameter for achieving superior results is a large surface area, which is closely interconnected with the structure and mean particle size of the material. In the study by Yu *et al.*, they synthesized homogeneous $ZnSnO_3$ nanocubes using a low-temperature solution route.[74] They observed that decreasing the reaction temperature from 80 °C to 0 °C led to a decrease in the particle size of the fabricated $ZnSnO_3$ nanocubes from 600 nm to 40 nm, while the surface area increased from 36.4 to 109.5 $m^2\ g^{-1}$. The reduction in particle size resulted in an increase in the overall surface area of the material. A larger surface area provides more reactive sites, leading to higher surface reactivity, greater surface-to-volume ratios, and increased availability of surface-active sites.

Moreover, vapor phase techniques have also been used for the synthesis of nanostructured materials. These techniques include laser ablation,[75] vapour–liquid–solid,[37] thermal evaporation,[76] molecular beam epitaxy (MBE),[77] metal–organic chemical vapour deposition[78] and magnetron sputtering.[79] The choice of the method for the synthesis of $ZnSnO_3$ primarily relies on the desired dimensions of the nanostructures. The impact of various fabrication techniques and starting materials on the morphologies of $ZnSnO_3$ is presented in Table 3. Furthermore, in the application domain, the influence of the morphology of $ZnSnO_3$ on is efficiency has also been investigated.

3.1. Hydrothermal technique

Hydrothermal synthesis is a widely employed technique for the preparation of $ZnSnO_3$, utilizing a solution-based reaction approach. This method involves placing starting material dispersion in a sealed stainless-steel Teflon-lined autoclave. Subsequently, the autoclave is subjected to heating in an oven under precise temperature, duration, and autogenous pressure settings. The temperature typically ranges from 140 °C to 200 °C for the hydrothermal synthesis of zinc stannate.[80] The hydrothermal synthesis of $ZnSnO_3$ nanoparticles involves the use of different mineralizers such as ammonium hydroxide, sodium hydroxide, hexadecyl trimethyl ammonium bromide, various amines, and sodium carbonate. This leads to the creation of nanocrystals with different shapes (cubic, spherical, and rod like). Careful control of the chemical properties of the mineralizer is essential given that it influences the surface charges of the resulting metal oxides, which is critical

Table 3 $ZnSnO_3$ micro/nanostructure synthesis processes and morphologies

Material	Morphologies	Precursors	Method	Ref.
$ZnSnO_3$	Polyhedral	$Zn(Ac)_2\cdot 2H_2O$, CTAB/SDBS	Solution-based	32
$ZnSnO_3$	Nanocubes	$SnCl_4\cdot 5H_2O/Zn(Ac)_2\cdot 2H_2O$	HNO_3 etching	92
$ZnSnO_3$	Nanocubes	$SnCl_4\cdot 5H_2O/ZnSO_4$	Solution-based	74
$ZnSnO_3$	Hollow-cubes	$Zn(NO_3)_2/SnCl_4$	HCl etching	131
$ZnSnO_3$	Hollow-cages	$SnCl_2/Zn(Ac)_2\cdot 2H_2O$	Solution-based	132
$ZnSnO_3$	Hollow-cubes	$SnCl_4\cdot 5H_2O/ZnCl_2$	Solution-based	125
$ZnSnO_3$	Hollow-cages	$SnCl_4\cdot 5H_2O/Zn(Ac)_2\cdot 2H_2O$	Solution-based	127
$ZnSnO_3$	Face-centred trigonal	$Na_2SnO_3\cdot 3H_2O/Zn(NO_3)_2\cdot 6H_2O$	Sol–gel	99
$ZnSnO_3$	Polycrystalline ilmenite-type	$Zn(Ac)_2\cdot 2H_2O/SnCl_4\cdot 5H_2O$/ethylene glycol	Sol–gel	100
$ZnSnO_3$	Nanostructures	$ZnCl_2/SnCl_2$/Tepa/trimesic acid	Sol–gel	103
$ZnSnO_3$	Hollow cubes	$SnCl_4/ZnCl_2$	NaOH etching	133 and 134
$ZnSnO_3$	Nanoplates	$Zn(Ac)_2\cdot 2H_2O$, $SnCl_4\cdot 5H_2O$, ethanol, MEA	Sol–gel	135
$ZnSnO_3$	Hierarchical nanocages	$SnCl_4\cdot 5H_2O/Zn(Ac)_2\cdot 2H_2O$/NaOH, $(CH_2)_6N_4$	Hydrothermal	128
$ZnSnO_3$	Hollow microspheres	$SnCl_4\cdot 5H_2O/Zn(Ac)_2\cdot 2H_2O$/NaOH, CTAB	Hydrothermal	126
$ZnSnO_3$	Nanocages	$SnCl_4\cdot 5H_2O/Zn(Ac)_2\cdot 2H_2O$/NaOH, $(CH_2)_6N_4$	Hydrothermal	136
$ZnSnO_3$	Nanocubes	$Zn(Ac)_2\cdot 2H_2O/SnCl_4\cdot 5H_2O$, NaOH	Hydrothermal	137
$ZnSnO_3$	Nanowires	$ZnCl_2/SnCl_4\cdot 5H_2O$/PEG (200)	Hydrothermal	138
$ZnSnO_3$	Nanowires	$Zn(Ac)_2\cdot 2H_2O/SnCl_4\cdot 5H_2O$/NaOH, PEG (4 K)	Single-step hydrothermal	91
$ZnSnO_3$	Nanowires	$ZnO/SnCl_4\cdot 5H_2O$/PEG (10 K)	Hydrothermal	139
$ZnSnO_3$	Nanocubes	$SnK_2O_3\cdot 3H_2O/ZnC_4H_6O_4\cdot 2H_2O$/urea	MA hydrothermal	72
$ZnSnO_3$	Nanocubes	$ZnSO_4\cdot 7H_2O/Na_2SnO_3\cdot 3H_2O$	Ionic substitution	140
$ZnSnO_3$	Nanobelts/microbelts	Zn and Sn powder/graphite powder	Vapour–liquid–solid	36
$ZnSnO_3$	Triangular-belts	Zn and Sn/graphite powder	Vapour–liquid–solid	37
$ZnSnO_3$	Nanosheets	$Na_2SnO_3\cdot 3H_2O/Zn(Ac)_2\cdot 2H_2O$/ethylene glycol	Solvothermal	71
$ZnSnO_3$	Hollow cubes	$ZnCl_2$, $SnCl_4\cdot 5H_2O$/sodium citrate/NaOH	Coprecipitation	116
$ZnSnO_3$	Solid/hollow microspheres	$Zn(NO_3)_2\cdot 6H_2O/SnCl_4\cdot 5H_2O$/NaOH	Precipitation	70
$ZnSnO_3$	Nano-urchins	Zinc plate/$ZnO_x(OH)_y/NH_3$	Laser ablation	75
$ZnSnO_3$	Amorphous	ZnO/SnO_2	Magnetron sputtering	79, 141 and 142
Ag–$ZnSnO_3$	Hollow cubes	$ZnCl_2/SnCl_4\cdot 5H_2O$/sodium citrate/$Zn(NO_3)_2\cdot 6H_2O$	Coprecipitation	143
CDs-$ZnSnO_3$	Nanocubes	$SnCl_4\cdot 5H_2O/ZnSO_4\cdot 7H_2O$/CDs powder	Precipitation–calcination	144
$ZnSnO_3$/rGO	Nanocubes	$ZnSO_4\cdot 7H_2O/SnCl_4\cdot 5H_2O$/PDDA/GO	Coprecipitation	145 and 146
S-$ZnSnO_3$	Hollow cubes	$Zn(NO_3)_2\cdot 6H_2O$, $Na_2SnO_3\cdot 4H_2O$, $C_4H_6N_2$, CH_3CSNH_2	Ion-exchange	147
$ZnSnO_3$/rGO	Nanosheets	$Zn(NO_3)_2\cdot 6H_2O/SnCl_2\cdot 2H_2O$/GO	Thermal decomposition	76
$ZnSnO_3$/C	Nanofibers	$SnCl_2\cdot 2H_2O/ZnCl_2$/DMF/PVP	Electrospinning	73

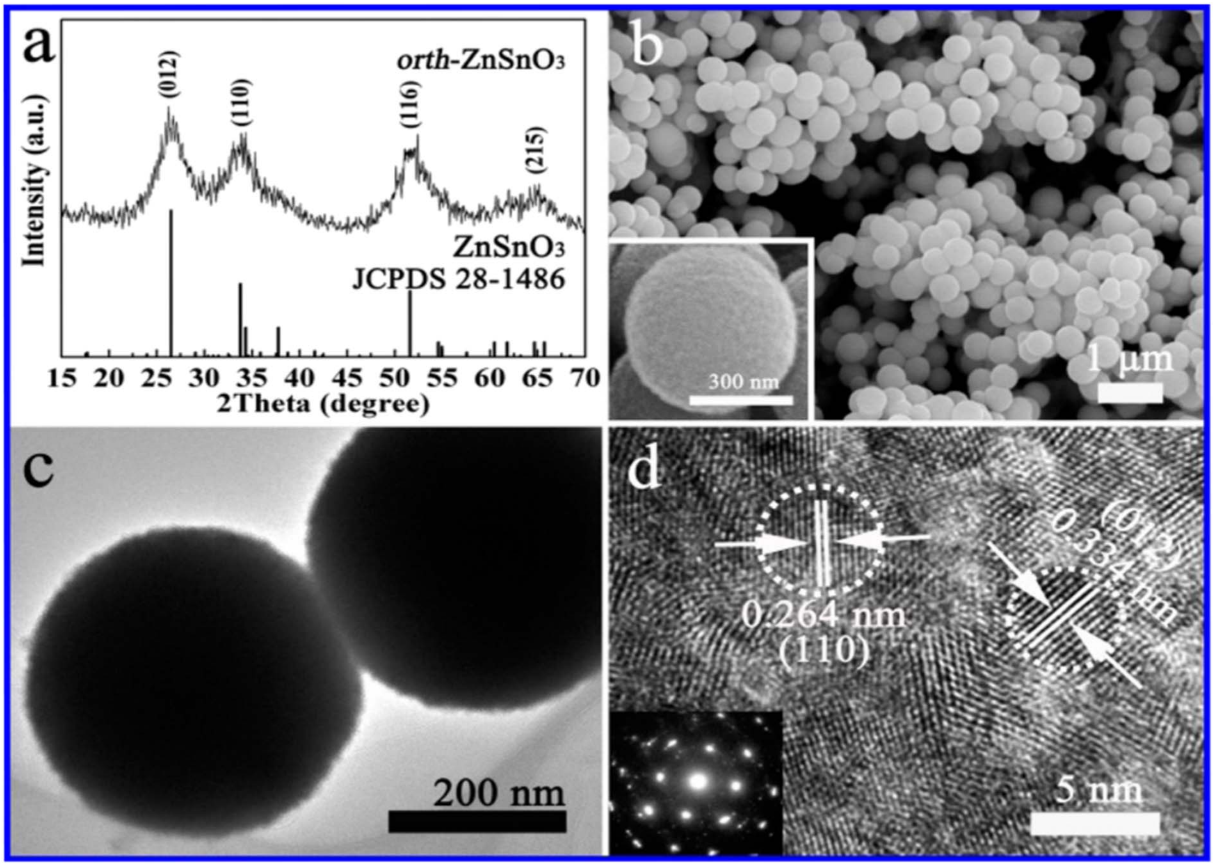

Fig. 7 (a) XRD pattern, (b) SEM image, (c) TEM image, and (d) HRTEM image of $ZnSnO_3$ solid microspheres.[90]

for the formation of nanoparticles in the hydrothermal synthesis process.[81–85]

In hydrothermal fabrication of $ZnSnO_3$, the compositions of synthesized nanomaterials can be precisely controlled through liquid-phase or multiphase chemical reactions. An advantage of the hydrothermal method is its capability to generate crystalline phases that are not stable at higher temperatures.[86–89]

The hydrothermal method is commonly used for the synthesis of $ZnSnO_3$ with orthorhombic (orth) and face-centred cubic (fcc) phases. In a typical synthesis procedure, both discrete orth and fcc $ZnSnO_3$ phases are simultaneously fabricated in a single solution through hydrothermal treatment. This is achieved by treating a solution having a small amount of ZnO-covered foil, urea, and potassium stannate trihydrate under hydrothermal conditions.[90] According to their study, the synthesis process starts by hydrothermally treating a solution of pure zinc-foil and $C_{20}H_{37}NaO_7S$, OT, and 1.50 g L^{-1} to obtain the ZnO precursor. Subsequently, the obtained ZnO-foil is again hydrothermally treated in an alcohol–water solution containing urea ($CO(NH_2)_2$) and potassium stannate trihydrate ($K_2SnO_3\cdot3H_2O$). Subsequently, the resulting microspheres are dried in air at 60 °C for 6 h. Consequently, pure orth-$ZnSnO_3$ solid microspheres are formed in the solution, as illustrated in Fig. 7. Additionally, pure fcc-$ZnSnO_3$ hollow microspheres are observed on the ZnO-induced template, as illustrated in Fig. 8.[90] The following is a description of the process for the formation of the two products:

$$CO(NH_2)_2 + H_2O \rightarrow NH_4+ + OH^- + CO_2$$

$$K_2SnO_3 + ZnO(l) + 2OH^- \rightarrow \text{orth-}ZnSnO_3 + 2KOH + H_2O$$

$$K_2SnO_3 + ZnO(s) + 2OH^- \rightarrow \text{fcc-}ZnSnO_3 + 2KOH + H_2O$$

To achieve controlled morphologies of the synthesized materials, different surfactants and polymers such as polyethylene glycol (PEG) can be introduced. Numerous studies have been published on the hydrothermal fabrication of nanoparticles, nanorods, nanotubes, nanowires, and hollow spheres. The presence of PEG in the hydrothermal reaction has been observed to facilitate the formation of nanowire morphologies.

In ref. 91, $ZnSnO_3$ nanowire arrays were synthesized using a single-step hydrothermal method. In their study, $Zn(Ac)_2\cdot2H_2O$, $SnCl_4\cdot5H_2O$, and polyethylene glycol (PEG) were used as the precursors. PEG, acting as a complex agent, reacted with $Zn(CH_3CO_2)_2\cdot2H_2O$ and $SnCl_4\cdot5H_2O$ to form a soluble $ZnSn(OH)_n(PEG)_{6-n}$ complex. The presence of PEG was crucial for obtaining the desired morphologies of $ZnSnO_3$ nanowires. The molar ratio of $Zn(CH_3CO_2)_2\cdot2H_2O$ to $SnCl_4\cdot5H_2O$ to PEG

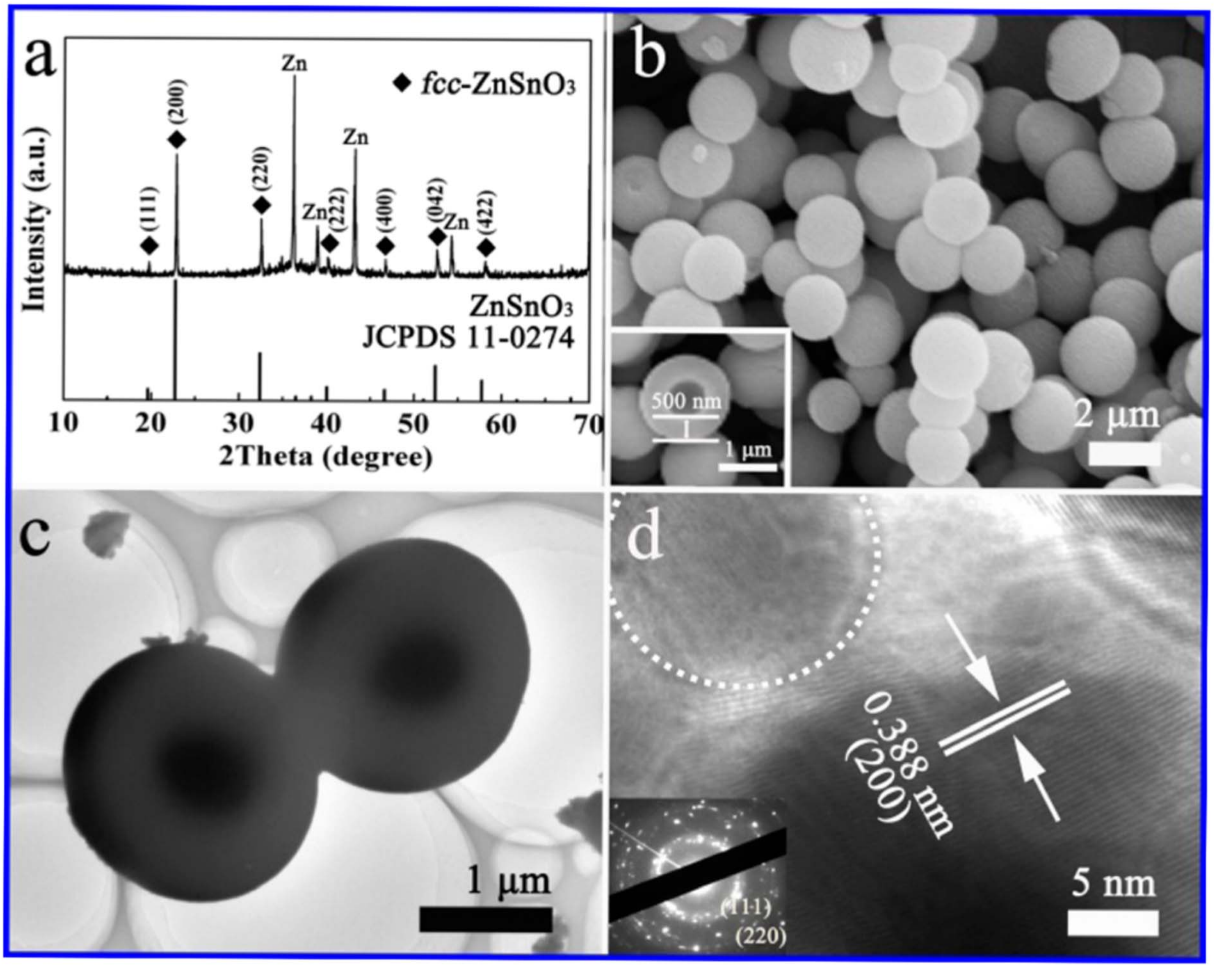

Fig. 8 (a) XRD pattern, (b) SEM image, (c) TEM image, and (d) HRTEM image of $ZnSnO_3$ hollow microspheres.[90]

(4000) was approximately 1 : 1 : 1, and the reaction was performed at a temperature of 200 °C for a duration of 12 h.

Hu and colleagues developed a straightforward chemical solution technique to achieve the large-scale production of well-defined faceted cubic $ZnSnO_3$ and octahedral Zn_2SnO_4 microcrystals.[92] They employed an acid-etching technique, which allowed the originally synthesized zinc stannate faceted microcrystals to undergo a transformation into hollow structures, while preserving their original shape. The synthesis process involved using specific starting materials, namely, tin tetrachloride ($SnCl_4 \cdot 5H_2O$), zinc acetate ($ZnAc_2 \cdot 2H_2O$), and NaOH, which were diluted in distilled water to create a clear solution. In a typical procedure, a 0.02 M $ZnAc_2$ solution was added to a 0.02 M $SnCl_4$ solution at RT and vigorously agitated for 10 min to form a mixed solution for the synthesis of cubic $ZnSnO_3$ microcrystals. Subsequently, this mixture was combined with a 0.2 M NaOH solution (15 mL) and continuously stirred for an additional 10 min. The proportion of Zn^{2+} : Sn^{4+} : Na^+ was kept at a molar ratio of 1 : 1 : 10. Subsequently, a hydrothermal procedure was conducted at 130 °C for 6 h inside a reactor with a 60 mL capacity. After the reaction, the resulting white materials were washed multiple times with ethanol and distilled water.

The reactions that lead to the creation of $ZnSnO_3$ can be summarized as follows:[92]

$$Zn^{2+} + Sn^{4+} + 6OH^- \rightarrow ZnSn(OH)_6$$

$$ZnSn(OH)_6 \rightarrow ZnSnO_3 + 3H_2O$$

$$ZnAc_2 + SnCl_4 + 6NaOH = ZnSnO_3 + 4NaCl + 2NaAc + 3H_2O$$

Under hydrothermal conditions, the creation, and then breaking of the weak-phase $ZnSn(OH)_6$ results in the nucleation and development of $ZnSnO_3$ nanoparticles, involving the aforementioned chemical processes (step 1). More $ZnSnO_3$ nanocrystallites are generated after adding more reactants to the reaction mixture, which are further combined and bound into comparatively augmented nanocrystallites. Noticeably, the obtained $ZnSnO_3$ undergoes a dissolution–recrystallisation process to reduce the high-energy surfaces. Next, the particles combine to form larger aggregates, adhering to the principles of Ostwald ripening (step 2). By extending the reaction duration, the crystals undergo morphological changes and acquire a cubic shape with dimensions measuring several microns. The cubic crystals exhibit 100 lattice planes on their basal surfaces,

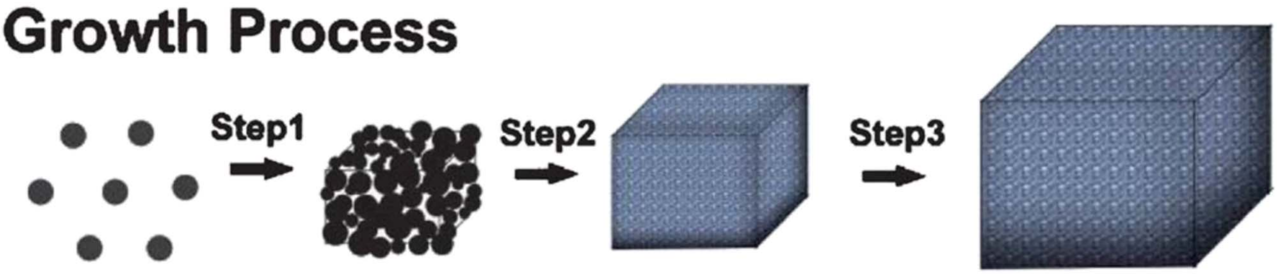

Fig. 9 Possible mechanism for the growth of $ZnSnO_3$ cubic microcrystals.[92]

achieved by adjusting the growth conditions to promote the desired crystal facet (step 3). Lastly, the nanocrystals present in the reaction system adhere to the surfaces of the $ZnSnO_3$ cubic crystals, resulting in the production of huge cubes.[92] Fig. 9 schematically depicts the growth process.

Exercising meticulous control over the chemical characteristics of the mineralizer is crucial, given that it determines the specific surface charges present on the resulting metal oxides. These surface charges serve as a critical factor in the overall process, significantly influencing and facilitating the creation of nanoparticles during the hydrothermal synthesis procedure. Generally, the careful management of the properties of the mineralizer directly impacts the outcome of nanoparticle formation, underscoring its pivotal role in this intricate process. However, the reliability and reproducibility of the process are limited, the necessary equipment is expensive, a longer reaction time is required, and it consumes plenty energy.

3.2. Solvothermal

The solvothermal procedure is similar to the hydrothermal method, excepted for the use of organic solvents instead of water. In the case of alcohols and glycerol as the reaction medium, the reactions are referred to as alcohothermal and gyrothermal, respectively. For the synthesis of NCs with good crystalline characteristics, these synthetic techniques are crucial.[93]

Wang and colleagues used the solvothermal route to achieve a phase transformation from 3D fcc $ZnSnO_3$ nanosheets to 2D orth $ZnSnO_3$ nanosheets. In the conventional route, a white suspension of $ZnSn(OH)_6$ products was promptly formed by combining a solution of $Na_2SnO_3 \cdot 3H_2O$ and $Zn(Ac)_2 \cdot H_2O$ in a mixture of ethylene glycol–deionized water. Subsequently, the $ZnSn(OH)_6$ was moved to a stainless-steel Teflon-lined autoclave and kept at 180 °C for 12 h. Next, the obtain powder was annealed at 500 °C for 4 h at a rate of 2.8 °C min^{-1}. Finally, two-dimensional $ZnSnO_3$ nanosheets were created.[71]

With the shift from 3D nanocubes to 2D $ZnSnO_3$ nanosheets, a straightforward solvothermal pathway was investigated in ref. 94. To form aqueous solutions, $Na_2SnO_3 \cdot 3H_2O$ and $Zn(Ac)_2 \cdot 3H_2O$ were mixed in ethanol–water solution in the usual manner. Subsequently, the Na_2SnO_3 solution was added slowly to the $Zn(CH_3COO)_2$ solution with stirring, resulting in the

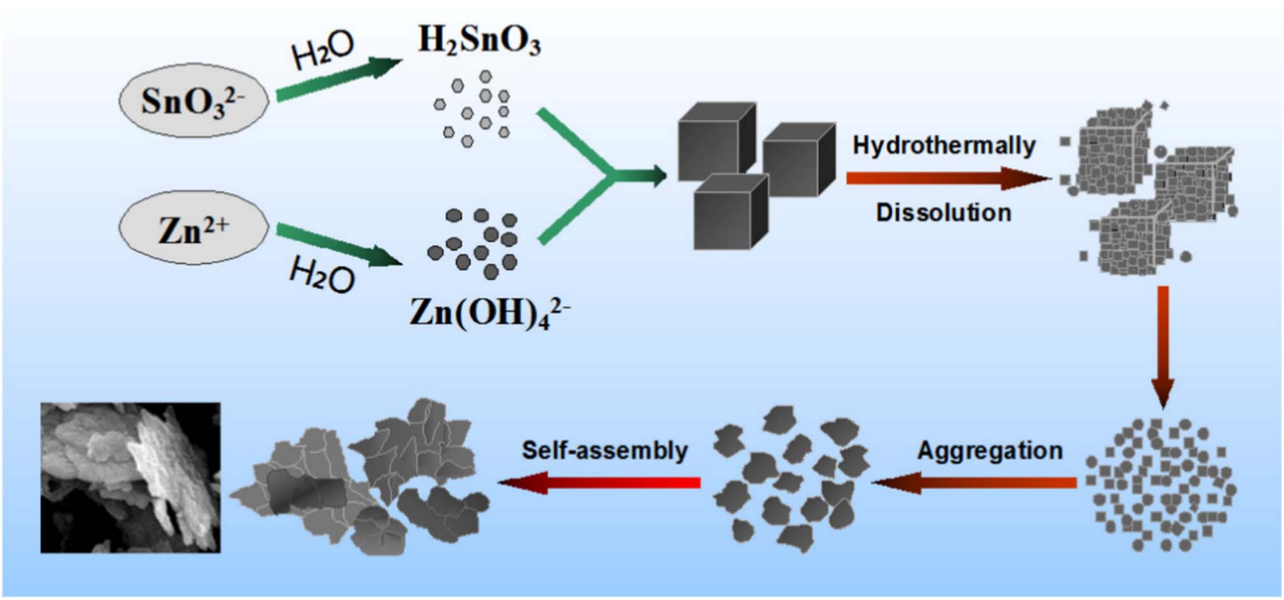

Fig. 10 Diagram depicting the probable process for the formation of the precursor $ZnSn(OH)_6$.[95]

formation of a white $ZnSn(OH)_6$ suspension. Then, the suspension was transferred to a Teflon-lined autoclave and kept at 180 °C for 12 h. The resulting $ZnSn(OH)_6$ was washed and annealed at 600 °C for 3 h. Firstly, the reaction happened due to the hydrolysis of the SnO_3^{2-} ions, resulting in the creation of blend H_2SnO_3. Later, the Zn^{2+} ions undergo a reaction with OH ions, resulting in the formation of the $Zn(OH)_4^{2-}$ phase. This reaction occurs due to the hydrolysis of both CH_3COO and Zn^{2+} ions, as follows:[94]

$$Sn_3^{2-} + 2H_2O \leftrightarrow H_2SnO_3 + 2OH^-$$

$$CH_3COO^- + H_2O \leftrightarrow CH_3COOH + OH^-$$

$$Zn^{2+} + 4H_2O \leftrightarrow Zn(OH)_4^{2-} + 4H^+$$

$$H_2SnO_3 + Zn(OH)_4^{2-} + 2H^+ \rightarrow ZnSn(OH)_6\downarrow + H_2O$$

Under hydrothermal conditions, the metastate $ZnSn(OH)_6$ nanocubes will undergo decomposition and subsequent recrystallization as the temperature and pressure increases. This process follows the breaking-recrystallization pathway, resulting in the formation of a stable nanostructure. Fig. 10 depicts the hypothetical growth process graphically.

3.3. Sol–gel technique

The sol–gel method is a chemical process that creates oxide-based materials from hydrolysable precursors through hydrolysis and condensation reactions. These precursors contain weaker ligands than water, such as halides, nitrates, sulfates, alkoxides, and carboxylates. The hydrolysed precursors form small colloidal nanoparticles in a liquid sol, which can undergo further polycondensation to create a network of polymeric oxide-based materials with oxo-bridges. The initial gels formed through this method consist of both a gel network and a significant liquid phase. Drying these gels, whether at room temperature or through heating, removes the solvent phase and produces dense materials.[96–98]

Due to its simplicity, cost-effectiveness, and capability to produce large-area films, the sol–gel method is widely regarded as an excellent technique for the preparation of $ZnSnO_3$. As demonstrated in ref. 99, the face-centred trigonal perovskite structure of $ZnSnO_3$ was synthesized using a sol gel. They used $Na_2SnO_3\cdot 3H_2O$ (0.01 mol) and $Zn(NO_3)_2\cdot 6H_2O$ (0.01 mol) as the precursors and deionized water (100 mL) as the solvent. Finally, the white $ZnSnO_3$ nanoparticles were dried at 70 °C in an oven for 12 h.

The authors of ref. 100 fabricated polycrystalline IL-type $ZnSnO_3$ *via* the sol–gel process at atmospheric pressure utilizing $Zn(CH_3COO)_2\cdot 2H_2O$, $SnCl_4\cdot 5H_2O$, and ethylene glycol as the precursors. To determine the impact of sintering on the $ZnSnO_3$ structure, the resulting product was sintered at 450 °C, 550 °C, and 650 °C. Upon sintering below 500 °C, they observed that the phase formation is incomplete with the significant presence of ZnO and SnO_2 as secondary phases. In contrast, sintering at 650 °C led to the creation of pure-phase $ZnSnO_3$.

Li *et al.* synthesized Zn–Sn–O thin-films and investigated the impact of sintering (300–1000 °C) on their microstructure, morphological, and optical characteristics.[67] Spinel Zn_2SnO_4

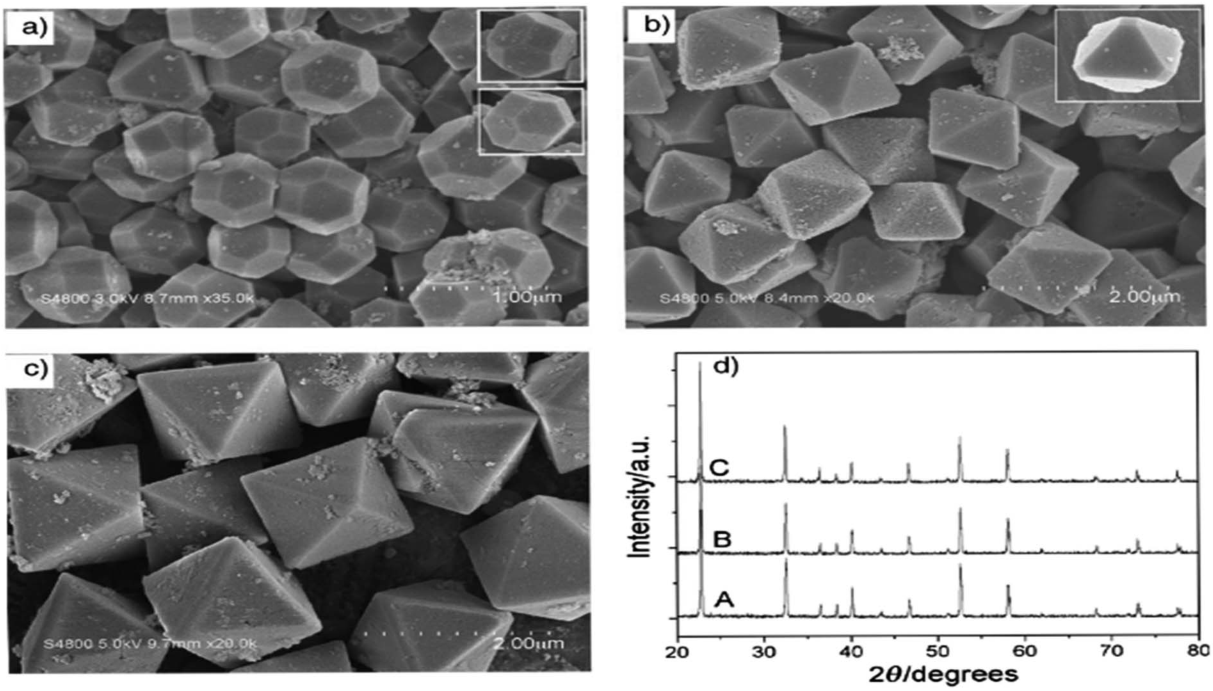

Fig. 11 SEM micrograph of $ZnSnO_3$ obtained using: (a) SDBS 0.15 M, (b) SDBS 0.4 M, and (c) SDBS 0.75 M. (d) XRD pattern of (A) 14-faceted polyhedra, (B) truncated octahedra and (C) octahedra.[102]

was formed in the temperature range of 400–700 °C, while perovskite $ZnSnO_3$ emerged at 800 °C. Alternatively, the formation of Zn_2SiO_4 only occurred at temperatures exceeding 1000 °C. Furthermore, the grain size decreased as the temperature increased from 400 °C to 800 °C. The proposed explanation is that the Zn_2SnO_4 grain grows *via* the surface diffusion pathway, and SnO_2 is dispersed on the surface of Zn_2SnO_4, inhibiting grain formation. Furthermore, when the temperature exceeds 800 °C, the lattice properties clearly decrease. The formation of $ZnSnO_3$ is responsible for this phenomenon, as follows:

$$Sn^{2+} + 0.5O_2 \rightarrow Sn^{4+} + O^{2-}$$

$$Zn_2SnO_4 + SnO_2 \rightarrow 2ZnSnO_3$$

Authors of ref. 101 synthesized porous $ZnSnO_3$ nanocubes *via* the conventional solution-based process together with a calcination process. When annealed at 500 °C, $ZnSn(OH)_6$ lost three water molecules to form amorphous $ZnSnO_3$, which decomposed into amorphous Zn_2SnO_4 and crystalline SnO_2 at 600 °C. The amorphous Zn_2SnO_4 became crystalline Zn_2SnO_4 when the annealing temperature increased to 700 °C. The proposed conversion of $ZnSn(OH)_6$ into different morphologies is as follows:

$$\begin{aligned}ZnSn(OH)_6 &\xrightarrow{500^\circ C} ZnSnO_3(\text{amorphous}) + 3H_2O\\ &\xrightarrow{600^\circ C} Zn_2SnO_4(\text{amorphous})\\ &\quad + SnO_2(\text{crystalline}) \xrightarrow{700^\circ C} Zn_2SnO_4(\text{crystalline})\end{aligned}$$

As demonstrated in ref. 103, $ZnSnO_3$ nanostructures were prepared *via* the sol–gel method using tepa as the gelling medium and trimeric acid hydrolysis medium, which increased the hydrolysis rate and led to initially smaller nucleation, controlling the final particle size. Here, 0.8 mmol $ZnCl_2$ and 0.8 mmol $SnCl_2$ were dispersed in 10 mL DI individually, and then mixed with the gelling agent and hydrolysis agent at 80 °C. Subsequently, the fabricated $ZnSnO_3$ was calcined at 700 °C for 2 h. A straightforward and cost-effective method was employed by Geng *et al.* for the successful synthesis of polyhedral $ZnSnO_3$ with a variety of morphologies without further heat treatment.[32] They showed the

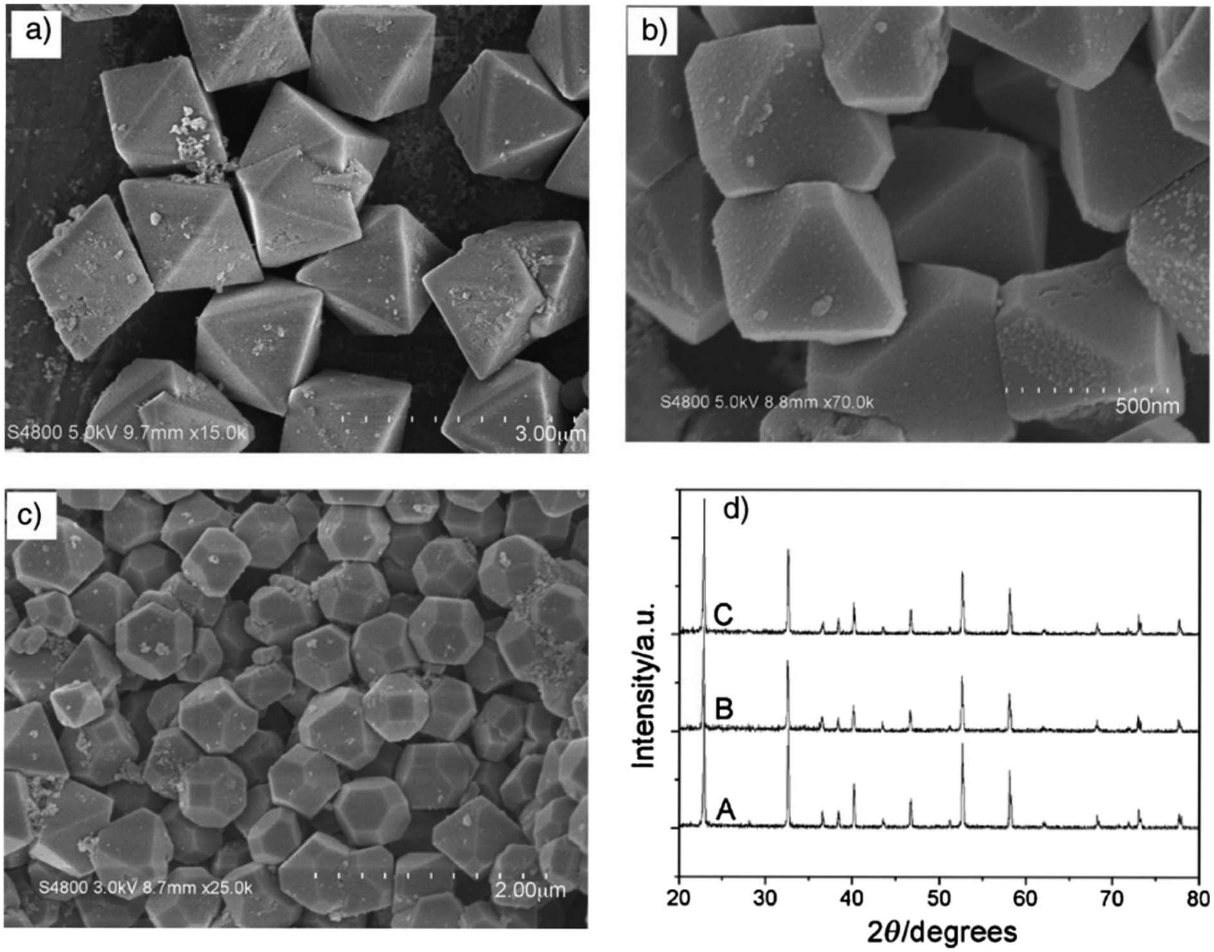

Fig. 12 Typical SEM images of the as-prepared $ZnSnO_3$ products: (a) CTAB 0.15 M, (b) CTAB 0.4 M, and (c) CTAB 0.75 M. (d) Corresponding XRD patterns of the as-prepared $ZnSnO_3$ polyhedra, (A) octahedra, (B) truncated octahedra and (C) 14-faceted polyhedra.[102]

morphology conversion between octahedra and 14-faceted $ZnSnO_3$ using surfactant. In the conventional synthesis, they used tin tetrachloride and $Zn(Ac)_2$ as the starting precursors. Different surfactants in varying concentrations and NaOH were used to control the polyhedral shape. In a beaker, the combined sol was treated at 85 °C with stirring. Finally, centrifugation was used to collect the white polyhedral $ZnSnO_3$ products. When an anionic surfactant (SDBS) was employed, the synthesis of $ZnSnO_3$ yielded different polyhedral shapes depending on the concentration of SDBS such as (1) at 0.25 M, 14-faceted polyhedra were synthesized, (2) at a moderate range of 0.3 to 0.5 M, truncated octahedra were formed, and (3) at 0.5 to 1.0 M, typical octahedra were synthesized. These observations demonstrate how the SDBS concentration influences the morphology of the resulting $ZnSnO_3$ particles. Fig. 11 depicts this shape-evolution pattern. Again, at varying concentrations of the cationic CTAB surfactant, the synthesis of $ZnSnO_3$ yielded different polyhedral shapes such as (1) at 0.2 M, regular octahedra were created, (2) at an intermediate CTAB range of 0.3 to 0.5 M, truncated octahedra were formed, and (3) at 0.5 to 1.0 M, the resulting products exhibited regular 14-faceted polyhedra. These findings demonstrate the influence of CTAB concentration on the morphology of the synthesized $ZnSnO_3$ particles. This shape-evolution form is depicted in Fig. 12.

When the concentration of the anionic SDBS surfactant increased, the *R* value also increased. Consequently, the shape of the $ZnSnO_3$ crystals changed from 14-faceted polyhedra to truncated octahedra, and eventually to regular octahedra. In contrast, when the concentration of the cationic CTAB surfactant increased, the *R* value decreased. This resulted in a different trend compared to the anionic SDBS surfactant, where increasing the CTAB concentration led to a transition from regular octahedra to truncated octahedra, and ultimately to 14-faceted polyhedra (Fig. 13).[102]

The production of $ZnSnO_3$ using the sol–gel method presents significant technical and chemical challenges. This is primarily due to the fact that the precursors used to introduce Sn^{4+} ions typically contain highly electronegative ions (such as Cl^-) or additional metallic ions (such as Na^{2+}), which reduce the likelihood of effective bonding between Sn^{4+} and Zn^{2+}. Additionally, $ZnSnO_3$ exhibits lower thermal stability, leading to its decomposition into Zn_2SnO_4, ZnO, and SnO_2 at elevated temperatures. Thus, to address these issues, alternative low-temperature synthesis techniques such as co-precipitation and hydrothermal synthesis have been employed.[104]

3.4. Vapor–liquid–solid technique

In recent decades, the vapor–liquid–solid (VLS) growth technique has witnessed substantial advancements.[105] Originally used for whisker growth, it has evolved into a practical method for producing semiconductor nanowires. These nanowires have applications in various fields such as nanoscale electronics, optoelectronics, sensing, and energy conversion.[106–108] However, based on a previous literature survey, few research endeavours have been reported on the synthesis of $ZnSnO_3$ using the VLS method.

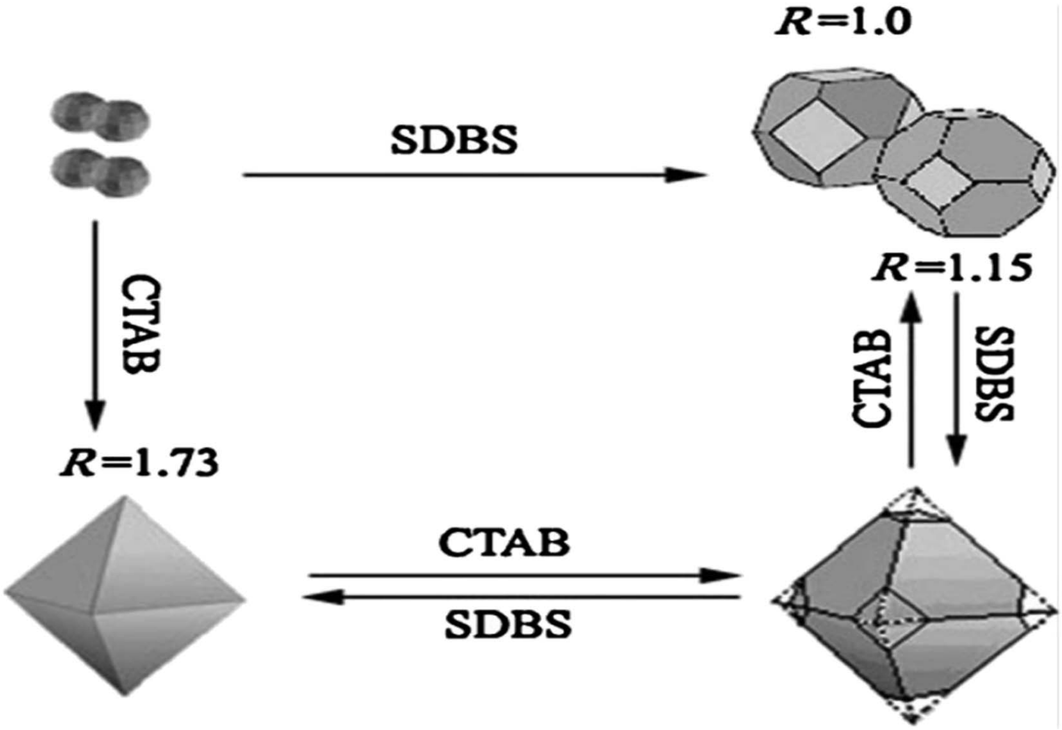

Fig. 13 Schematic diagram depicting the relationship between the ratio *R* and the transformation of the crystal shape.[102]

Wang *et al.* employed the widely recognized vapor–liquid–solid (VLS) mechanism to establish a thermal reaction method for synthesizing $ZnSnO_3$ nanoparticles, as described in ref. 36. The typical synthesis procedure utilized in their study is as follows. Initially, a Zn–Sn buffer layer was deposited as a seed layer on Si and alumina substrates. Subsequently, separate starting materials consisting of Zn and Sn powders were set in an alumina boat. Moreover, to enhance the carbon-thermal reaction while sintering, a blend of source materials containing 50 wt% graphite powder was placed in the central region of a quartz reactor with a stable temperature of 1173 K and left to react at a pressure of 10–20 torr for a duration of 3 h. Throughout the reaction, the flow rate of argon and oxygen gases was maintained at 200 sccm and 10–20 sccm, respectively. Subsequently, the resulting product comprised of single microbelt nanogenerators was constructed using enlarged $ZnSnO_3$ belts measuring 300–1000 μm in length. Furthermore, the power output and piezoelectric properties of these microbelts were assessed.[36]

Wang *et al.* also synthesized lead-free $ZnSnO_3$ triangular-belts using a high-temperature carbon-thermal approach. In this method, the starting materials consisted of Zn and Sn together with graphite powder. These materials were set in the middle point of the reactor to facilitate the process. The system was left to react at a stable temperature of 900 °C and a pressure of 10–20 torr for a duration of 3 h. The flow rate of Ar and O_2 gas during the reaction process was set at 200 and 10–20 sccm, respectively.[37]

Although the vapor–liquid–solid (VLS) technique is a potent method for the synthesis of nanowires, it is associated with certain challenges. For example, it requires specialized, costly equipment for handling the potentially hazardous precursor gases, and achieving uniformity in nanowire properties can be difficult. Furthermore, the incorporation of contaminants during growth process and the energy-intensive high-temperature conditions are additional concerns,[109–111] together with its limited scalability and precursor availability. Nevertheless, VLS is valuable due to its precise control of the

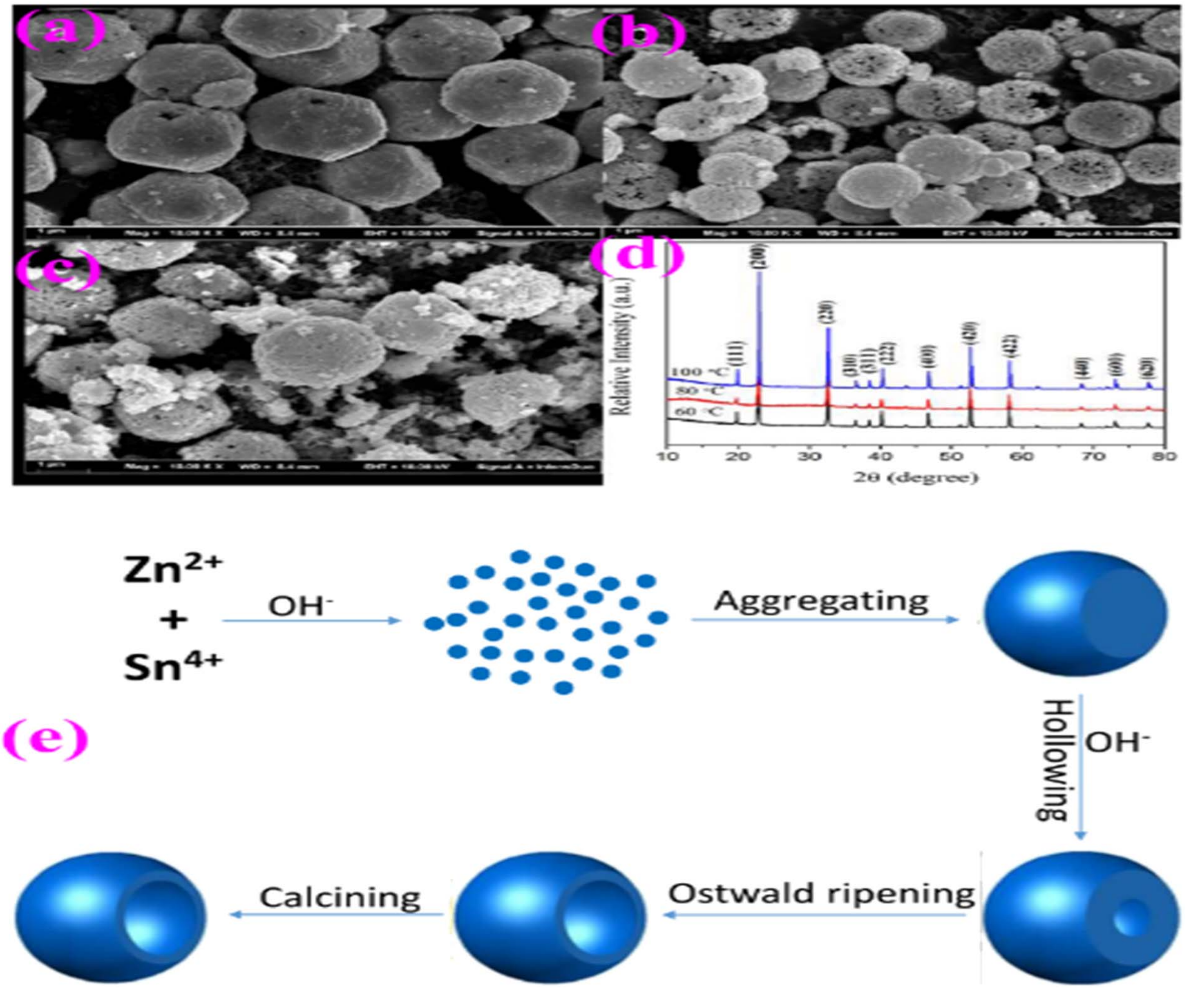

Fig. 14 SEM images of $ZnSnO_3$ obtained at different reaction temperatures: (a) 60 °C, (b) 80 °C, and (c) 100 °C. (d) XRD patterns of $ZnSn(OH)_6$ precursor. (e) Schematic illustration of the possible formation mechanism of $ZnSnO_3$ hollow spheres.[70]

nanowire properties, and thus ongoing research seeks to address the above-mentioned challenges for its broader utilization.

3.5. Coprecipitation technique

The coprecipitation method offers several advantages for the synthesis of $ZnSnO_3$. Firstly, it is a relatively simple and cost-effective technique, which facilitates precise control of the composition and stoichiometry of the final product. This method enables the simultaneous precipitation of zinc and tin ions in a homogeneous manner, leading to a well-mixed precursor solution.[112–114] Additionally, coprecipitation is conducted in aqueous solutions at relatively low temperatures, reducing the energy consumption and environmental impact compared to high-temperature synthesis methods.[115] The coprecipitation technique involves the precipitation of metal hydroxides from a salt precursor using a base in a solvent. By carefully controlling the release of anions and cations, the nucleation and growth kinetics of the particles can be regulated, leading to the synthesis of uniformly dispersed nanoparticles. Proper regulation of the experimental parameters such as pH, reactant and ion concentration, and temperature is crucial for controlling the morphological characteristics during the precipitation process.

In a study conducted by the authors of ref. 116, double-shelled perovskite $ZnSn(OH)_6$ hollow-cubes were fabricated using a rapid coprecipitation method. This involved mixing Zn^{2+}, Sn^{4+}, and OH^- ions with $Na_3C_6H_5O_7$ and NaOH at RT. Subsequently, the obtained $ZnSn(OH)_6$ cubes were transformed into $ZnSnO_3$ double-shelled nanocubes through sintering at 300 °C for 3 h in an N_2 atmosphere.

According to ref. 70, $ZnSnO_3$ hollow spheres were fabricated *via* a straightforward and template-free *in situ* precipitation technique, followed by a dehydration step. During this process, a solution comprised of a water–alcohol mixture was created and subjected to constant stirring. The solution consisted of $Zn(NO_3)_2\cdot 6H_2O$, $SnCl_4\cdot 5H_2O$, and NaOH mixed with the above-mentioned solution. The experimental conditions were kept constant throughout, except for the growth temperature, which was varied from 60 °C to 100 °C to investigate its impact on the morphology of $ZnSnO_3$. The results showed a significant alteration in the shape of $ZnSnO_3$ with an increase in the growth temperature, as depicted in Fig. 14. At 60 °C, the sample primarily consisted of uniform and monodisperse polyhedrons with a diameter of approximately 2.4 μm (Fig. 12a). When the growth temperature was increased to 80 °C, the $ZnSnO_3$ nanoparticles assembled into hollow microspheres (Fig. 14b). However, at 100 °C, uneven $ZnSnO_3$ spheres were obtained, with some small nanoparticles attached to their surface (Fig. 14c). Fig. 14d displays the X-ray diffraction peaks of the $ZnSn(OH)_6$ precursor at various growth temperatures.

A schematic representation of the fabrication route of the $ZnSnO_3$ hollow-spheres is shown in Fig. 14e. Initially, a significant amount of $ZnSn(OH)_6$ is generated in the presence of Zn^{2+} and Sn^{4+} ions at high concentrations of OH^-. Subsequently, these $ZnSn(OH)_6$ particles develop into spherical shapes through rapid aggregation. In the second stage, the surface of the $ZnSn(OH)_6$ microspheres undergo etching due to the dissolution approach in the highly alkaline environment, as the concentration of OH^- ions increases. Concurrently, the re-crystallization of $ZnSn(OH)_6$ occurs in the system, maintaining dynamic-equilibrium.[70]

$$ZnSn(OH)_6 + 4OH^- \leftrightarrow Sn(OH)_6^{2-} + Zn(OH)_4^{2-}$$

The resulting $ZnSnO_3$ nanoparticles typically exhibit high purity, fine particle size, and enhanced crystallinity, making coprecipitation an attractive choice for the production of $ZnSnO_3$ for various applications, including catalysis, sensors, and photovoltaics.[112,115] However, one drawback of the coprecipitation method for synthesizing $ZnSnO_3$ is controlling the particle size and morphology of the resulting material. This method often yields nanoparticles with a wide size distribution and irregular shapes, which can negatively impact the properties and performance of the materials in specific applications.[117,118] Achieving precise control over the particle size and shape can be difficult, requiring additional steps such as post-synthesis annealing and the use of surfactants.[119] Moreover, coprecipitation may also introduce impurities or defects in the final product, which can be undesirable in some applications, such as electronic devices and photocatalysis, where material purity and uniformity are critical for optimal performance.

3.6. Magnetron sputtering technique

Sputtering involves bombarding a target material with high-energy particles, causing the discharge of atoms/molecules from the surface. However, diode sputtering has notable drawbacks, including low deposition rates and high cost. In contrast, magnetron sputtering is a vacuum-coating process known for its high deposition rates, allowing the deposition of metals, alloys, and compounds on various substrates with thicknesses up to the millimeter scale. This technique offers several significant advantages compared to other vacuum coating processes, making it suitable for diverse commercial applications ranging from microelectronic manufacturing to the creation of decorative coatings.[120]

$ZnSnO_3$ films were produced using variable magnetron sputtering settings, employing mixed powder targets of ZnO and SnO_2. In the resulting films, $ZnSnO_3$ nanocrystalline phases were preferentially formed in the columnar grain structure when a short deposition time of 2 h was used. To create the target, pure SnO_2 and ZnO particles with a size of 1 μm were blended in a rotatable drum, maintaining an atomic ratio of Zn/Sn = 1. Subsequently, the mixture was placed on a copper plate, ensuring uniform thickness and a compacted surface. The deposition process involved evacuating the system to a base pressure below 3×10^{-3} Pa, followed by backfilling with Ar gas to achieve a pressure of 0.1–0.5 Pa, depending on the specific array parameters. The glass made of sodium as the substrate was subjected to an in-place cleaning process through RF sputtering for 15 min at 100 W prior to deposition.

Subsequently, the films were deposited *via* RF sputtering for 4 h, using target powers in the range of 200 to 400 W and substrate spacing in the range of 80 to 180 mm based on the specific line-up run surroundings. The deposition rate of the film thickness increased with a variation in the power and spacing, obtaining improved optical properties. The average transmittance of the $ZnSnO_3$ films was about 80%. Moreover, the $ZnSnO_3$ films exhibited optical band gaps in the range of 2.6–3.4 eV and resistivity in the range of 10^{-3}–10^{-4} Ω cm.[79]

A drawback associated with the magnetron sputtering technique for the synthesis of $ZnSnO_3$ is its restricted capacity to accurately control the stoichiometry and composition. This method relies on the sputtering of target materials (in this case, Zn and Sn) on a substrate, and achieving the desired stoichiometry can be challenging due to the differences in the sputter rates between the elements. Consequently, achieving a precise $ZnSnO_3$ composition may require careful process optimization and monitoring, which can be time-consuming and may lead to variations in material quality. Additionally, magnetron sputtering is typically conducted in a vacuum environment, which can be expensive and may limit the scalability of the production process for large-scale applications.

3.7. Electrospinning technique

Standard single-needle electrospinning processes have demonstrated significant performance advantages and wide-ranging applications in various sectors, due to their unique structural characteristics. Electrospinning is influenced by factors such as viscosity, operating voltage, temperature, pressure, and flow velocity.[121]

To prepare the electrospinning precursor solution, tin(II) chloride dihydrate ($SnCl_2 \cdot H_2O$) and zinc chloride ($ZnCl_2$) were dispersed in a mixture of dimethylformamide and absolute ethanol with vigorous stirring, maintaining a Zn^{2+} to Sn^{4+} molar ratio of 1 : 1. Subsequently, polyvinylpyrrolidone (PVP) was added to the mixture, while continuously stirring. Then, the resulting solution was transferred to a plastic syringe with a volume of 10 mL, which was outfitted with a blunt-tip needle of 22-gauge size, serving as the electrospinning precursor solution. A syringe pump was employed to control the feeding rate. Aluminium foil was positioned 20 cm away from the needle to collect the electrospun fibers. To fabricate $ZnSnO_3$ nanofibers, the collected precursor fibers were subjected to calcination in an air environment at 450 °C for a duration of 24 h.[73]

An inherent limitation when employing the electrospinning technique for the synthesis of $ZnSnO_3$ is the potential difficulty in achieving the desired crystalline structure and phase purity. Electrospinning primarily produces materials in the form of nanofibers or nanofibrous mats, which may require additional heat treatment or annealing steps to transform them into the desired $ZnSnO_3$ crystalline structure. This post-treatment can introduce challenges in terms of controlling the grain size and phase purity of the final product, given that the annealing conditions need to be carefully optimized.

3.8. Etching technique

An advantage of the etching technique for the synthesis of $ZnSnO_3$ is its ability to create finely tailored nanostructures with a high degree of precision.[122] By selectively removing certain components from the precursor material, etching enables the fabrication of intricate and well-defined nanoarchitectures of $ZnSnO_3$, such as nanofibers.[73] Furthermore, the etching technique enables the incorporation of $ZnSnO_3$ into specific device architectures, offering versatility and customization in the design of advanced materials for various technological applications.[73,122,123]

A successful etching approach was employed to produce hollow $ZnSnO_3$ nanocube architectures. Depending on the type of etching agent utilized, two paths can be distinguished, *i.e.*, acid and basic agents. In the case of utilizing NaOH solution as both the reactant and etching agent, hollow $ZnSnO_3$ architectures can be synthesized.[124] Initially, solid $ZnSn(OH)_6$ cubic compounds were formed by combining $SnCl_4/ZnCl_2$. Subsequently, $ZnSn(OH)_6$ hollow cube structures were obtained by introducing additional NaOH. Finally, the $ZnSn(OH)_6$ hollow cubes were sintered at an elevated temperature to form hollow $ZnSnO_3$. Fig. 15 illustrates the progression of the hollow $ZnSnO_3$ microstructure. In further investigations, Xu *et al.* discovered that only the combination

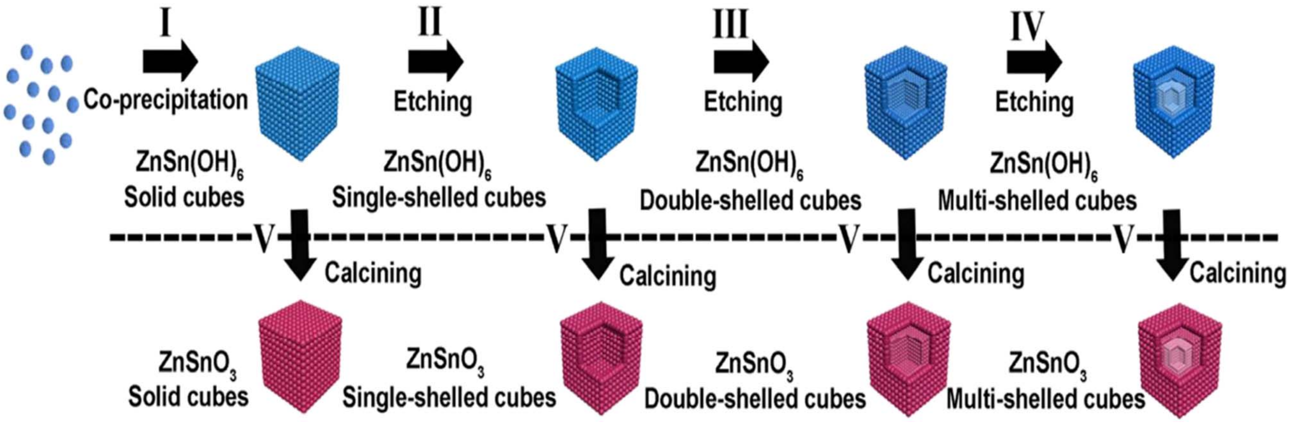

Fig. 15 Schematic illustration of the fabrication of $ZnSnO_3$ hollow-boxes under basic-etching and calcination.[129]

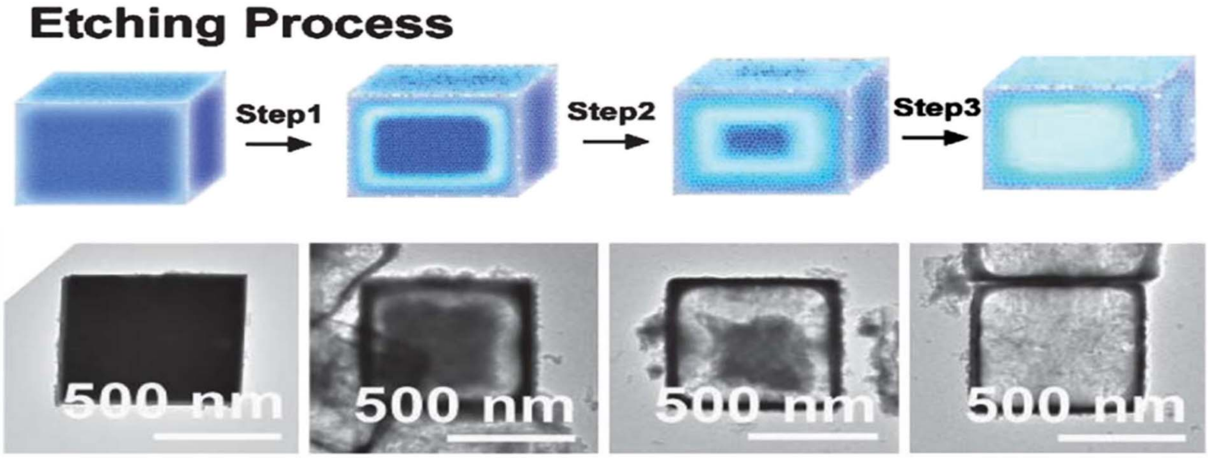

Fig. 16 Potential mechanism illustrating the acid etching process and the resulting synthesized products when employing cubic $ZnSnO_3$ templates.[92]

of $SnCl_4$/$ZnCl_2$/NaOH solution allowed the fabrication of $ZnSnO_3$ hollow-boxes.[125] Similarly, by subjecting a mixture of $SnCl_4$/$Zn(Ac)_2$/NaOH to hydrothermal heating based on Ostwald ripening, hierarchically hollow $ZnSnO_3$ cages were synthesized in a one-pot reaction, requiring an excess amount of NaOH.[126–128]

Cubic microcrystals of $ZnSnO_3$ can be readily transformed into hollow structures by utilizing nitric acid (HNO_3) as an alternative etching agent. Fig. 16 presents the proposed mechanism of the acid etching process, together with TEM images depicting the products obtained at different stages of etching the cubic $ZnSnO_3$ templates.[92]

The etching technique for the synthesis of $ZnSnO_3$ has drawbacks, including challenges in controlling the composition and morphology precisely. Etching involves selectively removing components from a precursor material, which is difficult for complex oxide systems such as $ZnSnO_3$. This can lead to non-uniformity in the final product, affecting the properties and performance. The process is time-consuming, requiring careful optimization of the etching agents and conditions, making synthesis more intricate compared to other methods.

3.9. Mechanochemical technique

Mechanochemical blending is a solid preparation method involving the coupling of mechanical and chemical phenomena on the molecular scale. It is an efficient strategy for synthesizing nanosized metal lattice composite powders due to its simplicity and the ability to achieve composite powder particles with a uniform distribution of grain sizes. In the study reported in ref. 130, the orthorhombic structure of $ZnSnO_3$ was created through mechanochemical grinding. A stoichiometric amount of ZnO and SnO_2 was ground for 20 min to obtain a fine powder, which was annealed at 500 °C for 3 h. Subsequently, the calcination process was repeated for an additional 20 n at 800 °C, with intermittent milling after each 3 h interval. Finally, the mixture was heated to the desired temperature at a ramping speed of 10 °C per minute. However, the mechanochemical technique for synthesizing $ZnSnO_3$ has the drawbacks of extended processing times and high energy consumption. Specifically, this method involves mechanical milling or grinding of precursor materials to induce chemical reactions. Although it can yield high-purity $ZnSnO_3$, the need for prolonged milling can be time-consuming and energy-intensive.

Building on the comprehensive review presented earlier, the precise synthesis of diverse ZTO micro-/nanostructures represents a captivating avenue for achieving enhanced performance and investigating the interplay between structure, properties, and performance. Additionally, the utilization of hollow shapes with customizable sizes, morphologies, and compositions has gained significant attention in the fields of sensors and catalysts owing to their exceptional attributes including improved surface area, reduced density, and extensive volume. These remarkable features make them highly desirable for various applications.

4. Application

In this section, we present some of the common uses of morphological $ZnSnO_3$ nanoparticles in the fields of photocatalysts, sensing, storage, and energy conversion devices.

The ability to design and synthesize $ZnSnO_3$ micro/nanostructures with precise control of their morphology, phase, and homogeneous size holds great potential for expanding their applications. Particularly, the crystalline phase plays a crucial role in energy harvesting applications. Moreover, by enhancing the structural or electrical properties of $ZnSnO_3$ nanocomposites, they can be utilized in a broad range of applications. Extensive studies exhibited the exceptional potential of $ZnSnO_3$ materials in various fields, including gas-sensing, photocatalysis, piezocatalysts, lithium-ion batteries, transparent conductors, and energy storage. Their remarkable electron mobility and electrical conductivity are the main factors responsible for this characteristic.

In this section, we explore the diverse morphology-based applications of $ZnSnO_3$ nanocomposites in photocatalysis, sensing, energy storage and conversion devices, highlighting their significant contributions to these fields.

4.1. Photodegradation of pollutants

Zinc stannate is a ternary metal oxide that holds great potential for photocatalytic and pyroelectric wastewater treatment. Previous studies have established that $ZnSnO_3$ exhibits ferroelectric properties, and similar to ferroelectrics with a perovskite structure, display piezoelectric behaviour, making it an important candidate for wastewater treatment.[148–150] Among the six possible crystal structures, LN-type-$ZnSnO_3$ has been found to possess superior photocatalytic activity due to its piezoelectric property.

The enhanced photocatalytic activity of LN-type $ZnSnO_3$ can be attributed to a specific feature of this crystallite orientation. In LN-type $ZnSnO_3$, the displacement of Zn ions next to the z-axis is higher than Sn ions, resulting in spontaneous polarization. The theoretical high spontaneous polarization of LN-type $ZnSnO_3$ thin films is estimated to be approximately $P_r \approx 59$ C cm^{-2}. However, experimental studies have revealed slightly lower values, such as $P_r \approx 47$ C cm^{-2} at a coercive field of $E_c \approx 130$ kV cm^{-1} and $P_r \approx 30$ C cm^{-2} at $E_c \approx 25$ kV cm^{-1} in single crystal-oriented LN-type $ZnSnO_3$ thin films. Vertically aligned LN-type $ZnSnO_3$ films exhibit a measured spontaneous polarization of $P_r \approx 26$ C cm^{-2}.[14]

In the study in ref. 99, the authors employed the sol–gel method to synthesize $ZnSnO_3$ catalyst nanoparticles and investigated their behaviour in the process of synergistic pyro- and photo-bi-catalysis. When subjected to UV light and thermal cycles in the range of 20 °C to 65 °C, the $ZnSnO_3$ catalyst exhibited a remarkable bi-catalytic dye degradation efficiency of about 98.1%. This efficiency significantly surpassed the photocatalytic degradation (76.8%) and the pyrocatalytic degradation (20.2%). The enhanced photoactivity of $ZnSnO_3$ can be attributed to its ability to facilitate faster separation of electron–hole (e^-–h^+) pairs, effectively acting as an electron trap. Consequently, the piezo-photocatalyst demonstrated a higher decomposition/breakdown performance than the ordinary photocatalyst. This improvement can be attributed to the synergistic catalytic effect achieved by combining the activity of piezo-phototronics with piezoelectricity, semiconductors, and photonics. This coupling effectively reduces the recombination of e^-–h^+ pairs generated by light and improves their mobility by inducing energy band distortion through applied stresses.

In the study in ref. 151, it was demonstrated that the efficiency of the $ZnSnO_3$/ZnO composite was significantly higher than that of $ZnSnO_3$ alone in the degradation of phenol. The $ZnSnO_3$/ZnO nanocomposite exhibited an improved photocatalytic breakdown with a reaction rate of 0.023 min^{-1} than that of 0.0168 min^{-1} for $ZnSnO_3$. This improvement in the reaction rate constant was ascribed to the mixed oxides of the composite with increased surface area of $ZnSnO_3$/ZnO nanocomposites. Consequently, the effective charge separation of the e^-–h^+ pairs occurred. This study also investigated the surface properties of the $ZnSnO_3$/ZnO nanocomposite by studying the isoelectric point (IEP) using the pH drift method. The IEP refers to the pH at which a semiconductor metal oxide carries no net charge, significantly affecting the surface characteristics. The most significant photodegradation of phenol occurred in mildly acidic medium, specifically at a pH of ~6.4. The efficiency of the photocatalytic reaction is directly influenced by the pH of the solution, given that it impacts the formation of hydroxyl radicals and leads to changes in the surface characteristics of the photocatalyst.

Furthermore, in another study in ref. 91, $ZnSnO_3$ nanowires were found to exhibit excellent piezophotocatalytic activity, with a rate constant of ~0.0176 min^{-1}. This enhanced performance can be attributed to the large surface area, superb arrangement, piezo-potential build-up, and band deforming characteristics of the $ZnSnO_3$ nanowires.

The optical-absorption activity of a photocatalyst plays a crucial part in photocatalysis. The authors in ref. 147 synthesized a nanocomposite of S-doped $ZnSnO_3$, which exhibited improved adsorption abilities and a narrow energy gap. The S-$ZnSnO_3$ material exhibited a significantly high specific surface area, reaching 80.63 m^2 g^{-1}, which facilitated the effective adsorption of reactants. Additionally, the introduction of S-doping in $ZnSnO_3$ led to a rapid reduction in the band gap from 3.7 to 2.4 eV. This significant reduction in the band gap resulted in a highly effective photocatalyst for the decomposition of RhB, achieving an efficiency of almost 90%, which is substantially higher than when using pure $ZnSnO_3$.

Furthermore, the manipulation of the surface morphologies of $ZnSnO_3$ also improves its photocatalytic capabilities by reducing the photon-induced recombination e^-–h^+ pairs and enhancing their mobility. In the in ref. 116, the authors designed double-shelled $ZnSnO_3$ hollow-cubes to enhance the photocatalytic breakdown of antibiotic wastewater. These double-shelled $ZnSnO_3$ hollow cubes provide a high surface area, offer large reactive sites, and allow multi-scattering of incident light, thereby enhancing the photocatalytic performance. The trapping experiments conducted in the study detected the primary reactive species in the photo breakdown activity as ·OH and h$^+$. These active species successfully encourage the breakdown of organic dyes under exposure to simulated sunlight.

Hollow $ZnSnO_3$ nanospheres/rGO nanocomposites have been proven to be effective photocatalysts for degrading metronidazole in aqueous solutions. These nanocomposites demonstrated remarkable photodegradation capabilities, particularly under visible light irradiation for a duration of 180 min. The hollow $ZnSnO_3$ nanospheres achieved a degradation efficiency of 42.1%, while the $ZnSnO_3$/rGO nanocomposites exhibited an even higher efficiency of 72.5%. In contrast, the pure rGO and $ZnSnO_3$ with rGO physical mixtures displayed a very low performance in terms of photodegradation. The outstanding performance of $ZnSnO_3$/rGO can be related to several factors. Firstly, the hybrid nanocomposite possesses higher adsorption effectiveness for the target dyes. Additionally, it exhibits enhanced absorption of visible light due to the presence of rGO. Finally, the distinctive electronic system of the $ZnSnO_3$/rGO hybrid nanocomposite contributes to its enhanced photocatalytic properties. This finding was reported in ref. 132.

The probable reaction mechanism pathway in the breakdown of dye can be outlined as follows:[116,147]

$$\mathrm{ZnSnO_3} + h\theta \rightarrow e^- + h^+$$

$$\mathrm{OH^-} + h^+ \rightarrow \cdot\mathrm{OH}$$

$$\mathrm{H_2O} + h^+ \rightarrow \mathrm{OH} + \mathrm{H^+}$$

$$e^- + \mathrm{O_2} \rightarrow \cdot\mathrm{O_2}^-$$

$$\mathrm{Dye} + \mathrm{O_2}^-/\cdot\mathrm{OH}/h^+ \rightarrow \text{degradation products}$$

When light of frequency ν equaling the E_g of metal oxide semiconductors illuminates them, the electrons (e^-) in the semiconductors become excited and transition from the VB to the CB. This process generates holes (h^+) in the VB, resulting in the formation of e^-–h^+ pairs. These h^+ and e^- can engage in reactions with H_2O molecules, OH^- ions, and dissolved O_2, leading to the creation of $\cdot OH$ radicals and $\cdot O_2^-$ radicals, respectively. Conversely, the organic dye can also undergo photosensitization. When a photosensitized organic dye undergoes dissociation in water, it can react with $\cdot OH$ radicals and $\cdot O_2^-$ radicals to produce H_2O and CO_2.

After band-gap excitation and the generation of free charge carriers (electrons and holes), various mechanisms of de-excitation occur, as shown in Fig. 17a and b.[116] Together with the desired redox reactions (pathways 1 and 2), several recombination processes compete with each other, hindering the successful transfer of the carriers to acceptor molecules at the surface.

These competing recombination processes include the recombination of carriers with their oppositely charged counterparts trapped on the surface (route 3) and the recombination of two carriers in the bulk of the semiconductor (pathway 4). Both of these mechanisms contribute to a decrease in the efficiency of the photocatalytic reaction. The rate of recombination is influenced by several factors, including the mobility and trapping behaviour of the charge carriers, the density of defects in the semiconductor lattice, and the presence of an interface with a secondary material, which acts as a sink for either electrons or holes. These factors collectively affect the recombination rates, and consequently impact the overall effectiveness of the photocatalytic process (Table 4).[152]

4.2. Gas sensors

Extensive research has been conducted in recent decades on gas-sensing materials due to their crucial role in detecting hazardous gases. This research has significant implications in industry, environmental monitoring, agriculture, medical diagnosis, military, human health, and aerospace.[161–164] Gas sensors based on n-type semiconductors have been employed to detect inflammable and hazardous gases such as H_2, H_2S, CH_4, C_2H_5OH, and CO. However, a major limitation of these sensors is their lack of selectivity.

Thus, to address this limitation, the n-type $ZnSnO_3$ semiconductor has emerged as a promising solution for enhancing the selectivity of gas sensors towards various gases. The utilization of the sensitive material has been greatly improved by the substantial increase in the specific surface area of $ZnSnO_3$. This enhanced specific surface area of the semiconductor allows for better capacity to adsorb gas molecules. Additionally, the double-shelled hollow morphology with mesoporous features not only facilitates the adsorption of gas molecules on the surface of the sensitive/reactive material but also allows for deep penetration of gas molecules inside the hollow spheres. This unique structure enables the rapid diffusion of gas

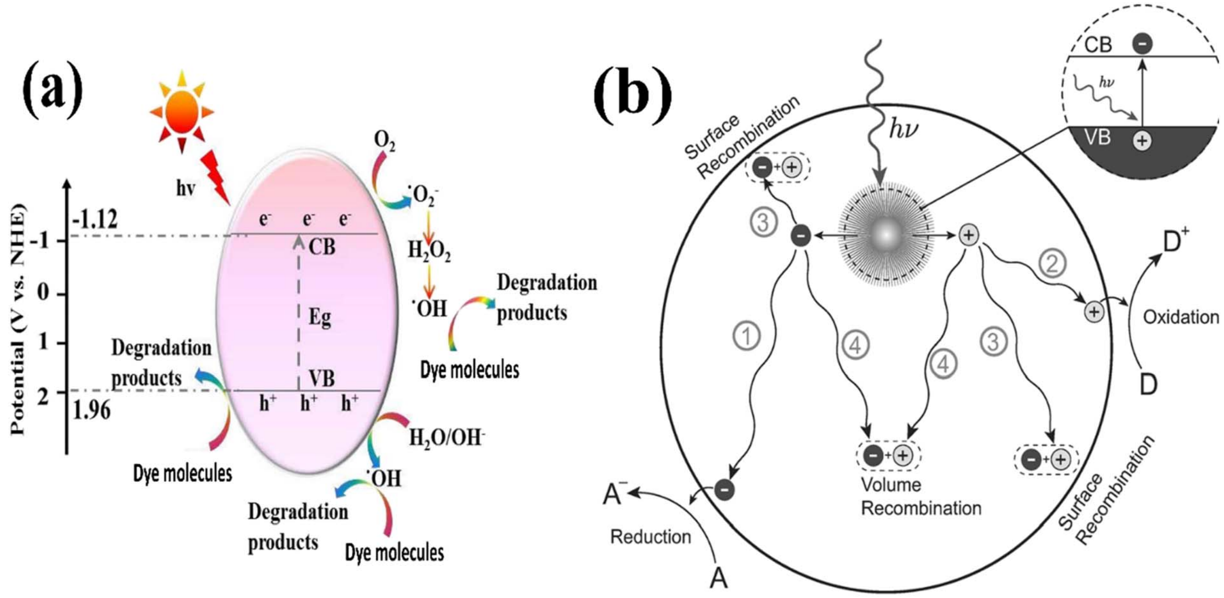

Fig. 17 Illustration of (a) photocatalytic mechanism. (b) Photoinduced formation of an electron hole pair in a semiconductor.[148,217]

Table 4 Photodegradation of pollutants based on $ZnSnO_3$ materials and their performance

Materials	Morphology	Light source	Time	Dye	Efficiency (%)	Ref.
$ZnSnO_3$/rGO	Nanosheets	Visible-light	35	MB	85	76
			90	Phenol	72.89	
$ZnSnO_3$	Nanocubes	UV	80	RhB	98.1[a]	99
					76.8	
S-$ZnSnO_3$	Hollow cubes	Visible-light	100	RhB	90	147
$ZnSnO_3$/rGO/MoS_2	Nanosheets	UV	100	MB	86	153
				RhB	78	
$ZnSnO_3$	Hollow cubes	Xe	100	MB	96.52	116
				CIP	85.9	
$ZnSnO_3$/rGO	3D folded	Visible	120	CIP	100	154
$ZnSnO_3$	Nanostructures	UV	120	Acid brown 14	92	103
$ZnSnO_3$/rGO	Hollow nanospheres	Visible light	180	Metronidazole	72.5	132
$ZnSnO_3$/ZnO	Nanocubes	UV	60	Phenol	47	151
AgI/$ZnSn(OH)_6$	Nanocubes	Visible light	40	RhB	100	155
			60	TOC	91	
$ZnSnO_3$	Nanourchins	UV	90	MO	98	75
				2,5-DCP	95	
$ZnSnO_3$/g-C_3N_4	Nanosheets	Visible	120	Tetracycline	85	156
$ZnSnO_3$/g-C_3N_4	Nanocubes	Visible	120	Tetracycline	90.8	157
Cu_3P/$ZnSnO_3$/g-C_3N_4	Nanocubes	Xe lamp	60	Tetracycline	98.45	158
CoP/$ZnSnO_3$	Nanocubes	Visible	60	Tetracycline	96.44	159
CDs-$ZnSnO_3$	Nanocubes	Visible	60	Tetracycline	81.76	144
NDs/$ZnSnO_3$	Nanocubes	Visible	120	Tetracycline	90	160
Ag–$ZnSnO_3$	Hollow nanocubes	UV	240	Caffeine	68[b]	143
					100[c]	

[a] Pyro-/photo-bi-catalysis. [b] pH = 6.5. [c] pH = 7.5.

molecules and oxygen, thereby improving the overall performance of the gas sensor.

$ZnSnO_3$ is widely recognized as an n-type semiconductor, primarily governed by the behaviour of its conduction electrons. When $ZnSnO_3$-based sensors come into contact with air, oxygen molecules tend to adsorb on the sample surface, effectively capturing free electrons from the CB. This process leads to the formation of ionized oxygen species, including O_2^-, O^- and O^{2-}. Consequently, the consumption of electrons results in the creation of a substantial electron depletion layer on the surface of the sample. This electron depletion layer significantly increases the resistance of the sensor, thereby influencing its overall performance.

$ZnSnO_3$ has been extensively studied as a highly effective material for detecting gases that are reducing and combustible. A gas sensor fabricated using polyhedral $ZnSnO_3$ demonstrated exceptional sensitivity, quick recovery, and reliable results for the detection of HCHO gas. Among the various polyhedral shapes, the 14-faceted $ZnSnO_3$, consisting of 6 {100} facets and 8 {111} facets, exhibited significantly greater sensitivity compared to the octahedral shape and commercially available powder. This improved sensitivity is attributed to the larger exposure of the active {100} facets on the 14-faceted $ZnSnO_3$. The increased number of active {100} facets in the 14-faceted $ZnSnO_3$ led to a higher specific surface area, providing more reactive sites for $ZnSnO_3$ to bind gas molecules. Consequently, this results in higher sensitivity. Considering these findings, it is promising to explore the potential of using cubic $ZnSnO_3$ entirely exposed with {100} facets for gas sensing applications.[32]

The researchers in ref. 165 have successfully developed hollow $ZnSnO_3$ nanocages, which showed remarkable gas sensing properties, particularly when detecting formaldehyde gas. These nanocages demonstrated a high gas response, together with short response and recovery times, superior selectivity, and good repeatability and stability, even at low concentrations of HCHO. This study confirmed that the highest response, with a value of 57.6, was achieved when exposed to 50 parts per million (ppm) of HCHO gas at 350 °C. The response time for the nanocages was measured to be 3 s, while the recovery time was 5 s. Alternatively, the sensitivity of these nanocages towards other gases such as C_2H_5OH, $(CH_3)_2CO$, CH_3OH, and NH_3 was significantly lower compared to formaldehyde gas.

To enhance the selectivity of sensors, the researchers in ref. 126 investigated the use of hollow cubic nanoparticles of zinc stannate with a surface area of 22.6319 $m^2\ g^{-1}$, which were synthesized through the hydrothermal process. The sensor fabricated using these samples exhibited significant improvements in selectivity. When exposed to 500 ppm of butane gas at an operating temperature of 380 °C, the response of the hollow microspheres was measured to be 5.79, whereas the response of the solid microspheres was 3.92. Moreover, the response time and recovery time of the hollow $ZnSnO_3$ microspheres were recorded to be 0.3 s and 0.65 s, while that of the solid $ZnSnO_3$ microspheres was 1.3 s and 13.7 s, respectively. These superior features of the sensor were ascribed to the larger specific surface area of the hollow particles in comparison to the solid particles. This enabled better access to the surface, leading to an increased ability to adsorb gas molecules.

Jiang *et al.* employed a hydrothermal technique to prepare perovskite-type $ZnSnO_3$ and conducted gas sensitivity experiments.[166] The results obtained from calculations revealed that acetone molecules strongly interacted with pre-adsorbed O_2^- and O^- on the $ZnSnO_3$ (001) surface, leading to charge transfer and resistance changes in the material. These observed phenomena form the basis for utilizing $ZnSnO_3$ as a sensing material for detecting acetone. The experimental findings demonstrated that the perovskite-type $ZnSnO_3$ exhibited a sheet like morphology with micro-holes on its surface, which contributed to enhanced sensitivity towards $(CH_3)_2CO$ gas. Through gas sensing tests, the ideal performance temperature was determined to be 350 °C, with a response time of 4 s and recovery time of 27 s. The sensitivity of the $ZnSnO_3$ nanosheets produced in this study towards 100 ppm and 10 ppm of $(CH_3)_2CO$ gas was found to be 125.444 and 8.37, respectively. Furthermore, the sensor based on the sheet-like $ZnSnO_3$ maintained 89.64% and 94.74% of its original sensitivity towards 10/100 ppm acetone gas, respectively, after undergoing a stability and repeatability test for five weeks.

One approach to enhance the selectivity towards specific gases involves doping or modifying the gas-sensitive material through the use of another substance and creating composites. This was demonstrated in ref. 167, where $Ag/ZnSnO_3$ structures exhibited sensitivity towards acetone. In this study, it was found that the response to 100 ppm of acetone was 30, with a response time of 2 s and recovery time of 3 s. The optimal operating temperature was determined to be 280 °C. In another study, ref. 168, focused on increasing the sensitivity towards ethanol vapor by doping with NiO. The sensitivity to 20 ppm of C_2H_5OH was measured at 23.95, with a response time of 56 s and recovery time of 48 s. The optimal operating temperature for this system was found to be 160 °C. In ref. 169, the authors synthesized zinc stannate nanofibers with a surface area of 88.4 $m^2\ g^{-1}$ using the electrospinning method. The sensitivity towards acetone was enhanced by doping with $Au/In–ZnSnO_3$. The response to 50 ppm of ethanol was recorded at 19.3, with a response time of 10 s and recovery time of 13 s at 200 °C.

The gas-sensing properties of conventional $ZnSnO_3$ nanoparticles are often unsatisfactory for sensor applications due to their high operating temperatures. These sensors typically require temperatures exceeding 200 °C, which limits their practical use. At lower temperatures, the thermal energy is insufficient to overcome the activation energy barrier, resulting in inadequate reactions with sensitive materials. Simultaneously, as the operating temperature increases, gas molecules gain higher thermal energy, enabling them to surpass the activation energy barrier. This leads to enhanced reactions among gas molecules and adsorbed oxygen, as well as enhanced ion adsorption on the surface of the semiconductor material.

Thus, to address this issue and achieve high-performance gas sensors with reduced working temperatures, various modifications have been applied, such as preparing nanomaterials with different morphologies and doping. In ref. 170, the authors synthesized 3D flower-like $ZnSnO_3$ using the coprecipitation method and improved the C_2H_5OH sensing properties at RT by incorporating nano-TiO_2. This modification significantly enhanced the ethanol response at room temperature, reaching a maximum value of 36.6. The response and recovery time for a low concentration of 10 ppm C_2H_5OH were recorded to be 4 s and 17 s, respectively. The authors attributed the formation of the 3D flower-like structure to the presence of the stabilizer and pH balancer triethanolamine (TEOA) during the synthesis of $ZnSnO_3$.

$ZnSnO_3$ is a conventional n-type metal-oxide semiconductor and its gas sensing mechanism operates through surface control, relying on changes in conductivity during the gas-sensing reaction. Upon exposure to air, $ZnSnO_3$ nanocubes adsorb oxygen ions on their surface, as follows:[171]

$$O_2 + e^- \rightarrow O_{2(ads)}^- \quad (1)$$

$$O_{2(ads)} + 2e^- \rightarrow 2O_{(ads)}^- \quad (2)$$

$$O_{2(ads)} + 4e^- \rightarrow 2O_{(ads)}^{2-} \quad (3)$$

When the $ZnSnO_3$ nanocubes are exposed to $C_2H_5OH/(CH_3)_2CO/HCHO$, the $C_2H_5OH/(CH_3)_2CO/HCHO$ molecules will interact with absorbed oxygen ions as follows:

$$C_2H_5OH/(CH_3)_2CO/HCHO + O_{2(ads)}^- \rightarrow H_2O + CO_2 + e^- \quad (4)$$

$$C_2H_5OH/(CH_3)_2CO/HCHO + 2O_{(ads)}^- \rightarrow H_2O + CO_2 + 2e^- \quad (5)$$

$$C_2H_5OH/(CH_3)_2CO/HCHO + 2O_{(ads)}^{2-} \rightarrow H_2O + CO_2 + 4e^- \quad (6)$$

Eqn (1) to (3) describe the process in which electrons are extracted from the CB of $ZnSnO_3$, leading to an increase in resistance. Alternatively, eqn (4) to (6) depict the process where electrons are returned to the CB of $ZnSnO_3$, resulting in a decrease in resistance. This gas-sensing mechanism highlights that the quantity of surface-adsorbed oxygen ions plays a crucial role in the gas-sensing characteristics of $ZnSnO_3$. As electrons are consumed in the surface region of the sensitive material, a depletion layer is formed, leading to an increase in the resistance of the material, as shown in Fig. 18.[170]

4.3. Anode for lithium-ion batteries

Lithium-ion batteries (LIBs) have revolutionized the energy storage landscape and become the backbone of portable electronic devices, electric vehicles, and grid storage applications. The remarkable combination of high energy density, long cycle life, and low self-discharge rate has made Li-ion batteries the preferred choice in various industries.[186–188] Over the years, extensive research efforts have been directed towards enhancing the performance and safety of Li-ion batteries, driven by the growing demand for sustainable and efficient energy storage solutions. In this case, $ZnSnO_3$ possesses a unique crystal structure and a wide bandgap, making it an intriguing material for Li-ion battery applications. When used

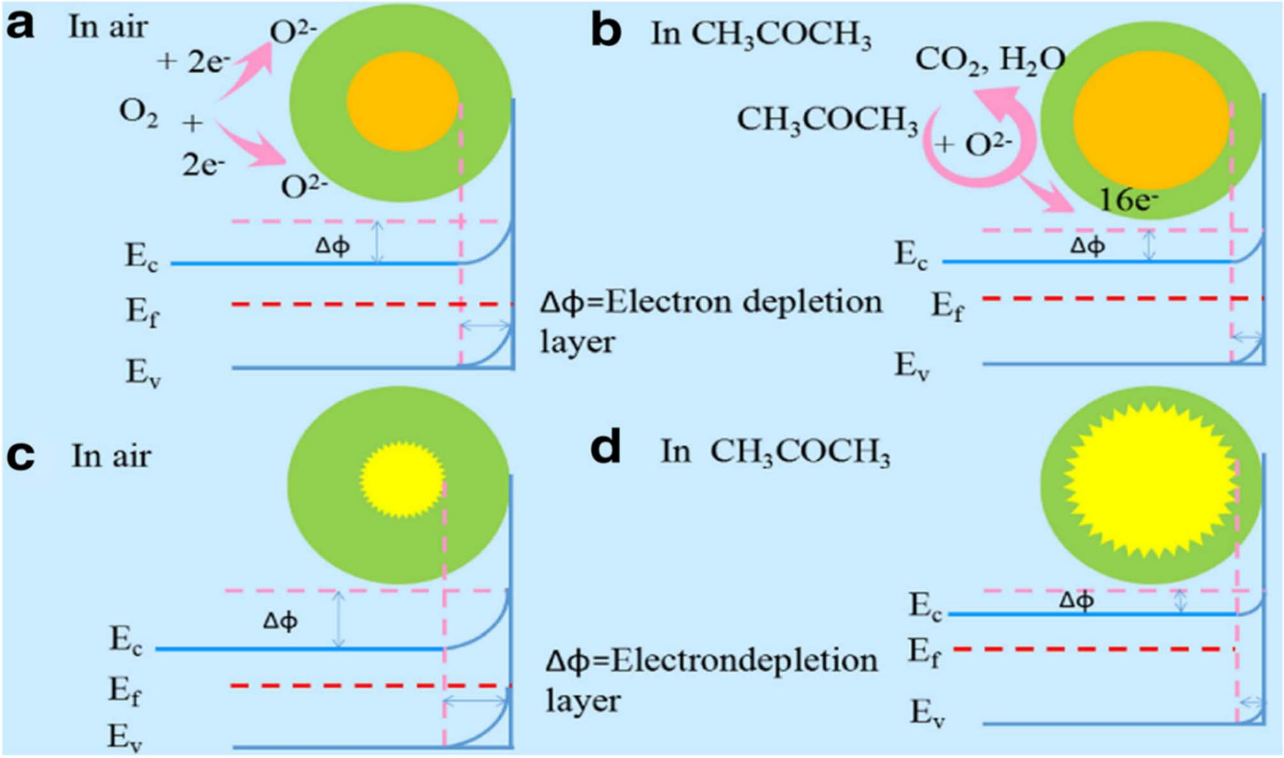

Fig. 18 Schematic band diagrams of $ZnSnO_3$ hollow microspheres exposed to (a) air and (b) CH_3COCH_3, and $ZnSnO_3/SnO_2$ hollow urchin gas sensors exposed to (c) air and (d) CH_3COCH_3.[218]

as an electrode material, $ZnSnO_3$ exhibits an exceptional theoretical capacity of 1320 mA h g^{-1}, surpassing that of many traditional alternatives.[71] This high capacity implies that $ZnSnO_3$ has potential to store more lithium ions, resulting in increased energy storage capabilities (Table 5).

Although the various structures of $ZnSnO_3$ demonstrate appealing characteristics in LIBs, this material still faces notable changes in volume during repeated charging and discharging cycles. Consequently, its rate performance is compromised and it experiences considerable capacity loss, impeding its practical use in real-world applications.[188,189] Thus, to address the aforementioned limitations of $ZnSnO_3$, scientists have implemented diverse approaches, including the creation of micro–nano structures, incorporating transition metals through modification, and combining the material with carbon substances.[190–193]

A reported study demonstrated that a sandwich-like $C/ZnSnO_3$ composite exhibited comparatively higher reversible capacity even after long-term cycling tests.[194] Binary $ZnSnO_3$ nanocomposites combine two practical materials, displaying an improved synergistic performance. The integration of these elements results in an enhancement of their individual properties, including improved electrical and ionic conductivity, enhanced electrochemical reactivity, and increased mechanical stability. The sandwich-like $C/ZnSnO_3$ nanocomposite displayed a reversible capacity of 1107 mA h g^{-1} under a current density of 100 mA g^{-1}, with a coulombic output of ∼98.5% after the 200th cycle. This performance was better than that of sheet-like $ZnSnO_3$, which showed a coulombic output of ∼96.2% after 100 cycles. Fig. 19 illustrates the synthesis procedure of the sandwich-like $ZnSnO_3$@C. The charge–discharge data of the sandwich-like $ZnSnO_3$@C and sheet-like $ZnSnO_3$ at a current density of 100 mA g^{-1} and the cycling performance of the nanocomposite are shown in Fig. 20a–d. The complete electrochemical reaction pathway can be outlined as follows:[71,194]

$$\mathrm{Zn} + x\mathrm{Li}^+ + x\mathrm{e}^- \leftrightarrow \mathrm{Li}_x\mathrm{Zn}_x \leq 1$$

$$\mathrm{C} + y\mathrm{Li}^+ + y\mathrm{e}^- \leftrightarrow \mathrm{Li}_y\mathrm{C}$$

$$\mathrm{Sn} + z\mathrm{Li}^+ + z\mathrm{e}^- \leftrightarrow \mathrm{Li}_z\mathrm{SnO} \leq z \leq 4.4$$

$$4\mathrm{Li}^+ + \mathrm{ZnSnO_3} + 4\mathrm{e}^- \rightarrow \mathrm{Sn} + 2\mathrm{Li_2O} + \mathrm{ZnO}$$

$$6\mathrm{Li}^+ + \mathrm{ZnSnO_3} + 6\mathrm{e}^- \rightarrow \mathrm{Sn} + 3\mathrm{Li_2O} + \mathrm{Zn}$$

Overall, the unique nanostructure of the sandwich-like $C/ZnSnO_3$ composite, with its interconnected carbon nanoplates, encapsulated $ZnSnO_3$ nanoparticles, and high specific surface area (106 m^2 g^{-1}), enables enhanced Li storage activity by facilitating efficient charge transfer, preventing material detachment, and accommodating volume changes during electrochemical reactions.[194]

Amorphous $ZnSnO_3$ double-shell hollow microcubes (D-$ZnSnO_3$) possessed an average edge length of 1.6 mm and

Table 5 Gas sensors based on $ZnSnO_3$ and their performance

Sensing materials	Morphology	Surface area ($m^2\ g^{-1}$)	Target	Concentration (ppm)	Operating temp. (°C)	Response (R_a/R_g)	Response-recovery time (s)	Ref.
$ZnSnO_3$	Hollow microspheres	62.50	Ethanol	500	320	144.3	7, 8	90
	Solid microspheres	40.43			260	80	4, 7	
$CeO_2/ZnSnO_3$	Hollow microspheres	—	Ethanol	100	200	219.2	12, 22	172
$CuO/ZnSnO_3$	Hollow microspheres	—	Ethanol	100	160	131	13, 8	173
Ag–$ZnSnO_3$	Nanocubes	—	Ethanol	100	200	83.96	1, 50	174
$ZnSnO_3$	Hollow microspheres	30.21	Ethanol	100	280	24	—	70
$NiO/ZnSnO_3$	Microsphere-decorated fibers	60	Ethanol	20	160	23.95	56, 48	168
$ZnSnO_3$	Hollow spheres	—	Ethanol	50	270	27.8	0.9, 2.2	127
$ZnSnO_3$	2D nanosheets	85.1	HCHO	10	100	57	36, 42	175
	Nanocubes	59.7	Ethanol		200	20.3	41, 105	
$ZnSnO_3$	3D flower-like	—	Ethanol	1000	RT(25)	36.6	2, 14	170
$ZnSnO_3$	Hollow nanocages	76.4	HCHO	50	350	57.6	3, 5	165
			Ethanol			34.5		
			Acetone			23.6		
$ZnSnO_3$	Nanosheets	57.86	Ethanol	50	320	33	0.36, 9	94
			Acetone		440	41	0.18, 2.6	
$ZnSnO_3$	Nanocubes	71	TEA	100	350	57.5	41, 040	72
$ZnSnO_3$	Hierarchical	67.8	HCHO	10	300	34.1	132, 15	171
$ZnSnO_3$	Hollow cubes	98	HCHO	100	220	37.2	1, 59	124
$ZnSnO_3$	Hollow cubes	—	HCHO	200	270	22.5	—	136
$ZnSnO_3$	Nanocubes	70.001	HCHO	50	210	21.2	—	137
$ZnSnO_3$	Porous nanostructures	—	HCHO	100	240	13.5	1, 10	176
$ZnSnO_3$	Porous cubes	33.7	Toluene	100	300	16.56	2, 11	177
			HCHO			36.81	3, 12	
Zn_2SnO_4	Hierarchical	23.7	Toluene	100	280	25.2	1, 3.5	178
	Spherical	20.6				19.2		
	Cubic	9.1				11.7		
$ZnSnO_3$	Sheet-like	—	Acetone	100	350	125.44	7, 27	166
$ZnSnO_3$/rGO	Hierarchical	33.14	Acetone	50	350	80.37	4, 27	179
$Ag/ZnSnO_3$	Hollow nanocubes	19.1	Acetone	100	280	30	2, 3	167
$ZnSnO_3/SnO_2$	Concave microcubes	69.7	Acetone	50	260	19.1	5.6	180
$ZnSnO_3$	Hollow polyhedrons	—	Acetone	50	240	12.48	17, 10	181
Au/In–$ZnSnO_3$	Nanofibers	88.4	Acetone	50	200	19.3	10, 13	169
$ZnSnO_3$	Nanocages	—	H_2S	100	310	29.4	20, 50	128
$ZnSnO_3$–C1	Hollow cubes	—	H_2S	100	335	14.18	6, 22	182
$ZnSnO_3$	Hollow hexahedron	152	CO_2	400	RT	4, 65	73.2, 79.5	183
PdO–$ZnSnO_3$	Hollow microspheres	—	*n*-Propanol	100	140	30.8	1, 25	184
$ZnSnO_3$	Hollow spheres	53.91	*n*-Butanol	50	200	7.1	2, 40	185
$ZnSnO_3$	Hollow microspheres	22.632	Butane	500	380	5.79	0.3, 0.65	126
	Solid microspheres	—				3.92	1.3, 13.7	

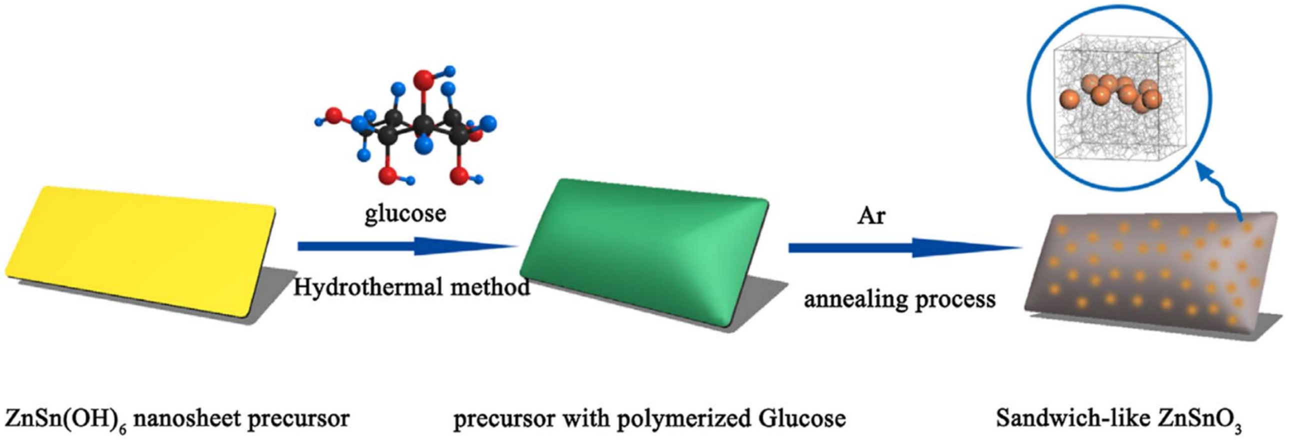

Fig. 19 Schematic illustration depicting the synthesis of sandwich-like $ZnSnO_3$@C.[194]

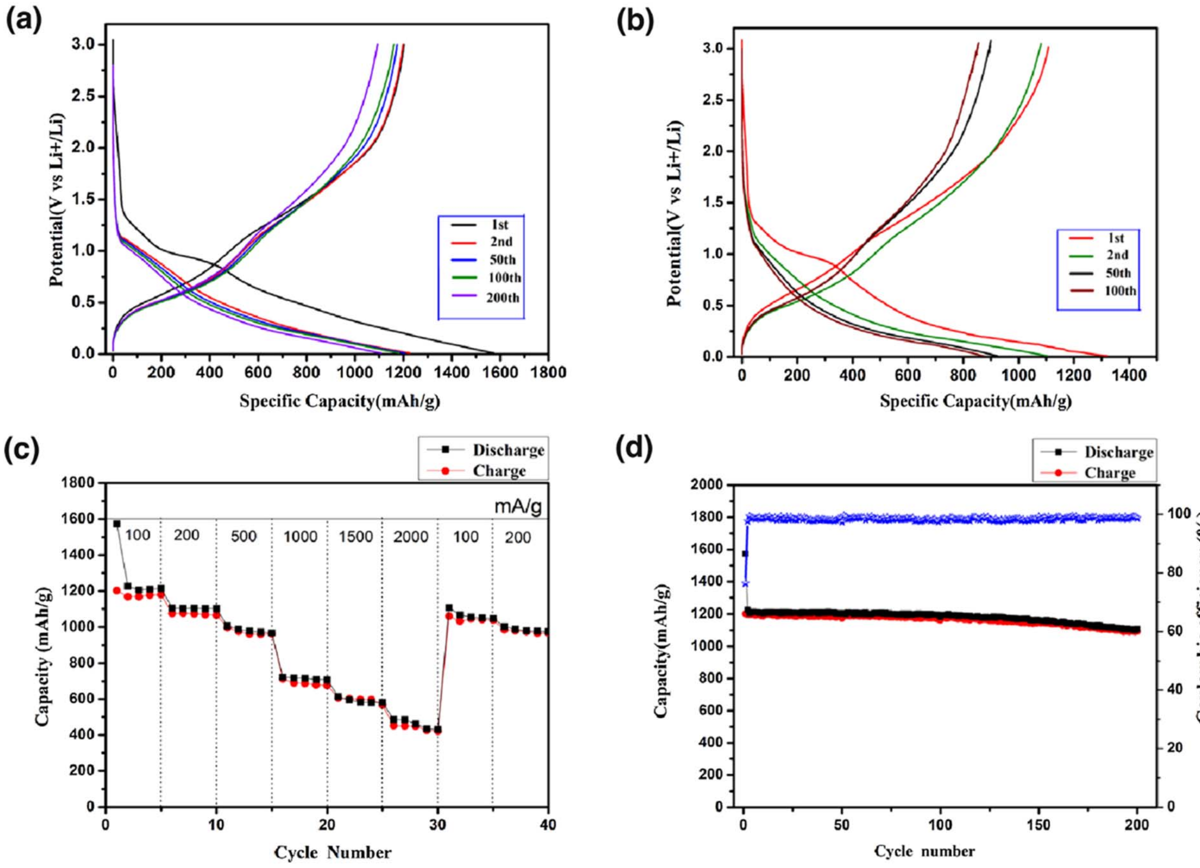

Fig. 20 Charge–discharge profiles of (a) sandwich-like $ZnSnO_3$@C and (b) sheet-like $ZnSnO_3$ at 100 mA g^{-1}. (c) Cycling activity at various current densities. (d) Cycling activity at 100 mA g^{-1} of the sandwich-like $ZnSnO_3$@C.[194]

displayed favourable electrochemical characteristics when utilized as anode materials.[195] Compared to their $ZnSnO_3$ yolk–shell (Y-$ZnSnO_3$) counterparts, the D-$ZnSnO_3$ anodes exhibited a superior performance. They maintained a high coulombic efficiency of 99% at a current density of 100 mA g^{-1} and retained a significant reversible capacity of 741 mA h g^{-1} after 50 cycles. The exceptional electrochemical properties of D-$ZnSnO_3$ originate from its amorphous nature and unique box-in-box hollow architecture. The amorphous structure of D-$ZnSnO_3$ contributed to its isotropy, effectively relieving mechanical strain and preserving the electrode integrity throughout cycling. Furthermore, the hollow box-in-box architecture provided ample space to accommodate the substantial volume changes associated with the insertion and extraction of Li^+ ions.[195]

Lu *et al.* successfully fabricated amorphous isotropic $ZnSnO_3$ nanocubes with a well-defined mesoporous morphology, which were coated with a uniform thin carbon layer, forming core–shell nanoparticles that were interconnected to create a cohesive framework.[196] Comparative electrochemical analysis of the amorphous $ZnSnO_3$@C and crystalline $ZnSnO_3$@C revealed that the former exhibited a superior performance, including a higher specific capacity, superior cyclic stability, and favourable rate capability.

Although the capacity and cyclic stability of the crystalline $ZnSnO_3$@C, with excellent crystallinity, showed a slight increase, reaching a capacity of 791 mA h g^{-1} after 100 cycles, the amorphous $ZnSnO_3$@C demonstrates an improved reversible specific capacity and a more stable capacity retention. The amorphous material achieved reversible capacities exceeding 1020 mA h g^{-1} during the initial 20 cycles, with a marginal increase to 1060 mA h g^{-1} after 100 cycles. This enhancement was attributed to the improved accessibility of lithium ions in the structure. The uninterrupted carbon nanocoating, interconnected porous structure, well-established mesoporosity, and homogeneous amorphous composition all significantly contributed and played essential roles in the accommodation of mechanical strain, buffering of volume changes, and maintenance the structural integrity of $ZnSnO_3$ to achieve a stable cycling performance.

Additionally, this unique structure facilitates rapid electron and Li-ion transfer, thereby enhancing the application of active materials and enabling high-reversible cathode performances.[196] The utilization of ZnO@$ZnSnO_3$ quantum dot (QD) core–shell nanorod (NR) arrays as anodes led to significant improvements in their electrochemical performance.[197] The incorporation of a highly conductive $ZnSnO_3$ QD shell on the ZnO@$ZnSnO_3$ QD core–shell NRs resulted in larger free spaces, which were retained after extended cycling at high current densities. This indicates that the unique arrangement of the ZnO@$ZnSnO_3$ QD core–shell NRs successfully accommodated the volume changes during cycling.

The use of a binder-free electrode offers several advantages, such as establishing good contact with the electrolyte and maintaining a short Li-ion diffusion path within the ZnO@$ZnSnO_3$ QD electrode. Moreover, after 450 cycles at a current density of 1000 mA g^{-1}, there were still more free spaces observed among the ZnO@$ZnSnO_3$ QDs. This suggests that the barrier posed by significant volume expansion can be overcome when the surface of ZnO nanorods is enhanced with $ZnSnO_3$ QD shells.[197] The incorporation of $ZnSnO_3$ hollow cubes in flexible reduced graphene oxide (rGO) sheets, resulting in a porous architecture, was proven to be advantageous in lithium-ion battery applications.[146] This design effectively mitigated the issues associated with significant volume enlargement throughout repetitive charge–discharge cycles. Additionally, the 3D networks created by the $ZnSnO_3$ hollow cubes encased in rGO sheets facilitated the rapid transport of lithium ions and electrons.

As a result of these features, the $ZnSnO_3$-graphene assemblies (ZGAs) exhibited an improved rate capacity, achieving a high specific capacity of 552.6 mA h g^{-1} at a current density of 1200 mA g^{-1}. Furthermore, ZGAs demonstrated excellent cycling stability, maintaining a specific capacity of 745.4 mA h g^{-1} after 100 cycles at a current density of 100 mA g^{-1}. These impressive electrochemical properties indicate that ZGAs have substantial prospect as superior-performance anode materials for LIBs.[146]

In the study described in ref. 198, cube-like, interconnected, amorphous $ZnSnO_3$@TiO_2 nanocomposites were fabricated using a simple co-precipitation followed by TiO_2 coating procedure. The incorporation of an interconnected TiO_2 wrapping and numerous mesopores in the composite structure served to alleviate volume expansion stress, resulting in significantly improved electrochemical stability and performance. The hierarchical heterostructure of the $ZnSnO_3$@TiO_2 nanocomposite exhibited impressive electrochemical characteristics. It demonstrated a high initial discharge capacity of 1590 mA h g^{-1} at a current density of 100 mA g^{-1} and a capacity retention of 780 mA h g^{-1} after 200 cycles, surpassing that of pure $ZnSnO_3$ nanomaterial anodes. The benefits of the hierarchical nanocomposite morphology, together with the synergistic activity of $ZnSnO_3$ and TiO_2 contributed to the improved cycle life of the $ZnSnO_3$@TiO_2 anode. Several factors contribute to its improved performance, as follows: (1) the hierarchical porous 3D morphology reduced the transportation length of lithium ions and electrolyte molecules, increased the contact area between the electrolyte and active material, and enhanced the penetration capability of the electrolyte molecules. (2) The hierarchical porous morphology helped mitigate the significant volume enlargement that occurs during repetitive charge–discharge cycles. (3) The TiO_2 coating layer effectively alleviated the stress induced by volume changes during the Li^+ insertion–extraction conversion reaction. (4) The synergistic effect of the high capacity of $ZnSnO_3$ and superior structural stability of TiO_2 contributed to the superior electrochemical performance of the $ZnSnO_3$@TiO_2 composite. Overall, the hierarchical $ZnSnO_3$@TiO_2 nanocomposite demonstrated promising electrochemical properties, making it a potential candidate for high-performance anode materials in LIBs.[198]

A sustainable cubic $ZnSnO_3$/carbon composite with a high surface area of 896.39 m^2 g^{-1} was successfully synthesized using a low-cost combustion process.[199] The electrochemical

Table 6 Anode materials for lithium-ion batteries based on $ZnSnO_3$ and their performance

Materials	Initial capacity (mA h g^{-1})	Reversible capacity (mA h g^{-1})	Cycle number (*n*)	Current density (mA g^{-1})	Capacity retention (%)	Ref.
Sandwich-like $ZnSnO_3$@C	1573	1107	200	100	70	194
Sheet-like $ZnSnO_3$	1321	872	100	100	66	194
ZnO@$ZnSnO_3$ core–shell	1275	1073	110	200	84	197
Amorphous $ZnSnO_3$@C	1633	1060	100	200	65	196
Crystalline $ZnSnO_3$@C	1350	791	100	200	59	196
Cube-like $ZnSnO_3$@TiO_2	1590	780	200	100	49	198
$ZnSnO_3$/rGO	1987.5	745	100	100	38	146
$ZnSnO_3$/rGO	2013	718	100	100	36	145
$ZnSnO_3$/rGO	1691	713	100	100	42	200
S@Ni/NiO/$ZnSnO_3$	1070	493	400	335	46	201
S@$ZnSnO_3$	781	312	400	335	40	201
$ZnSnO_3$/C nanofibers	1412	586	100	100	42	73
$ZnSnO_3$/C	1469	695	200	100	57	189
$ZnSnO_3$@CNF	1183	582.6	100	100	49	188
$ZnSnO_3$ nanocubes	1470	590	50	200	40	101
Double-shell-$ZnSnO_3$ hollow microcubes	2134	741	50	100	35	195
Yolk–shell $ZnSnO_3$	1570	628	50	100	40	195
$ZnSnO_3$–C hollow microcubes	2255	703	50	100	31	202
$ZnSnO_3$ amorphous hollow microcubes	1921	400	50	100	21	202
Sheet-like $ZnSnO_3$	1390	625	50	100	45	71
$ZnSnO_3$@C/rGO	1984	1040	45	100	52	203
Ag/$ZnSnO_3$	874.5	464.5	45	300	53	204

performance of supercapacitors using the $ZnSnO_3$/C nanocomposite as electrode materials was demonstrated, revealing a good rate capability and exceptional cycling stability. The presence of $ZnSnO_3$ in the composite facilitated rapid ion transfer, resulting in a capacitance retention of approximately 80% after 3000 charge–discharge cycles at different current densities in 6 M KOH electrolyte. These results indicate that the $ZnSnO_3$/carbon composite shows promise as a lightweight electrode material for supercapacitors due to its quick charge–discharge characteristics and strong endurance.

Furthermore, it is anticipated that unique morphology of anode materials, such as porous hollow nanostructures[198] and hybrid carbon-based nanocomposites,[199] can be a viable approach for enhancing lithium storage. However, it is necessary to improve the existing system for evaluating anode materials and assessing their charge–discharge capacity (Table 6).

4.4. Nanodevices

Materials with piezoelectric properties have the remarkable ability to transform mechanical energy into electrical energy. In 2006, Wang[206] pioneered the concept of piezoelectric nanogenerators (PENGs), and since then, there has been an explosion of innovation in the design of nanostructured materials to serve as PENGs for harnessing diverse forms of energy from their surroundings.[121,206,207] This surge in research has led to the development of various piezoelectric materials, including inorganic materials, to further advance this field.[205,208–210]

In the study conducted by Wang *et al.*, a lead-free nanogenerator was developed using a $ZnSnO_3$ microbelts, which demonstrated an impressive performance.[36] When subjected to compressive and releasing strain ranging from 0.8% to 1.0%, the $ZnSnO_3$ microbelts, anchored at their ends on a flexible polystyrene substrate, produced an output power of approximately 3 nW. The resulting output voltage and current were measured to be 100 mV and 30 nA, respectively. These values correspond to an energy conversion efficiency in the range of 4.2% to 6.6% based on the applied strain of 0.8% to 1%. These findings highlight the significant advancements in lead-free $ZnSnO_3$ nanogenerators, showcasing their potential for high output power generation and efficient energy conversion through piezoelectric effects.

Datta and colleagues made a significant contribution by demonstrating the remarkable ferroelectric properties of $ZnSnO_3$ nanowire arrays.[211] They discovered that these arrays exhibited an exceptional remanent polarization value of approximately 30 μC cm^{-2}. This groundbreaking finding provides valuable insights for the future development of $ZnSnO_3$-based ferroelectric devices, enabling a more coordinated and targeted design approach.

Piezoelectric nanogenerators (PENGs) are highly valued for their ability to convert ambient mechanical stimuli into electrical energy, making them ideal for self-powered sensors. In ref. 212, the researchers employed a low-temperature solution-based approach to synthesize aluminium-doped zinc stannate ($ZnSnO_3$) PENGs, which exhibited high electrical outputs in response to external forces. The improved output was ascribed to several factors, including the modified crystalline structure of $ZnSnO_3$, the incorporation of aluminium cations with specific modifications, and the reduced size of the $ZnSnO_3$ nanocube particles. Through their experiments, the researchers

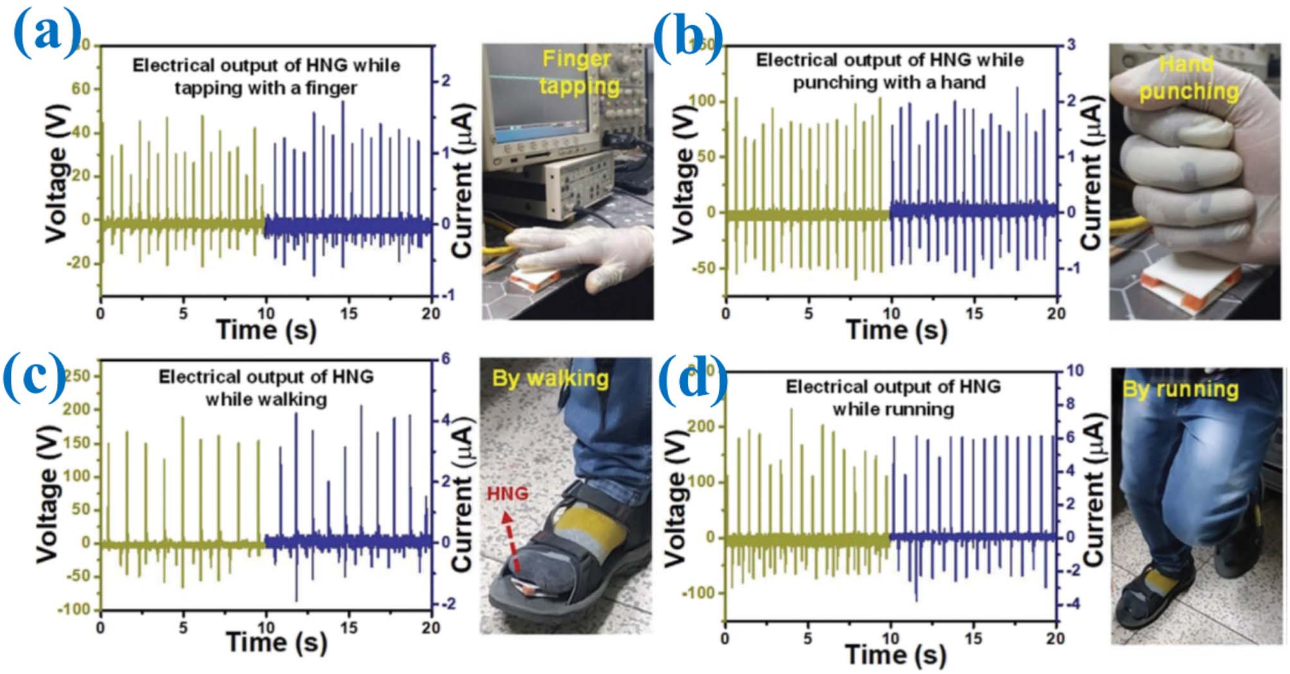

Fig. 21 HNG device showing promising potential for real-time and practical applications in harvesting mechanical energy from everyday human activities. Visual illustrations and the associated electrical data showing the performance and output of the HNG device for (a) finger tapping, (b) hand punching, (c) walking, and (d) running.[213]

determined that the optimal concentration of aluminium dopant was 2 wt%. The resulting Al-doped $ZnSnO_3$ PENG generated impressive electrical outputs of 110 V, 13 μA, and 1200 mW m^{-2} with just 120 beats per min (2 Hz) finger tapping as the input. Remarkably, the PENG charged a 2.2 μF capacitor to 3 V in a mere 8 s with the simple act of finger tapping. Leveraging the high output-to-input ratio, the researchers integrated the PENG with a helmet, enabling it to function as a motion sensor. By detecting the mechanical movements of the wearer, the device converted each footstep into a wireless signal, showcasing its potential applications in capturing human motion data.

The improved electrical output of nanogenerators is attributed to the enhanced dielectric features, enhanced electric dipole moment, and piezoelectric coefficient exhibited by piezoelectric materials. To harness the synergistic effects of $ZnSnO_3$ and polydimethylsiloxane (PDMS) polymer, Yu and colleagues synthesized a composite polymer matrix (CPM) by embedding $ZnSnO_3$ nanocrystals (NCs) in triboelectric PDMS.[213] The resulting hybrid nanogenerator (HNG) demonstrated an impressive performance, with open-circuit voltage (V_{OC}), short-circuit current (I_{SC}), power density, and charge density values of approximately ~410 V, 13 μA, 2 W m^{-2}, and 95 C m^{-2}, respectively, for the 0.15 g reduced graphene oxide (rGO)-$ZnSnO_3$/PDMS CPM-based HNG. The electrical energy produced by harvesting mechanical energy using the HNG was investigated during various human body actions, including finger tapping, hand punching, walking, and running, as depicted in Fig. 21a–d. The obtained electrical output, as represented by the V_{OC}/I_{SC} curves of the HNG, was approximately ~40 V/1.5 μA, ~80 V/2 μA, ~160 V/4 μA, and ~190 V/6 μA for tapping with a finger, punching with a hand, walking, and running, respectively. These results demonstrate the remarkable potential of the HNG in converting mechanical energy from human actions into electrical energy.

Furthermore, the integration of single-crystalline piezoelectric perovskite $ZnSnO_3$ nanocubes with PDMS for the construction of hybrid piezoelectric nanogenerators (HP-NGs) is a significant development. Lee *et al.* successfully demonstrated a highly stable and powerful HP-NG without the need for electrical poling treatment.[214] The HP-NGs incorporating $ZnSnO_3$ nanocubes showed remarkable mechanical durability, robustness, and power-generation capabilities. To evaluate their piezoelectric power generation and mechanical resilience, a direct impact approach was employed. In one experiment, a large-scale HP-NG was placed on a road and subjected to vertical compressive force exerted by a heavy motor vehicle. Fig. 22 captures a snapshot of this experimental motion.

The observed the output voltage and current from the 10 cm × 10 cm HP-NG are depicted in Fig. 22c and d, demonstrating a notable recorded output voltage of approximately ~20 V and output current density of about 1 μA cm^{-2}.

The utilization of $ZnSnO_3$ triangular belts as lead-free nanogenerators has yielded groundbreaking results [*Z*]. By applying a mechanical deformation of 0.1%, these nanogenerators could generate a current of 0.13 μA and voltage of 5.3 50 V, marking the first verification of high output power from lead-free $ZnSnO_3$ nanogenerators.[37]

Fig. 23 presents a schematic diagram illustrating the working mechanism of generating power from a piezoelectric nanogenerator (PENG). Research has confirmed that when

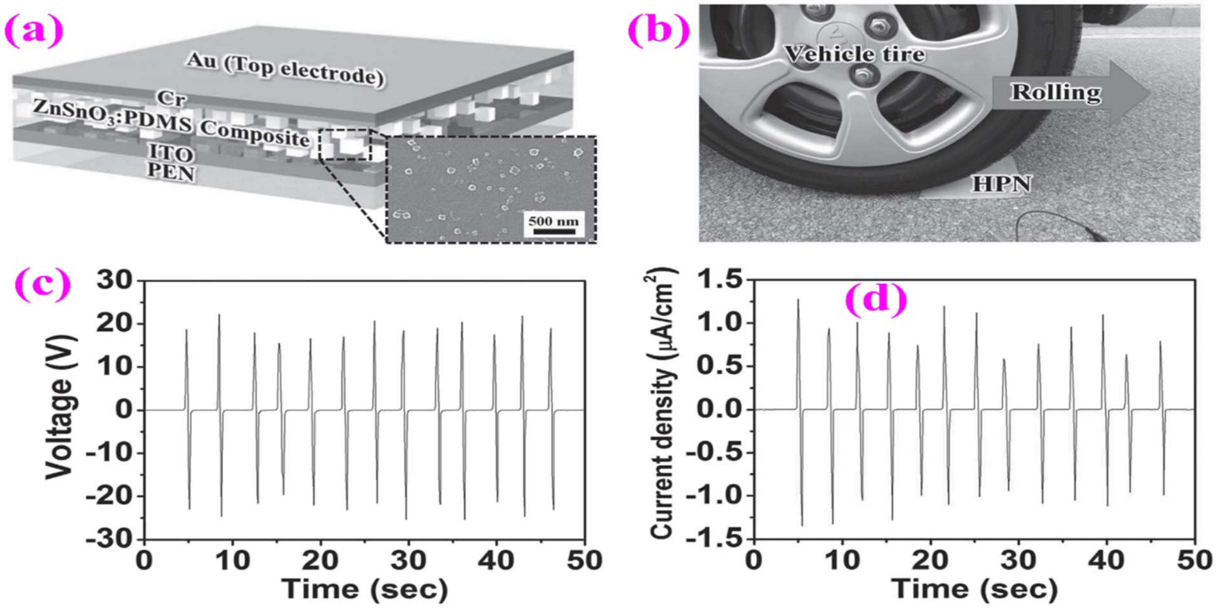

Fig. 22 Structure and power generation by HP-NG when a tire is rolled. (a) Illustration of the structure of the $ZnSnO_3$:PDMS nanocomposite-based flexible HP-NG as seen by the cross-sectional FESEM image. (b) Experimental setup for power production under the rolling of a vehicle tire, in which $ZnSnO_3$:PDMS HP-NG was attached to the road. (c) Output voltage and (d) current density from HP-NG induced by the loading and unloading of a vehicle tire.[214]

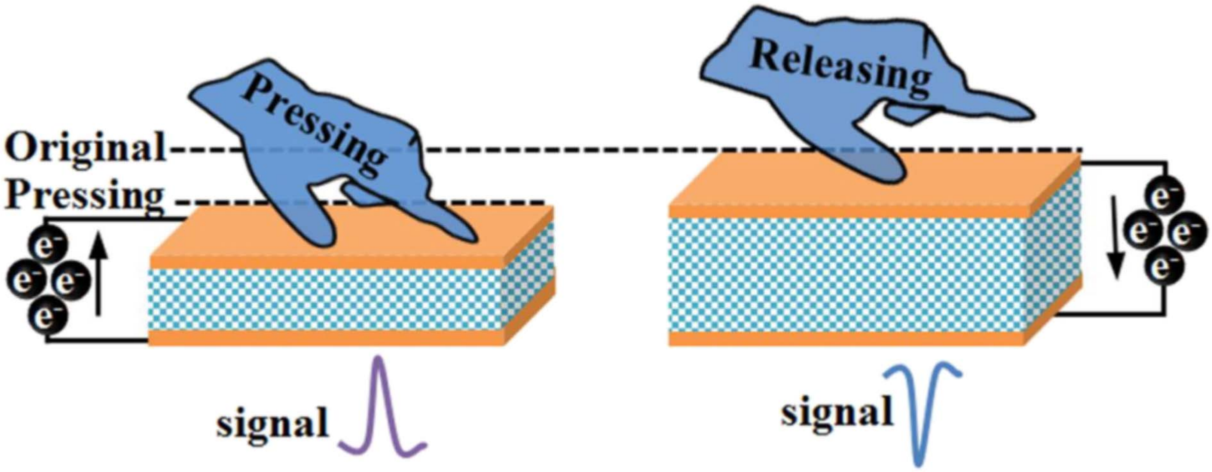

Fig. 23 Working mechanism of generating power from a piezoelectric nanogenerator.[215]

subjected to longitudinal compressive stress, the electric dipoles in the crystal align effectively in a single direction due to the phenomenon known as the stress-induced poling effect.[215] When a tapping force is applied to the device, this pressure causes the separation of positive and negative charges in the $ZnSnO_3$ nanorods, creating an electric dipole.[216] After the cancellation of the interior charges with opposite signs, excess charges remain at both surfaces, leading to a net polarization effect, as depicted in Fig. 7b. This resulting polarization induces opposite charges at the corresponding electrodes, initiating the flow of electrons through the external circuit, thereby generating voltage and current. This mechanism generates a piezoelectric potential across the surface, allowing free electrons to move from the top and bottom electrodes through the external circuit. To balance this generated piezoelectric potential, the electrons accumulate at the interfaces between the nanocubes and electrodes. Subsequently, when the nanocubes decompress after removing the applied load or object, the accumulated electrons return through the external load, and the piezoelectric potential is neutralized.[215,216]

On pressing it will give a positive peak, whereas on releasing the pressure, it produces a negative peak as the electrons move in the opposite direction. Higher and smaller peaks were also observed when compression occurred more rapidly than decompression and the magnitude of the both output voltage and current strongly depends on the compression frequency and applied pressure.[210,215,216]

5. Conclusion and perspectives

Nanostructured materials based on $ZnSnO_3$ possess a multitude of features. These include optical properties, a high isoelectric point, large specific area, non-toxic nature, mechanical characteristics, bending strength, and flexibility. Each of these properties is significant and unique, contributing to the functionality and potential applications of $ZnSnO_3$-based nanostructures. Researchers have dedicated their efforts to exploring the fundamental aspects of developing, modifying, and utilizing $ZnSnO_3$-based nanostructures in various energy and biological applications due to their intriguing characteristics. In this study, we focused on $ZnSnO_3$-based nanostructures and provided a comprehensive overview, with particular emphasis on their applications in Li-ion batteries, photocatalysis, biosensors, and the biological domain. Our review primarily addresses the advancements made in $ZnSnO_3$-based materials to achieve higher performances across diverse applications.

$ZnSnO_3$-based materials exhibit photocatalytic properties, enabling the decomposition of dye molecules upon exposure to visible light. The efficiency of catalysts in photodegradation and their long-term stability are influenced by factors such as structural morphology, crystal orientation, particle size, and oxygen defects. To enhance the photocatalytic activity of $ZnSnO_3$, several strategies have been employed, including the fabrication of $ZnSnO_3$ nanostructured arrays, incorporating additional components such as noble metals, introducing dopants, and integrating carbon materials. These approaches aim to improve the overall photocatalytic performance of $ZnSnO_3$-based materials. However, there are still challenges and opportunities in the field of $ZnSnO_3$ photocatalysis. Despite extensive research in controlled environments, key factors such as surface excess charges, surface additives, and the states of adsorbates in the photocatalytic process are not well-understood. Additionally, there is no consensus on the nature of photogenerated charge carriers and their relationship with charge/energy transfer and bond breaking/forming due to a lack of detailed knowledge about their interactions with adsorbates. Thus, to address these issues, it is crucial to complement traditional ensemble-averaged experimental techniques with time-resolved methods. These experiments aim to uncover the dynamic aspects of $ZnSnO_3$ photocatalysis, leading to a deeper understanding and the potential development of new dynamic-based photocatalysis models.

Researchers have shown that $ZnSnO_3$-based nanostructured materials possess the capability to bind gaseous molecules. In sensing applications, the utilization of nanostructures aims to increase the surface-to-volume ratio, enhancing their reactivity and facilitating their interaction with analytes by facilitating their translocation across cell membranes. To satisfy to biosensing and environmental requirements, scientists have developed electrochemical sensors utilizing $ZnSnO_3$ nanostructures and composite materials. These advancements open possibilities for improved gas sensing and environmental monitoring applications. Due to the benefits mentioned earlier, we emphasize the synthesis strategy to enhance the efficiency of $ZnSnO_3$ and optimize its operating temperature. It is advisable to investigate techniques that can produce $ZnSnO_3$ structures characterized by significant porosity and substantial specific surface areas. Given that surface resistance plays a crucial role in gas sensing, the creation of highly porous structures is advantageous, offering additional reactive sites for the absorption and interaction of the desired gas molecules, and thereby promoting the formation of an electron depletion region. Despite the extensive use of $ZnSnO_3$ nanomaterials and their composites for gas sensing, their selectivity and high operating temperature remain questionable. Thus, to enhance selectivity for specific gases, it is recommended to conduct dynamic tests at varying temperatures. Different temperatures influence the adsorption and desorption processes of distinct gas molecules on the material surface, resulting in temperature-dependent interactions between the sensing material and specific gas molecules. This dynamic testing approach enables the confirmation of the selectivity of a sensor for a particular gas at a specific temperature. Consequently, in practical applications, a single sensor can detect multiple gases by adjusting the working temperature, enabling the accurate identification of the components in mixed gases and significantly expanding the detection capabilities of the sensor.

$ZnSnO_3$-based nanostructures have been found to exhibit promising energy storage characteristics, indicating their potential use as electrode materials in supercapacitors and lithium-ion batteries. $ZnSnO_3$ is widely recognized as a viable active material for batteries, demonstrating a typical reversible energy of 1107 mA h g^{-1} after 200 cycles. These findings highlight the suitability of $ZnSnO_3$ for energy storage applications and suggest its potential for enhancing the performance of supercapacitors and LIBs. Although various related structures have been created and considerable progress has been made in energy storage, there are still many challenges that need further exploration. First, cleverly designed structures optimize certain properties of LIBs, but simultaneously these anodes present other issues. For example, porous or hollow structures can accommodate the volume changes but reduce the volumetric capacity of the whole cell. For the prevalent application of portable, light, small electric devices, volumetric capacity and specific capacity are highly valued.

The comprehensive assessment of anode materials and structures is necessary, aiming to produce electrode architecture designs endowed with better overall performances. Although composites of multi-material blending and combination of different structures are beneficial, more theoretical research including modelling and computing should be applied to maximize the features leading to improved performances, while also minimizing the shortcomings among the different materials and structures.

The exceptional properties of nanostructured $ZnSnO_3$-based materials in energy storage, biosensor, biological, and PENG applications highlight their potential for further scientific advancements in interdisciplinary research. There is significant scope for enhancing the performance of $ZnSnO_3$-based materials in the energy, environmental, and biology fields. Accordingly, further investigations into the tunable characteristics of these materials are anticipated, aiming to unlock their full potential and contribute to advancements in these diverse fields.

Author contributions

Moksodur Rahman: conceptualization, formal analysis, investigation, methodology, visualization, writing – original draft; Muhammad Shahriar Bashar: supervision, resources, validation, writing – review & editing; Md. Lutfor Rahman: validation, visualization, writing – review & editing; Faisal Islam Chowdhury: conceptualization, supervision, project administration, writing – review & editing.

Conflicts of interest

There are no conflicts to declare.

References

1 A. Yamada and M. Konagai, Atomic layer deposition of ZnO films and their application to solar cells, *Solid State Phenom.*, 1999, **67**, 237–247, DOI: **10.4028/www.scientific.net/ssp.67-68.237**.

2 M. Ashraf, S. M. J. Akhtar, A. F. Khan, Z. Ali and A. Qayyum, Effect of annealing on structural and optoelectronic properties of nanostructured ZnSe thin films, *J. Alloys Compd.*, 2011, **509**, 2414–2419, DOI: **10.1016/j.jallcom.2010.11.032**.

3 K. A. Gesheva, T. M. Ivanova and G. Bodurov, Transition metal oxide films: Technology and “smart Windows” electrochromic device performance, in *Prog Org Coat*, Elsevier, 2012, pp. 635–639. DOI: **10.1016/j.porgcoat.2011.07.016**.

4 R. S. Niranjan, K. R. Patil, S. R. Sainkar and I. S. Mulla, High H2S-sensitive copper-doped tin oxide thin film, *Mater. Chem. Phys.*, 2003, **80**, 250–256, DOI: **10.1016/S0254-0584(02)00467-4**.

5 I. M. El Radaf, Promising novel transparent conductive F-doped $ZnSnO_3$ thin films for optoelectronic applications, *J. Mater. Sci.: Mater. Electron.*, 2023, **34**, 215, DOI: **10.1007/s10854-022-09600-z**.

6 S. Y. Bang, F. C. Mocanu, T. H. Lee, J. Yang, S. Zhan, S. M. Jung, D. W. Shin, Y. H. Suh, X. B. Fan, S. Lee, H. W. Choi, L. G. Occhipinti, S. D. Han and J. M. Kim, Robust In-Zn-O Thin-Film Transistors with a Bilayer Heterostructure Design and a Low-Temperature Fabrication Process Using Vacuum and Solution

Deposited Layers, *ACS Omega*, 2020, **5**, 21593–21601, DOI: **10.1021/acsomega.0c02225**.

7 Z. Wu, B. Fan, L. Zhang, Y. Yao, S. Hong, H. Yu and Y. Jia, Strongly enhanced piezoelectric-catalysis of $ZnSnO_3$/graphite hybrid materials for dye wastewater decomposition, *Ceram. Int.*, 2023, **49**(18), 29614–29621, DOI: **10.1016/j.ceramint.2023.06.180**.

8 J. Xu, X. Jia, X. Lou and J. S. Shen, One-step hydrothermal synthesis and gas sensing property of $ZnSnO_3$ microparticles, *Solid-State Electronics*, 2006, **50**(3), 504–507, DOI: **10.1016/j.sse.2006.02.001**.

9 P. Wadkar, D. Bauskar and P. Patil, High performance H_2 sensor based on $ZnSnO_3$ cubic crystallites synthesized by a hydrothermal method, *Talanta*, 2013, **105**, 327–332, DOI: **10.1016/j.talanta.2012.10.051**.

10 Y. Zeng, T. Zhang, H. Fan, G. Lu and M. Kang, Synthesis and gas-sensing properties of $ZnSnO_3$ cubic nanocages and nanoskeletons, *Sens. Actuators, B*, 2009, **143**, 449–453, DOI: **10.1016/j.snb.2009.07.021**.

11 Z. Wang, J. Liu, F. Wang, S. Chen, H. Luo and X. Yu, Size-Controlled Synthesis of $ZnSnO_3$ Cubic Crystallites at Low Temperatures and Their HCHO-Sensing Properties, *J. Phys. Chem. C*, 2010, **114**, 13577–13582, DOI: **10.1021/jp104733e**.

12 X. J. Zhu, L. M. Geng, F. Q. Zhang, Y. X. Liu and L. B. Cheng, Synthesis and performance of Zn_2SnO_4 as anode materials for lithium ion batteries by hydrothermal method, *J. Power Sources*, 2009, **189**, 828–831, DOI: **10.1016/j.jpowsour.2008.07.028**.

13 C. Wang, B. Q. Xu, X. Wang and J. Zhao, Preparation and photocatalytic activity of $ZnO/TiO_2/SnO_2$ mixture, *J. Solid State Chem.*, 2005, **178**, 3500–3506, DOI: **10.1016/j.jssc.2005.09.005**.

14 D. Mukherjee, A. Datta, C. Kons, M. Hordagoda, S. Witanachchi and P. Mukherjee, Intrinsic anomalous ferroelectricity in vertically aligned $LiNbO_3$-type $ZnSnO_3$ hybrid nanoparticle-nanowire arrays, *Appl. Phys. Lett.*, 2014, **105**, 1–6, DOI: **10.1063/1.4902557**.

15 E. Y. Shaba, J. O. Jacob, J. O. Tijani and M. A. T. Suleiman, A critical review of synthesis parameters affecting the properties of zinc oxide nanoparticle and its application in wastewater treatment, *Appl. Water Sci.*, 2021, **11**, 48, DOI: **10.1007/s13201-021-01370-z**.

16 T. Udayabhaskararao, M. Kazes, L. Houben, H. Lin and D. Oron, Nucleation, Growth, and Structural Transformations of Perovskite Nanocrystals, *Chem. Mater.*, 2017, **29**, 1302–1308, DOI: **10.1021/acs.chemmater.6b04841**.

17 A. Perejón, N. Murafa, P. E. Sánchez-Jiménez, J. M. Criado, J. Subrt, M. J. Diánez and L. A. Pérez-Maqueda, Direct mechanosynthesis of pure $BiFeO_3$ perovskite nanoparticles: Reaction mechanism, *J. Mater. Chem. C*, 2013, **1**, 3551–3562, DOI: **10.1039/c3tc30446a**.

18 Y. Cao, D. Jia, J. Zhou and Y. Sun, Simple solid-state chemical synthesis of $ZnSnO_3$ nanocubes and their application as gas sensors, *Eur. J. Inorg. Chem.*, 2009, 4105–4109, DOI: **10.1002/ejic.200900146**.

19 G. Fu, H. Chen, Z. Chen, J. Zhang and H. Kohler, Humidity sensitive characteristics of Zn $2SnO_4$-$LiZnVO_4$ thick films prepared by the sol-gel method, *Sens. Actuators, B*, 2002, **81**, 308–312, DOI: **10.1016/S0925-4005(01)00971-6**.

20 P. Song, Q. Wang and Z. Yang, Ammonia gas sensor based on PPy/$ZnSnO_3$ nanocomposites, *Mater. Lett.*, 2011, **65**, 430–432, DOI: **10.1016/j.matlet.2010.10.087**.

21 D. Kovacheva and K. Petrov, Preparation of crystalline $ZnSnO_3$ from Li_2SnO_3 by low-temperature ion exchange, *Solid State Ion.*, 1998, **109**(3–4), 327–332, DOI: **10.1016/S0167-2738(97)00507-9**.

22 J. X. Wang, S. S. Xie, H. J. Yuan, X. Q. Yan, D. F. Liu, Y. Gao, Z. P. Zhou, L. Song, L. F. Liu, X. W. Zhao, X. Y. Dou, W. Y. Zhou and G. Wang, Synthesis, structure, and photoluminescence of Zn_2SnO_4 single-crystal nanobelts and nanorings, *Solid State Commun.*, 2004, **131**, 435–440, DOI: **10.1016/j.ssc.2004.06.009**.

23 Z. Lu and Y. Tang, Two-step synthesis and ethanol sensing properties of $Zn_2SnO_4SnO_2$ nanocomposites, *Mater. Chem. Phys.*, 2005, **92**, 5–9, DOI: **10.1016/j.matchemphys.2004.11.029**.

24 J. X. Wang, S. S. Xie, Y. Gao, X. Q. Yan, D. F. Liu, H. J. Yuan, Z. P. Zhou, L. Song, L. F. Liu, W. Y. Zhou and G. Wang, Growth and characterization of axially periodic Zn_2SnO_4 (ZTO) nanostructures, *J. Cryst. Growth*, 2004, **267**, 177–183, DOI: **10.1016/j.jcrysgro.2004.03.052**.

25 X. Y. Xue, Y. J. Chen, Q. H. Li, C. Wang, Y. G. Wang and T. H. Wang, Electronic transport characteristics through individual nanowires, *Appl. Phys. Lett.*, 2006, **88**, 182102, DOI: **10.1063/1.2199612**.

26 Y.-Y. Choi, H.-K. Kim, H.-W. Koo, T.-W. Kim and S.-N. Lee, Flexible $ZnSnO_3$/Ag/$ZnSnO_3$ multilayer electrodes grown by roll-to-roll sputtering on flexible polyethersulfone substrates, *J. Vac. Sci. Technol., A*, 2011, **29**, 061502, DOI: **10.1116/1.3632999**.

27 Y. Y. Choi, S. J. Kang and H. K. Kim, Rapid thermal annealing effect on the characteristics of $ZnSnO_3$ films prepared by RF magnetron sputtering, *Curr. Appl. Phys.*, 2012, **12**(4), S104–S107, DOI: **10.1016/j.cap.2012.05.014**.

28 H. Cao, Z. Hu, X. Wei, H. Wang, X. Tian and S. Ding, Conductometric ethanol gas sensor based on a bilayer film consisting of SnO_2 film and SnO_2/$ZnSnO_3$ porous film prepared by magnetron sputtering, *Sens. Actuators, B*, 2023, **382**, DOI: **10.1016/j.snb.2023.133562**.

29 I. Riahi, B. Khalfallah and F. Chaabouni, Physico-chemical properties of perovskite $ZnSnO_3$ thin films deposited on glass and silicon wafers by RF magnetron sputtering, *Opt. Quantum Electron.*, 2022, **54**, DOI: **10.1007/s11082-022-03907-1**.

30 K. Lee, H. S. Han, J. H. Ryu, S. Kang, K. Jung, Y. K. Kim, T. Song, S. Mhin and K. M. Kim, Laser-driven formation of $ZnSnO_3$/CNT heterostructure and its critical role in boosting performance of the triboelectric nanogenerator, *Carbon*, 2023, **212**, DOI: **10.1016/j.carbon.2023.118120**.

31 Q. R. Hu, P. Jiang, H. Xu, Y. Zhang, S. L. Wang, X. Jia and W. H. Tang, Synthesis and photoluminescence of

Zn_2SnO_4 nanowires, *J. Alloys Compd.*, 2009, **484**, 25–27, DOI: **10.1016/j.jallcom.2009.05.057**.

32 B. Geng, C. Fang, F. Zhan and N. Yu, Synthesis of polyhedral ZnSnO3 microcrystals with controlled exposed facets and their selective gas-sensing properties, *Small*, 2008, **4**, 1337–1343, DOI: **10.1002/smll.200701177**.

33 T. Bora, M. H. Al-Hinai, A. T. Al-Hinai and J. Dutta, Phase Transformation of Metastable $ZnSnO_3$ Upon Thermal Decomposition by *In Situ* Temperature-Dependent Raman Spectroscopy, *J. Am. Ceram. Soc.*, 2015, **98**, 4044–4049, DOI: **10.1111/jace.13791**.

34 A. Rovisco, R. Branquinho, J. Martins, E. Fortunato, R. Martins and P. Barquinha, *Growth Mechanism of Seed-Layer Free $ZnSnO_3$ Nanowires : E ff ect of Physical Parameters*, (2019) 37–41.

35 Y. Inaguma, M. Yoshida and T. Katsumata, A polar oxide $ZnSnO_3$ with a $LiNbO_3$-type structure, *J. Am. Chem. Soc.*, 2008, **130**, 6704–6705, DOI: **10.1021/ja801843v**.

36 J. M. Wu, C. Xu, Y. Zhang and Z. L. Wang, Lead-Free Nanogenerator Made from Single $ZnSnO_3$ Microbelt, *ACS Nano*, 2012, **6**, 4335–4340, DOI: **10.1021/nn300951d**.

37 C. Jyh Ming Wu, C. Xu, Y. Zhang, Y. Yang, Y. Zhou, Z. Lin Wang, J. M. Wu, C. Xu, Y. Zhang, Y. Yang, Y. Zhou and Z. L. Wang, Flexible and Transparent Nanogenerators Based on a Composite of Lead-Free $ZnSnO_3$ Triangular-Belts, *Adv. Mater.*, 2012, **24**, 6094–6099, DOI: **10.1002/adma.201202445**.

38 H. Wang, H. Huang and B. Wang, First-principles study of structural, electronic, and optical properties of $ZnSnO_3$, *Solid State Commun.*, 2009, **149**, 1849–1852, DOI: **10.1016/j.ssc.2009.07.009**.

39 H. Gou, F. Gao and J. Zhang, Structural identification, electronic and optical properties of $ZnSnO_3$: First principle calculations, *Comput. Mater. Sci.*, 2010, **49**, 552–555, DOI: **10.1016/j.commatsci.2010.05.049**.

40 Y. Fan, X. Huang, G. Wang and P. Jiang, Core-Shell Structured Biopolymer@$BaTiO_3$ Nanoparticles for Biopolymer Nanocomposites with Significantly Enhanced Dielectric Properties and Energy Storage Capability, *J. Phys. Chem. C*, 2015, **119**, 27330–27339, DOI: **10.1021/acs.jpcc.5b09619**.

41 W. Routray and V. Orsat, Recent advances in dielectric properties–measurements and importance, *Curr. Opin. Food Sci.*, 2018, **23**, 120–126, DOI: **10.1016/j.cofs.2018.10.001**.

42 A. Chaudhary, P. Malik, R. Mehra and K. K. Raina, Influence of ZnO nanoparticle concentration on electro-optic and dielectric properties of ferroelectric liquid crystal mixture, *J. Mol. Liq.*, 2013, **188**, 230–236, DOI: **10.1016/j.molliq.2013.09.020**.

43 S. Gao, C. Wu, Y. Zhang and H. Li, Dielectric regulation of high-graphitized fine ash wrapped cube-like $ZnSnO_3$ composites with boosted microwave absorption performance, *Ceram. Int.*, 2021, **47**, 4994–5002, DOI: **10.1016/j.ceramint.2020.10.074**.

44 D. Anadkat, C. Badampudi, A. Gor and A. V. Sanchela, Investigation of frequency dependent dielectric properties of La-doped $BaSnO_3$-$ZnSnO_3$ solid-solutions, *J. Alloys Compd.*, 2023, **958**, DOI: **10.1016/j.jallcom.2023.170350**.

45 A. Sasmal, A. Patra, P. S. Devi and S. Sen, Space charge induced augmented dielectric permittivity and improved energy harvesting ability of nano-Ag decorated $ZnSnO_3$ filled PVDF based flexible nanogenerator, *Compos. Sci. Technol.*, 2021, **213**, DOI: **10.1016/j.compscitech.2021.108916**.

46 R. Love, Application of Kramers-Kronig relations to the interpretation of dielectric data, *J. Phys. C: Solid State Phys.*, 1974, 7, **http://iopscience.iop.org/0022-3719/7/23/024**.

47 C. Li, H. Wang, B. Wang and R. Wang, First-principles study of the structure, electronic, and optical properties of orthorhombic $BiInO_3$, *Appl. Phys. Lett.*, 2007, **91**, DOI: **10.1063/1.2770761**.

48 J. M. Wu, C. Xu, Y. Zhang and Z. L. Wang, Lead-Free Nanogenerator Made from Single $ZnSnO_3$ Microbelt, *ACS Nano*, 2012, **6**, 4335–4340, DOI: **10.1021/nn300951d**.

49 J. Y. Son, G. Lee, M. Jo, H. Kim, H. M. Jang and Y. Shin, Heteroepitaxial Ferroelectric $ZnSnO_3$ Thin Film, *J. Am. Chem. Soc.*, 2009, 8386–8387, DOI: **10.1021/ja903133n**.

50 H. Gou, J. Zhang, Z. Li, G. Wang, F. Gao, R. C. Ewing and J. Lian, Energetic stability, structural transition, and thermodynamic properties of $ZnSnO_3$, *Appl. Phys. Lett.*, 2011, **98**, 2011–2014, DOI: **10.1063/1.3562013**.

51 Y. Inaguma, M. Yoshida and T. Katsumata, A polar oxide $ZnSnO_3$ with a $LiNbO_3$-type structure, *J. Am. Chem. Soc.*, 2008, **130**, 6704–6705, DOI: **10.1021/ja801843v**.

52 J. Ko and C. T. Prewitt, High-pressure phase transition in $MnTiO_3$ from the ilmenite to the $LiNbO_3$ structure, *Phys. Chem. Miner.*, 1988, **15**, 355–362, DOI: **10.1007/BF00311040**.

53 W. Zhong and D. Vanderbilt, Effect of quantum fluctuations on structural phase transitions in $SrTiO_3$ and $BaTiO_3$, *Phys. Rev. B*, 1996, **53**, 5047, DOI: **10.1103/PhysRevB.53.5047**.

54 Y. Wang, J. A. Yan and M. Y. Chou, Electronic and vibrational properties of γ-AlH_3, *Phys. Rev. B: Condens. Matter Mater. Phys.*, 2008, **77**, DOI: **10.1103/PhysRevB.77.014101**.

55 X. Q. Chen, W. Wolf, R. Podloucky and P. Rogl, Ab initio study of structural stability, elastic, vibrational, and electronic properties of $TiPd_2$, *Phys. Rev. B: Condens. Matter Mater. Phys.*, 2007, **76**, DOI: **10.1103/PhysRevB.76.092102**.

56 M. Leszczyński, E. Litwin-Staszewska, T. Suski, J. Bąk-Misiuk and J. Domagała, Lattice Constant Of Doped Semiconductor, *Acta Phys. Pol. A*, 1995.

57 E. Ching-Prado, C. A. Samudio, J. Santiago-Aviles and S. Velumani, Electronic structure and optical properties of SnO_2:F from PBE0 hybrid functional calculations, *J. Mater. Sci.: Mater. Electron.*, 2018, **29**, 15423–15435, DOI: **10.1007/s10854-018-9067-3**.

58 P. G. Sundell, M. E. Björketun and G. Wahnström, Thermodynamics of doping and vacancy formation in $BaZrO_3$ perovskite oxide from density functional

calculations, *Phys. Rev. B: Condens. Matter Mater. Phys.*, 2006, **73**, DOI: **10.1103/PhysRevB.73.104112**.

59 M. Bououdina, S. Azzaza, R. Ghomri, M. N. Shaikh, J. H. Dai, Y. Song, W. Song, W. Cai and M. Ghers, Structural and magnetic properties and DFT analysis of ZnO:(Al,Er) nanoparticles, *RSC Adv.*, 2017, **7**, 32931–32941, DOI: **10.1039/c7ra01015j**.

60 L. Q. Jiang, J. K. Guo, H. B. Liu, M. Zhu, X. Zhou, P. Wu and C. H. Li, Prediction of lattice constant in cubic perovskites, *J. Phys. Chem. Solids*, 2006, **67**, 1531–1536, DOI: **10.1016/j.jpcs.2006.02.004**.

61 D. Kucharczyk and Z. Niklewski, Accurate X-ray Determination of the Lattice Parameters and the Thermal Expansion Coefficients of VO_2 near the Transition Temperature, *J. Appl. Cryst.*, 1979, **12**, 370–373, DOI: **10.1107/S0021889879012711**.

62 Y. Okada and Y. Tokumaru, Precise determination of lattice parameter and thermal expansion coefficient of silicon between 300 and 1500 K, *J. Appl. Phys.*, 1984, **56**, 314–320, DOI: **10.1063/1.333965**.

63 S. Shikata, T. Tanno, T. Teraji, H. Kanda, T. Yamada and J. I. Kushibiki, Precise measurements of diamond lattice constant using Bond method, *Jpn. J. Appl. Phys.*, 2018, **57**, DOI: **10.7567/JJAP.57.111301**.

64 H. Yusa, M. Akaogi, N. Sata, H. Kojitani, R. Yamamoto and Y. Ohishi, High-pressure transformations of ilmenite to perovskite, and lithium niobate to perovskite in zinc germanate, *Phys. Chem. Miner.*, 2006, **33**, 217–226, DOI: **10.1007/s00269-006-0070-5**.

65 H. Gou, J. Zhang, Z. Li, G. Wang, F. Gao, R. C. Ewing and J. Lian, Energetic stability, structural transition, and thermodynamic properties of $ZnSnO_3$, *Appl. Phys. Lett.*, 2011, **98**, 2011–2014, DOI: **10.1063/1.3562013**.

66 Q. J. Liu, H. Qin, Z. Jiao, F. S. Liu and Z. T. Liu, First-principles calculations of structural, elastic, and electronic properties of trigonal $ZnSnO_3$ under pressure, *Mater. Chem. Phys.*, 2016, **180**, 75–81, DOI: **10.1016/j.matchemphys.2016.05.041**.

67 H. L. Yuan and J. C. Li, Effect of annealing temperature on the growth of Zn-Sn-O nanocomposite thin films, *J. Alloys Compd.*, 2017, **714**, 114–119, DOI: **10.1016/j.jallcom.2017.04.230**.

68 H. Wang, H. Huang and B. Wang, First-principles study of structural, electronic, and optical properties of $ZnSnO_3$, *Solid State Commun.*, 2009, **149**, 1849–1852, DOI: **10.1016/j.ssc.2009.07.009**.

69 H. L. Yuan and J. C. Li, Effect of annealing temperature on the growth of Zn-Sn-O nanocomposite thin films, *J. Alloys Compd.*, 2017, **714**, 114–119, DOI: **10.1016/j.jallcom.2017.04.230**.

70 X. Jia, M. Tian, R. Dai, D. Lian, S. Han, X. Wu and H. Song, One-pot template-free synthesis and highly ethanol sensing properties of $ZnSnO_3$ hollow microspheres, *Sens. Actuators, B*, 2017, **240**, 376–385, DOI: **10.1016/j.snb.2016.08.146**.

71 T. W. Yuejiao Chen, B. Qu, M. Lin, D. Lei, L. Chen and Q. Li, Synthesis of ZnSnO3 Mesocrystals from Regular Cube-like to Sheet-like Structures and Their Comparative Electrochemical Properties in Li-ion Batteries, *J. Mater. Chem. C*, 2015, **3**, 10715–10722, DOI: **10.1039/b000000x**.

72 B. S. Sá, C. A. Zito, T. M. Perfecto and D. P. Volanti, Porous ZnSnO3 nanocubes as a triethylamine sensor, *Sens. Actuators, B*, 2021, **338**, DOI: **10.1016/j.snb.2021.129869**.

73 Y. Zhang, J.-L. Wei, X.-Y. Jin, M.-C. Yu, L. Wang, Yu-H. Guo and S.-T. Dong, Electrospun $ZnSnO_3$-C Nanofiber as an Anode Material for Lithium-Ion Batteries, *J. Electron. Mater.*, 2021, **50**, 4945–4953, DOI: **10.1007/s11664-021-09036-x**.

74 Z. Wang, J. Liu, F. Wang, S. Chen, H. Luo and X. Yu, Size-controlled synthesis of $ZnSnO_3$ cubic crystallites at low temperatures and their HCHO-sensing properties, *J. Phys. Chem. C*, 2010, **114**, 13577–13582, DOI: **10.1021/jp104733e**.

75 Z. Tian, C. Liang, J. Liu, H. Zhang and L. Zhang, Zinc stannate nanocubes and nanourchins with high photocatalytic activity for methyl orange and 2,5-DCP degradation, *J. Mater. Chem.*, 2012, **22**, 17210–17214, DOI: **10.1039/c2jm32406g**.

76 G. Gnanamoorthy, V. K. Yadav, D. Latha, V. Karthikeyan and V. Narayanan, Enhanced photocatalytic performance of $ZnSnO_3$/rGO nanocomposite, *Chem. Phys. Lett.*, 2020, **739**, DOI: **10.1016/j.cplett.2019.137050**.

77 K. Fujiwara, H. Minato, J. Shiogai, A. Kumamoto, N. Shibata and A. Tsukazaki, Thin-film stabilization of $LiNbO_3$-type $ZnSnO_3$ and $MgSnO_3$ by molecular-beam epitaxy, *APL Mater.*, 2018, **7**, 022505, DOI: **10.1063/1.5054289**.

78 Y. Xu, L. Y. Hou and X. M. Zhang, Zinc tin oxide thin films prepared by MOCVD with different Sn/Zn ratios, *Rare Met.*, 2017, **36**, 753–757, DOI: **10.1007/s12598-015-0583-5**.

79 F. W. J. Li, Y. Qi and W. D. Y. Guo, Characteristics of the Structure and Properties of $ZnSnO_3$ Films by Varying the Magnetron Sputtering Parameters, *Acta Metall. Sin. (Engl. Lett.)*, 2016, **29**, 827–833, DOI: **10.1007/s40195-016-0458-2**.

80 G. Yang and S. J. Park, Conventional and microwave hydrothermal synthesis and application of functional materials: A review, *Materials*, 2019, **12**, DOI: **10.3390/ma12071177**.

81 A. Annamalai, D. Carvalho, K. C. Wilson and M. J. Lee, Properties of hydrothermally synthesized Zn_2SnO_4 nanoparticles using Na_2CO_3 as a novel mineralizer, *Mater. Charact.*, 2010, **61**, 873–881, DOI: **10.1016/j.matchar.2010.05.011**.

82 X. Fu, X. Wang, J. Long, Z. Ding, T. Yan, G. Zhang, Z. Zhang, H. Lin and X. Fu, Hydrothermal synthesis, characterization, and photocatalytic properties of Zn_2SnO_4, *J. Solid State Chem.*, 2009, **182**, 517–524, DOI: **10.1016/j.jssc.2008.11.029**.

83 X. Ji, X. Huang, J. Liu, J. Jiang, X. Li, R. Ding, Y. Hu, F. Wu and Q. Li, Hydrothermal synthesis of novel Zn_2SnO_4 octahedron microstructures assemblec with hexagon nanoplates, *J. Alloys Compd.*, 2010, **503**, DOI: **10.1016/j.jallcom.2009.12.038**.

84 J. Zeng, M. Di Xin, K. W. Li, H. Wang, H. Yan and W. Zhang, Transformation process and photocatalytic activities of hydrothermally synthesized Zn_2SnO_4 nanocrystals, *J. Phys. Chem. C*, 2008, **112**, 4159–4167, DOI: **10.1021/jp7113797**.

85 M. Ben Ali, F. Barka-Bouaifel, H. Elhouichet, B. Sieber, A. Addad, L. Boussekey, M. Férid and R. Boukherroub, Hydrothermal synthesis, phase structure, optical and photocatalytic properties of Zn_2SnO_4 nanoparticles, *J. Colloid Interface Sci.*, 2015, **457**, 360–369, DOI: **10.1016/j.jcis.2015.07.015**.

86 L. Zhang, X. Zhang, Y. Zou, Y. H. Xu, C. L. Pan, J. S. Hu and C. M. Hou, Hydrothermal synthesis, influencing factors and excellent photocatalytic performance of novel nanoparticle-assembled $Bi_{25}FeO_{40}$ tetrahedrons, *CrystEngComm*, 2015, **17**, 6527–6537, DOI: **10.1039/c5ce00743g**.

87 Y. Li, Y. L. Lu, K. Di Wu, D. Z. Zhang, M. Debliquy and C. Zhang, Microwave-assisted hydrothermal synthesis of copper oxide-based gas-sensitive nanostructures, *Rare Met.*, 2021, **40**, 1477–1493, DOI: **10.1007/s12598-020-01557-4**.

88 F. Majid, J. Rauf, S. Ata, I. Bibi, A. Malik, S. M. Ibrahim, A. Ali and M. Iqbal, Synthesis and characterization of $NiFe_2O_4$ ferrite: Sol–gel and hydrothermal synthesis routes effect on magnetic, structural and dielectric characteristics, *Mater. Chem. Phys.*, 2021, **258**, DOI: **10.1016/j.matchemphys.2020.123888**.

89 Y. Wang, Y. J. Hu, X. Hao, P. Peng, J. Y. Shi, F. Peng and R. C. Sun, Hydrothermal synthesis and applications of advanced carbonaceous materials from biomass: a review, *Adv. Compos. Hybrid Mater.*, 2020, **3**, 267–284, DOI: **10.1007/s42114-020-00158-0**.

90 Y. Wang, P. Gao, D. Bao, L. Wang, Y. Chen, X. Zhou, P. Yang, S. Sun and M. Zhang, One pot, two phases: Individual orthorhombic and face-centered cubic $ZnSnO_3$ obtained synchronously in one solution, *Inorg. Chem.*, 2014, **53**, 12289–12296, DOI: **10.1021/ic5014126**.

91 C. H. Chou, S. Y. Lee and K. S. Chang, High-density $ZnSnO_3$ nanowire arrays fabricated using single-step hydrothermal synthesis, *J. Am. Ceram. Soc.*, 2020, **103**, 4129–4139, DOI: **10.1111/jace.17100**.

92 G. Ma, R. Zou, L. Jiang, Z. Zhang, Y. Xue, L. Yu, G. Song, W. Li and J. Hu, Phase-controlled synthesis and gas-sensing properties of zinc stannate ($ZnSnO_3$ and Zn_2SnO_4) faceted solid and hollow microcrystals, *CrystEngComm*, 2012, 2172–2179, DOI: **10.1039/c2ce06272k**.

93 H. Zhong, T. Mirkovic and G. D. Scholes, *Nanocrystal Synthesis, Compr. Nanosci. Nanotechnol.*, 2011, 1–5, DOI: **10.1016/B978-0-12-374396-1.00051-9**.

94 Y. Chen, L. Yu, Q. Li, Y. Wu, Q. Li and T. Wang, An evolution from 3D face-centered-cubic $ZnSnO_3$ nanocubes to 2D orthorhombic $ZnSnO_3$ nanosheets with excellent gas sensing performance, *Nanotechnology*, 2012, **23**, 415501, DOI: **10.1088/0957-4484/23/41/415501**.

95 Y. Chen, L. Yu, Q. Li, Y. Wu and Q. Li, An evolution from 3D face-centered-cubic $ZnSnO_3$ nanocubes to 2D orthorhombic $ZnSnO_3$ nanosheets with excellent gas sensing performance, *Nanotechnology*, 2012, **23**, 415501.

96 B. C. Dave and S. B. Lockwood, Sol-Gel Method, *Encyclopedia of Nanotechnology*, 2012, pp. 2459–2470, DOI: **10.1007/978-90-481-9751-4_359**.

97 E. Yilmaz and M. Soylak, Functionalized nanomaterials for sample preparation methods, in *Handbook of Nanomaterials in Analytical Chemistry: Modern Trends in Analysis*, Elsevier, 2019, pp. 375–413, DOI: **10.1016/B978-0-12-816699-4.00015-3**.

98 S. Sakka, Sol-Gel Process and Applications, in *Handbook of Advanced Ceramics: Materials, Applications, Processing, and Properties*, 2nd edn, Elsevier Inc., 2013, pp. 883–910, DOI: **10.1016/B978-0-12-385469-8.00048-4**.

99 J. Chen, W. Luo, S. Yu, X. Yang, Z. Wu, H. Zhang, J. Gao, Y. W. Mai, Y. Li and Y. Jia, Synergistic effect of photocatalysis and pyrocatalysis of pyroelectric $ZnSnO_3$ nanoparticles for dye degradation, *Ceram. Int.*, 2020, **46**, 9786–9793, DOI: **10.1016/j.ceramint.2019.12.251**.

100 T. A. Para, H. A. Reshi and V. Shelke, Synthesis of $ZnSnO_3$ nanostructure by sol gel method, *AIP Conf. Proc.*, 2016, **1731**, 1–4, DOI: **10.1063/1.4947656**.

101 B. Li, X. Li, J. Zai and X. Qian, Facile Synthesis of Porous Zn–Sn–O Nanocubes and Their Electrochemical Performances, *Nanomicro Lett.*, 2016, **8**, 174–181, DOI: **10.1007/s40820-015-0075-z**.

102 B. Geng, C. Fang, F. Zhan and N. Yu, Synthesis of polyhedral $ZnSnO_3$ microcrystals with controlled exposed facets and their selective gas-sensing properties, *Small*, 2008, **4**, 1337–1343, DOI: **10.1002/smll.200701177**.

103 F. Beshkar, O. Amiri and Z. Salehi, Synthesis of $ZnSnO_3$ nanostructures by using novel gelling agents and their application in degradation of textile dye, *Sep. Purif. Technol.*, 2017, **184**, 66–71, DOI: **10.1016/j.seppur.2017.04.024**.

104 T. A. Para, H. A. Reshi and V. Shelke, Synthesis of $ZnSnO_3$ nanostructure by sol gel method, in *AIP Conf Proc*, American Institute of Physics Inc., 2016, DOI: **10.1063/1.4947656**.

105 R. S. Wagner and W. C. Ellis, Vapor-liquid-solid mechanism of single crystal growth, *Appl. Phys. Lett.*, 1964, **4**, 89–90, DOI: **10.1063/1.1753975**.

106 Z. Zhu, M. Suzuki, K. Nagashima, H. Yoshida, M. Kanai, G. Meng, H. Anzai, F. Zhuge, Y. He, M. Boudot, S. Takeda and T. Yanagida, Rational Concept for Reducing Growth Temperature in Vapor-Liquid-Solid Process of Metal Oxide Nanowires, *Nano Lett.*, 2016, **16**, 7495–7502, DOI: **10.1021/acs.nanolett.6b03227**.

107 S. Li, Y. C. Lin, X. Y. Liu, Z. Hu, J. Wu, H. Nakajima, S. Liu, T. Okazaki, W. Chen, T. Minari, Y. Sakuma, K. Tsukagoshi, K. Suenaga, T. Taniguchi and M. Osada, Wafer-scale and deterministic patterned growth of monolayer MoS_2 via vapor-liquid-solid method, *Nanoscale*, 2019, **11**, 16122–16129, DOI: **10.1039/c9nr04612g**.

108 T. Haffner, M. Zeghouane, F. Bassani, P. Gentile, A. Gassenq, F. Chouchane, N. Pauc, E. Martinez, E. Robin, S. David, T. Baron and B. Salem, Growth of $Ge_{1-x}Sn_x$ Nanowires by Chemical Vapor Deposition via Vapor–Liquid–Solid Mechanism Using GeH_4 and $SnCl_4$, *Phys. Status Solidi A*, 2018, 215, DOI: **10.1002/pssa.201700743**.

109 C. W. Pinion, J. D. Christesen and J. F. Cahoon, Understanding the vapor-liquid-solid mechanism of Si nanowire growth and doping to synthetically encode precise nanoscale morphology, *J. Mater. Chem. C*, 2016, **4**, 3890–3897, DOI: **10.1039/c5tc03898g**.

110 H. Anzai, M. Suzuki, K. Nagashima, M. Kanai, Z. Zhu, Y. He, M. Boudot, G. Zhang, T. Takahashi, K. Kanemoto, T. Seki, N. Shibata and T. Yanagida, True Vapor-Liquid-Solid Process Suppresses Unintentional Carrier Doping of Single Crystalline Metal Oxide Nanowires, *Nano Lett.*, 2017, **17**, 4698–4705, DOI: **10.1021/acs.nanolett.7b01362**.

111 X. Xue, Z. Zhou, B. Peng, M. M. Zhu, Y. J. Zhang, W. Ren, Z. G. Ye, X. Chen and M. Liu, Review on nanomaterials synthesized by vapor transport method: growth and their related applications, *RSC Adv.*, 2015, **5**, 79249–79263, DOI: **10.1039/c5ra13349a**.

112 T. Zhang, T. Zhang, R. Zhang, J. Deng, G. Lu and L. Wang, Highly sensitive sensing platform based on $ZnSnO_3$ hollow cubes for detection of ethanol, *Appl. Surf. Sci.*, 2017, **400**, 262–268, DOI: **10.1016/j.apsusc.2016.12.183**.

113 P. T. Lan Huong, N. Tu, H. Lan, L. H. Thang, N. Van Quy, P. A. Tuan, N. X. Dinh, V. N. Phan and A. T. Le, Functional manganese ferrite/graphene oxide nanocomposites: Effects of graphene oxide on the adsorption mechanisms of organic MB dye and inorganic As(v) ions from aqueous solution, *RSC Adv.*, 2018, **8**, 12376–12389, DOI: **10.1039/c8ra00270c**.

114 J. Zhang, L. Fan, J. Li, X. Liu, R. Wang, L. Wang and G. Tu, Growth mechanism of $CsPbBr_3$ perovskite nanocrystals by a co-precipitation method in a CSTR system, *Nano Res.*, 2019, **12**, 121–127, DOI: **10.1007/s12274-018-2190-x**.

115 R. Jiang, Y. Wang, C. Gao, A. Li, Y. Liu, D. Li and J. Zhang, Hollow $ZnSnO_3$ cubes@carbon/reduced graphene oxide ternary composite as anode of lithium ion batteries with enhanced electrochemical performance, *Ceram. Int.*, 2017, **43**, 11556–11562, DOI: **10.1016/j.ceramint.2017.05.031**.

116 S. Dong, L. Cui, W. Zhang, L. Xia, S. Zhou, C. K. Russell, M. Fan, J. Feng and J. Sun, Double-shelled $ZnSnO_3$ hollow cubes for efficient photocatalytic degradation of antibiotic wastewater, *Chem. Eng. J.*, 2020, **384**, 123279, DOI: **10.1016/j.cej.2019.123279**.

117 H. Dong and G. M. Koenig, A review on synthesis and engineering of crystal precursors produced: Via coprecipitation for multicomponent lithium-ion battery cathode materials, *CrystEngComm*, 2020, **22**, 1514–1530, DOI: **10.1039/c9ce00679f**.

118 A. V. Rane, K. Kanny, V. K. Abitha, S. Thomas and S. Thomas, Methods for Synthesis of Nanoparticles and Fabrication of Nanocomposites, in *Synthesis of Inorganic Nanomaterials: Advances and Key Technologies*, Elsevier, 2018, pp. 121–139, DOI: **10.1016/B978-0-08-101975-7.00005-1**.

119 N. S. Bajaj and R. A. Joshi, Energy materials: synthesis and characterization techniques, *Energy Mater.*, 2021, 61–82, DOI: **10.1016/B978-0-12-823710-6.00019-4**.

120 I. V. Tudose, F. Comanescu, P. Pascariu, S. Bucur, L. Rusen, F. Iacomi, E. Koudoumas and M. P. Suchea, Chemical and physical methods for multifunctional nanostructured interface fabrication, Functional Nanostructured Interfaces for Environmental and Biomedical Applications, *Micro Nano Technol.*, 2019, 15–26, DOI: **10.1016/B978-0-12-814401-5.00002-5**.

121 V. S. Kavarthapu, S. A. Graham, P. Manchi, M. V. Paranjape and J. S. Yu, Electrospun $ZnSnO_3$/PVDF-HFP Nanofibrous Triboelectric Films for Efficient Mechanical Energy Harvesting, *Adv. Fiber Mater.*, 2023, DOI: **10.1007/s42765-023-00295-3**.

122 Z. Li, Q. Li, X. Liu, C. Yang and Y. Zhou, Simultaneous photocatalytic removal of heavy metal and organic dye over nitrogen and sulfur co-doped hierarchical $ZnSnO_3$/Zn2SnO4 hollow octahedrons, *Mater. Res. Bull.*, 2022, **156**, DOI: **10.1016/j.materresbull.2022.111980**.

123 Z. Li, Y. Xiong, D. Bi, Q. Liu, C. Yang and J. Zhang, Continuously improved gas-sensing performance of Zn_2SnO_4 porous octahedrons by structure evolution and further $ZnSnO_3$ nanosheets decoration, *J. Alloys Compd.*, 2022, **901**, DOI: **10.1016/j.jallcom.2022.163744**.

124 T. Zhou, T. Zhang, R. Zhang, Z. Lou, J. Deng and L. Wang, Hollow $ZnSnO_3$ Cubes with Controllable Shells Enabling Highly Efficient Chemical Sensing Detection of Formaldehyde Vapors, *ACS Appl. Mater. Interfaces*, 2017, **9**, 14525–14533, DOI: **10.1021/acsami.7b03112**.

125 L. P. Wang, Y. Zhao, C. Wei, C. Wong, M. Srinivasan and Z. J. Xu, Polycrystalline zinc stannate as an anode material for sodium-ion batteries, *J. Mater. Chem. A*, 2015, **3**, 14033–14038, DOI: **10.1039/c5ta02734a**.

126 H. Fan, Y. Zeng, X. Xu, N. Lv and T. Zhang, Hydrothermal synthesis of hollow $ZnSnO_3$ microspheres and sensing properties toward butane, *Sens. Actuators, B*, 2011, **153**, 170–175, DOI: **10.1016/j.snb.2010.10.026**.

127 Y. Bing, Y. Zeng, C. Liu, L. Qiao, Y. Sui, B. Zou, W. Zheng and G. Zou, Assembly of hierarchical $ZnSnO_3$ hollow microspheres from ultra-thin nanorods and the enhanced ethanol-sensing performances, *Sens. Actuators, B*, 2014, **190**, 370–377, DOI: **10.1016/j.snb.2013.08.015**.

128 Y. Zeng, K. Zhang, X. Wang, Y. Sui, B. Zou, W. Zheng and G. Zou, Rapid and selective H_2S detection of hierarchical ZnSnO 3 nanocages, *Sens. Actuators, B*, 2011, **159**, 245–250, DOI: **10.1016/j.snb.2011.06.080**.

129 T. Zhou, T. Zhang, R. Zhang, Z. Lou, J. Deng and L. Wang, Hollow $ZnSnO_3$ Cubes with Controllable Shells Enabling Highly Efficient Chemical Sensing Detection of Formaldehyde Vapors, *ACS Appl. Mater. Interfaces*, 2017, **9**, 14525–14533, DOI: **10.1021/acsami.7b03112**.

130 A. V. Borhade and Y. R. Baste, Study of photocatalytic asset of the $ZnSnO_3$ synthesized by green chemistry, *Arabian J. Chem.*, 2017, **10**, S404–S411, DOI: **10.1016/j.arabjc.2012.10.001**.

131 P. Song, Q. Wang and Z. Yang, Biomorphic synthesis of $ZnSnO_3$ hollow fibers for gas sensing application, *Sens. Actuators, B*, 2011, **156**, 983–989, DOI: **10.1016/j.snb.2011.03.017**.

132 S. Dong, J. Sun, Y. Li, C. Yu, Y. Li and J. Sun, $ZnSnO_3$ hollow nanospheres/reduced graphene oxide nanocomposites as

high-performance photocatalysts for degradation of metronidazole, *Appl. Catal., B*, 2014, **144**, 386–393, DOI: 10.1016/j.apcatb.2013.07.043.

133 T. Zhou, T. Zhang, R. Zhang, Z. Lou, J. Deng and L. Wang, Hollow $ZnSnO_3$ Cubes with Controllable Shells Enabling Highly Efficient Chemical Sensing Detection of Formaldehyde Vapors, *ACS Appl. Mater. Interfaces*, 2017, **9**, 14525–14533, DOI: 10.1021/acsami.7b03112.

134 J. F. Duan, S. C. Hou, S. G. Chen and H. G. Duan, Synthesis of amorphous $ZnSnO_3$ hollow nanoboxes and their lithium storage properties, *Mater. Lett.*, 2014, **122**, 261–264, DOI: 10.1016/j.matlet.2014.02.060.

135 L. Xu, W. Kuang, M. Lai, J. Miao, L. Zhang and R. Zhang, Preparation of Sn-Zn-O thin film for its potential applications in photodegradation of organic dyes, *Mater. Lett.*, 2018, **233**, 42–46, DOI: 10.1016/j.matlet.2018.08.142.

136 Y. Zeng, T. Zhang, H. Fan, G. Lu and M. Kang, Synthesis and gas-sensing properties of $ZnSnO_3$ cubic nanocages and nanoskeletons, *Sens. Actuators, B*, 2009, **143**, 449–453, DOI: 10.1016/j.snb.2009.07.021.

137 J. Zheng, H. Hou, H. Fu, L. Gao and H. Liu, Size-controlled synthesis of porous $ZnSnO_3$ nanocubes for improving formaldehyde gas sensitivity, *RSC Adv.*, 2021, **11**, 20268–20277, DOI: 10.1039/d1ra01852c.

138 Y. T. Wang and K. S. Chang, Piezopotential-Induced Schottky Behavior of $Zn_{1-x}SnO_3$ Nanowire Arrays and Piezophotocatalytic Applications, *J. Am. Ceram. Soc.*, 2016, **99**, 2593–2600, DOI: 10.1111/jace.14264.

139 M. K. Lo, S. Y. Lee and K. S. Chang, Study of $ZnSnO_3$-nanowire piezophotocatalyst using two-step hydrothermal synthesis, *J. Phys. Chem. C*, 2015, **119**, 5218–5224, DOI: 10.1021/acs.jpcc.5b00282.

140 C. Liu, R. Röder, L. Zhang, Z. Ren, H. Chen, Z. Zhang, C. Ronning and P. X. Gao, Highly efficient visible-light driven photocatalysts: A case of zinc stannate based nanocrystal assemblies, *J. Mater. Chem. A*, 2014, **2**, 4157–4167, DOI: 10.1039/c3ta14611a.

141 I. Lee, N. Sung, K. Hwa and R. Conley, Characterization of zinc – tin – oxide films deposited by radio frequency magnetron sputtering at various substrate temperatures, *Thin Solid Films*, 2013, **548**, 385–388, DOI: 10.1016/j.tsf.2013.08.067.

142 Y. Choi, S. J. Kang and H. Kim, Rapid thermal annealing effect on the characteristics of $ZnSnO_3$ films prepared by RF magnetron sputtering, *Curr. Appl. Phys.*, 2012, **12**, 104–107, DOI: 10.1016/j.cap.2012.05.014.

143 C. B. Anucha, I. Altin, E. Bacaksiz, V. N. Stathopoulos, I. Polat, A. Yasar and Ö. F. Yüksel, Silver doped zinc stannate (Ag-$ZnSnO_3$) for the photocatalytic degradation of caffeine under uv irradiation, *Water*, 2021, **13**, 5–7, DOI: 10.3390/w13091290.

144 F. Guo, X. Huang, Z. Chen, H. Sun and W. Shi, Investigation of visible-light-driven photocatalytic tetracycline degradation via carbon dots modified porous $ZnSnO_3$ cubes: Mechanism and degradation pathway, *Sep. Purif. Technol.*, 2020, **253**, 117518, DOI: 10.1016/j.seppur.2020.117518.

145 Y. Ma, R. Jiang, Y. Dong, Y. Liu and J. Zhang, Embedding ultrafine $ZnSnO_3$ nanoparticles into reduced graphene oxide composites as high-performance electrodes for lithium ion batteries, *Biomed. Mater.*, 2020, 0–16, DOI: 10.1088/1361-6528/aab07e.

146 Y. Wang, D. Li, Y. Liu and J. Zhang, Self-assembled 3D $ZnSnO_3$ hollow cubes@reduced graphene oxide aerogels as high capacity anode materials for lithium-ion batteries, *Electrochim. Acta*, 2016, **203**, 84–90, DOI: 10.1016/j.electacta.2016.03.195.

147 R. Guo, R. Tian, D. Shi, H. Li and H. Liu, S-Doped $ZnSnO_3$ Nanoparticles with Narrow Band Gaps for Photocatalytic Wastewater Treatment, *ACS Appl. Nano Mater.*, 2019, **2**, 7755–7765, DOI: 10.1021/acsanm.9b01804.

148 S. Dong, L. Cui, W. Zhang, L. Xia, S. Zhou, C. K. Russell, M. Fan, J. Feng and J. Sun, Double-shelled $ZnSnO_3$ hollow cubes for efficient photocatalytic degradation of antibiotic wastewater, *Chem. Eng. J.*, 2020, **384**, 123279, DOI: 10.1016/j.cej.2019.123279.

149 J. Chen, W. Luo, S. Yu, X. Yang, Z. Wu, H. Zhang, J. Gao, Y. W. Mai, Y. Li and Y. Jia, Synergistic effect of photocatalysis and pyrocatalysis of pyroelectric $ZnSnO_3$ nanoparticles for dye degradation, *Ceram. Int.*, 2020, **46**, 9786–9793, DOI: 10.1016/j.ceramint.2019.12.251.

150 A. Biswas, S. Saha and N. R. Jana, $ZnSnO_3$ Nanoparticle-Based Piezocatalysts for Ultrasound-Assisted Degradation of Organic Pollutants, *ACS Appl. Nano Mater.*, 2019, **2**, 1120–1128, DOI: 10.1021/acsanm.9b00107.

151 M. Najam Khan and J. Dutta, Comparison of photocatalytic activity of zinc stannate particles and zinc stannate/zinc oxide composites for the removal of phenol from water, and a study on the effect of pH on photocatalytic efficiency, *Mater. Sci. Semicond. Process.*, 2015, **36**, 124–133, DOI: 10.1016/j.mssp.2015.03.011.

152 S. N. Habisreutinger, L. Schmidt-Mende and J. K. Stolarczyk, Photocatalytic reduction of CO_2 on TiO_2 and other semiconductors, *Angew. Chem., Int. Ed.*, 2013, **52**, 7372–7408, DOI: 10.1002/anie.201207199.

153 G. Venkatesh, N. Elavarasan, M. Srinivasan, G. Palanisamy, R. R. Macadangdang, S. Vignesh, P. Ramasamy, H. E. Ali, M. Shkir and Z. Ahmad, Z-scheme heterojunction $ZnSnO_3/rGO/MoS_2$ nanocomposite for excellent photocatalytic activity towards mixed dye degradation, *Int. J. Hydrogen Energy*, 2022, **47**, 11863–11876, DOI: 10.1016/j.ijhydene.2022.01.240.

154 S. Dong, L. Xia, X. Chen, L. Cui, W. Zhu, Z. Lu, J. Sun and M. Fan, Interfacial and electronic band structure optimization for the adsorption and visible-light photocatalytic activity of macroscopic $ZnSnO_3$/graphene aerogel, *Composites, Part B*, 2021, **215**, 108765, DOI: 10.1016/j.compositesb.2021.108765.

155 F. Chen, Q. Yang, C. Niu, X. Li, C. Zhang, J. Zhao, Q. Xu, Y. Zhong, Y. Deng and G. Zeng, Enhanced visible light photocatalytic activity and mechanism of $ZnSn(OH)_6$ nanocubes modified with AgI nanoparticles, *Catal. Commun.*, 2016, **73**, 1–6, DOI: 10.1016/j.catcom.2015.10.003.

156 X. Huang, F. Guo, M. Li, H. Ren, Y. Shi and L. Chen, Hydrothermal synthesis of $ZnSnO_3$ nanoparticles decorated on g-C_3N_4 nanosheets for accelerated photocatalytic degradation of tetracycline under the visible-light irradiation, *Sep. Purif. Technol.*, 2020, **230**, 115854, DOI: **10.1016/j.seppur.2019.115854**.

157 X. Zhu, F. Guo, J. Pan, H. Sun, L. Gao, J. Deng, X. Zhu and W. Shi, Fabrication of visible-light-response face-contact $ZnSnO_3$@g-C_3N_4 core–shell heterojunction for highly efficient photocatalytic degradation of tetracycline contaminant and mechanism insight, *J. Mater. Sci.*, 2021, **56**, 4366–4379, DOI: **10.1007/s10853-020-05542-1**.

158 F. Guo, X. Huang, Z. Chen, L. Cao, X. Cheng, L. Chen and W. Shi, Construction of Cu_3P-$ZnSnO_3$-g-C_3N_4 p-n-n heterojunction with multiple built-in electric fields for effectively boosting visible-light photocatalytic degradation of broad-spectrum antibiotics, *Sep. Purif. Technol.*, 2021, **265**, 118477, DOI: **10.1016/j.seppur.2021.118477**.

159 Z. Chen, X. Chu, X. Huang, H. Sun, L. Chen and F. Guo, Fabrication of visible-light driven CoP/$ZnSnO_3$ composite photocatalyst for high-efficient photodegradation of antibiotic pollutant, *Sep. Purif. Technol.*, 2021, **257**, 117900, DOI: **10.1016/j.seppur.2020.117900**.

160 J. Pan, F. Guo, H. Sun, Y. Shi and W. Shi, Nanodiamonds anchored on porous $ZnSnO_3$ cubes as an efficient composite photocatalyst with improved visible-light photocatalytic degradation of tetracycline, *Sep. Purif. Technol.*, 2021, **263**, 118398, DOI: **10.1016/j.seppur.2021.118398**.

161 D. Kohl, *Function and applications of gas sensors*, 2001. **http://iopscience.iop.org/0022-3727/34/19/201**.

162 Z. Xiao, L. B. Kong, S. Ruan, X. Li, S. Yu, X. Li, Y. Jiang, Z. Yao, S. Ye, C. Wang, T. Zhang, K. Zhou and S. Li, Recent development in nanocarbon materials for gas sensor applications, *Sens. Actuators, B*, 2018, **274**, 235–267, DOI: **10.1016/j.snb.2018.07.040**.

163 S. Gupta Chatterjee, S. Chatterjee, A. K. Ray and A. K. Chakraborty, Graphene-metal oxide nanohybrids for toxic gas sensor: A review, *Sens. Actuators, B*, 2015, **221**, 1170–1181, DOI: **10.1016/j.snb.2015.07.070**.

164 S. S. Varghese, S. Lonkar, K. K. Singh, S. Swaminathan and A. Abdala, Recent advances in graphene based gas sensors, *Sens. Actuators, B*, 2015, **218**, 160–183, DOI: **10.1016/j.snb.2015.04.062**.

165 W. Guo, T. Liu, W. Yu, L. Huang, Y. Chen and Z. Wang, Rapid selective detection of formaldehyde by hollow $ZnSnO_3$ nanocages, *Phys. E*, 2013, **48**, 46–52, DOI: **10.1016/j.physe.2012.11.021**.

166 L. Jiang, Z. Chen, Q. Cui, S. Xu and F. Tang, Experimental and DFT-D3 study of sensitivity and sensing mechanism of $ZnSnO_3$ nanosheets to C_3H_6O gas, *J. Mater. Sci.*, 2022, **57**, 3231–3251, DOI: **10.1007/s10853-021-06855-5**.

167 Y. Yin, F. Li, N. Zhang, S. Ruan, H. Zhang and Y. Chen, Improved gas sensing properties of silver-functionalized $ZnSnO_3$ hollow nanocubes, *Inorg. Chem. Front.*, 2018, **5**, 2123–2131, DOI: **10.1039/c8qi00470f**.

168 M. ul Haq, Z. Zhang, X. Chen, N. Rahman, S. Khan, R. Khatoon, S. S. Hassan, Z. Ye and L. Zhu, A two-step synthesis of microsphere-decorated fibers based on NiO/$ZnSnO_3$ composites towards superior ethanol sensitivity performance, *J. Alloys Compd.*, 2019, **777**, 73–83, DOI: **10.1016/j.jallcom.2018.10.361**.

169 Q. Chen, Y. Wang, M. Wang, S. Ma, P. Wang, G. Zhang, W. Chen, H. Jiao, L. Liu and X. Xu, Enhanced acetone sensor based on Au functionalized In-doped $ZnSnO_3$ nanofibers synthesized by electrospinning method, *J. Colloid Interface Sci.*, 2019, **543**, 285–299, DOI: **10.1016/j.jcis.2019.02.055**.

170 X. Wang, B. Ding, Y. Liu, X. Zhu, H. Li, M. Xia, H. Fu and M. Li, Synthesis of 3D flower-like $ZnSnO_3$ and improvement of ethanol-sensing properties at room temperature based on nano-TiO_2 decoration and UV radiation, *Sens. Actuators, B*, 2018, **264**, 119–127, DOI: **10.1016/j.snb.2018.02.178**.

171 W. Guo, B. Zhao, M. Fu, C. Wang and R. Peng, One pot synthesis of hierarchical and porous $ZnSnO_3$ nanocubes and gas sensing properties to formaldehyde, *Results Phys.*, 2019, **15**, 102606, DOI: **10.1016/j.rinp.2019.102606**.

172 S. Yu, X. Jia, J. Yang, S. Wang, Y. Li and H. Song, Highly sensitive and low detection limit of ethanol gas sensor based on CeO_2 nanodot-decorated $ZnSnO_3$ hollow microspheres, *Ceram. Int.*, 2022, DOI: **10.1016/j.ceramint.2022.02.023**.

173 S. Yu, X. Jia, J. Yang, S. Wang, Y. Li and H. Song, Highly sensitive ethanol gas sensor based on CuO/$ZnSnO_3$ heterojunction composites, *Mater. Lett.*, 2021, **291**, 129531, DOI: **10.1016/j.matlet.2021.129531**.

174 Y. Yin, Y. Shen, S. Zhao, J. Bai, Y. Qi, C. Han and D. Wei, Effect of noble metal elements on ethanol sensing properties of $ZnSnO_3$ nanocubes, *J. Alloys Compd.*, 2021, **887**, 161409, DOI: **10.1016/j.jallcom.2021.161409**.

175 D. Wang, X. Pu, X. Yu, L. Bao, Y. Cheng, J. Xu, S. Han, Q. Ma and X. Wang, Controlled preparation and gas sensitive properties of two-dimensional and cubic structure $ZnSnO_3$, *J. Colloid Interface Sci.*, 2022, **608**, 1074–1085, DOI: **10.1016/j.jcis.2021.09.167**.

176 L. Du, Y. Li, Y. Tong and M. Zhang, Biotemplates based preparation of hierarchical $ZnSnO_3$ porous nanostructures for fast detection of formaldehyde, *Ceram. Int.*, 2021, **47**, 13139–13146, DOI: **10.1016/j.ceramint.2021.01.178**.

177 J. Huang, X. Xu, C. Gu, W. Wang, B. Geng, Y. Sun and J. Liu, Size-controlled synthesis of porous $ZnSnO_3$ cubes and their gas-sensing and photocatalysis properties, *Sens. Actuators, B*, 2012, **171–172**, 572–579, DOI: **10.1016/j.snb.2012.05.036**.

178 L. Wang, T. Zhou, R. Zhang, Z. Lou, J. Deng and T. Zhang, Comparison of toluene sensing performances of zinc stannate with different morphology-based gas sensors, *Sens. Actuators, B*, 2016, **227**, 448–455, DOI: **10.1016/j.snb.2015.12.097**.

179 L. Jiang, K. Xue, Z. Chen, Q. Cui and S. Xu, Hydrothermal synthesis of $ZnSnO_3$/rGO composite material and highly

gas sensing performance to acetone, *Mater. Sci. Semicond. Process.*, 2021, **134**, DOI: **10.1016/j.mssp.2021.106051**.

180 J. Zhang, X. Jia, D. Lian, J. Yang, S. Wang, Y. Li and H. Song, Enhanced selective acetone gas sensing performance by fabricating $ZnSnO_3/SnO_2$ concave microcube, *Appl. Surf. Sci.*, 2021, **542**, DOI: **10.1016/j.apsusc.2020.148555**.

181 Q. Chen, S. Y. Ma, H. Y. Jiao, G. H. Zhang, H. Chen, X. L. Xu, H. M. Yang and Z. Qiang, Synthesis of novel $ZnSnO_3$ hollow polyhedrons with open nanoholes: Enhanced acetone-sensing performance, *Ceram. Int.*, 2017, **43**, 1617–1621, DOI: **10.1016/j.ceramint.2016.10.094**.

182 Z. Wang, J. Miao, H. Zhang, D. Wang and J. Sun, Hollow cubic $ZnSnO_3$ with abundant oxygen vacancies for H_2S gas sensing, *J. Hazard. Mater.*, 2020, **391**, 122226, DOI: **10.1016/j.jhazmat.2020.122226**.

183 K. Liu, Z. Zheng, J. Xu and C. Zhang, Enhanced visible light-excited $ZnSnO_3$ for room temperature ppm-level CO_2 detection, *J. Alloys Compd.*, 2022, **907**, 164440, DOI: **10.1016/j.jallcom.2022.164440**.

184 L. Du, D. Wang, K. Gu and M. Zhang, Construction of PdO-decorated double-shell $ZnSnO_3$ hollow microspheres for: N-propanol detection at low temperature, *Inorg. Chem. Front.*, 2021, **8**, 787–795, DOI: **10.1039/d0qi01292k**.

185 G. Feng, Y. Che, C. Song, J. Xiao, X. Fan, S. Sun, G. Huang and Y. Ma, Morphology-controlled synthesis of $ZnSnO_3$ hollow spheres and their n-butanol gas-sensing performance, *Ceram. Int.*, 2021, **47**, 2471–2482, DOI: **10.1016/j.ceramint.2020.09.090**.

186 P. Shi, Z.-H. Fu, M.-Y. Zhou, X. Chen, N. Yao, L.-P. Hou, C.-Z. Zhao, B.-Q. Li, J.-Q. Huang, X.-Q. Zhang and Q. Zhang, *Inhibiting intercrystalline reactions of anode with electrolytes for long-cycling lithium batteries*, 2022. **https://www.science.org**.

187 Z. Y. Zhang, Z. W. Li, Q. Luo, B. Z. Yang, Y. Liu, Y. Y. Hu, X. Bin Liu, Y. H. Yin, Y. S. Li and Z. P. Wu, Spontaneous nanominiaturization of silicon microparticles with structural stability as flexible anodes for lithium ion batteries, *Carbon*, 2022, **188**, 238–245, DOI: **10.1016/j.carbon.2021.11.059**.

188 X. Li, G. Guan, C. Yu, B. Cheng, X. Chen, K. Zhang and J. Xiang, Enhanced electrochemical performances based on $ZnSnO_3$ microcubes functionalized in-doped carbon nanofibers as free-standing anode materials, *Dalton Trans.*, 2023, DOI: **10.1039/D3DT01642K**.

189 K. Wang, S. Zhang, Z. Hou, L. Wang, P. An, J. Jia, Y. Li and P. Zhang, Nanofibrous $ZnSnO_3$/C composite derived from natural cellulose substance as an enhanced lithium-ion battery anode, *Mater. Lett.*, 2023, **331**, DOI: **10.1016/j.matlet.2022.133435**.

190 Y. Chen, B. Qu, L. Mei, D. Lei, L. Chen, Q. Li and T. Wang, Synthesis of $ZnSnO_3$ mesocrystals from regular cube-like to sheet-like structures and their comparative electrochemical properties in Li-ion batteries, *J. Mater. Chem.*, 2012, **22**, 25373–25379, DOI: **10.1039/c2jm33123c**.

191 X. Chen, Y. Huang, H. Huang, M. Wang and K. Wang, Silver-modified hollow $ZnSnO_3$ boxes as high capacity anode materials for Li-ion batteries, *Mater. Lett.*, 2015, **149**, 33–36, DOI: **10.1016/j.matlet.2015.02.060**.

192 Q. Xie, Y. Ma, X. Zhang, H. Guo, A. Lu, L. Wang, G. Yue and D. L. Peng, Synthesis of amorphous $ZnSnO_3$-C hollow microcubes as advanced anode materials for lithium ion batteries, *Electrochim. Acta*, 2014, **141**, 374–383, DOI: **10.1016/j.electacta.2014.07.095**.

193 Y. Ma, R. Jiang, D. Li, Y. Dong, Y. Liu and J. Zhang, Embedding ultrafine $ZnSnO_3$ nanoparticles into reduced graphene oxide composites as high-performance electrodes for lithium ion batteries, *Nanotechnology*, 2018, **29**, DOI: **10.1088/1361-6528/aab07e**.

194 P. Luo, H. Zhang, L. Liu, L. Fang and Y. Wang, Sandwich-like nanostructure of amorphous $ZnSnO_3$ encapsulated in carbon nanosheets for enhanced lithium storage, *Electrochim. Acta*, 2016, **219**, 734–741, DOI: **10.1016/j.electacta.2016.10.085**.

195 Y. Ma, Q. Xie, X. Liu, Y. Zhao, D. Zeng, L. Wang, Y. Zheng and D. L. Peng, Synthesis of amorphous $ZnSnO_3$ double-shell hollow microcubes as advanced anode materials for lithium ion batteries, *Electrochim. Acta*, 2015, **182**, 327–333, DOI: **10.1016/j.electacta.2015.09.102**.

196 F. Han, W. Li, C. Lei, B. He, K. Oshida and A. Lu, Selective Formation of Carbon-Coated, Metastable Amorphous $ZnSnO_3$ Nanocubes Containing Mesopores for Use as High-Capacity Lithium-Ion Battery, *Small*, 2014, **10**, 1–8, DOI: **10.1002/smll.201400371**.

197 H. Tan, H. W. Cho and J. J. Wu, Binder-free ZnO@$ZnSnO_3$ quantum dots core-shell nanorod array anodes for lithium-ion batteries, *J. Power Sources*, 2018, **388**, 11–18, DOI: **10.1016/j.jpowsour.2018.03.066**.

198 Y. L. Qin, F. F. Zhang, X. C. Du, G. Huang, Y. C. Liu and L. M. Wang, Controllable synthesis of cube-like $ZnSnO_3$@TiO_2 nanostructures as lithium ion battery anodes, *J. Mater. Chem. A*, 2015, **3**, 2985–2990, DOI: **10.1039/c4ta06055e**.

199 C. K. Sim, S. R. Majid and N. Z. Mahmood, $ZnSnO_3$/mesoporous biocarbon composite towards sustainable electrode material for energy storage device, *Microchem. J.*, 2021, **164**, 105968, DOI: **10.1016/j.microc.2021.105968**.

200 Y. Wang, D. Li, Y. Liu and J. Zhang, Fabrication of novel rugby-like $ZnSnO_3$/reduced graphene oxide composites as a high-performance anode material for lithium-ion batteries, *Mater. Lett.*, 2016, **167**, 222–225, DOI: **10.1016/j.matlet.2015.12.107**.

201 M. Jiang, J. Wu, H. Guo, H. Zhang, M. Zhu and X. Xu, Controlled synthesis of cube-like $ZnSnO_3$ decorated by nickel-based films and electrochemical applications on lithium-sulfur batteries, *Compos. Interfaces*, 2022, 1–12, DOI: **10.1080/09276440.2022.2044108**.

202 Q. Xie, Y. Ma, X. Zhang, H. Guo, A. Lu, L. Wang, G. Yue and D. L. Peng, Synthesis of amorphous $ZnSnO_3$-C hollow microcubes as advanced anode materials for lithium ion batteries, *Electrochim. Acta*, 2014, **141**, 374–383, DOI: **10.1016/j.electacta.2014.07.095**.

203 R. Jiang, Y. Wang, C. Gao, A. Li, Y. Liu, D. Li and J. Zhang, Hollow $ZnSnO_3$ cubes@carbon/reduced graphene oxide

ternary composite as anode of lithium ion batteries with enhanced electrochemical performance, *Ceram. Int.*, 2017, **43**, 11556–11562, DOI: 10.1016/j.ceramint.2017.05.031.

204 X. Chen, Y. Huang, H. Huang, M. Wang and K. Wang, Silver-modified hollow $ZnSnO_3$ boxes as high capacity anode materials for Li-ion batteries, *Mater. Lett.*, 2015, **149**, 33–36, DOI: 10.1016/j.matlet.2015.02.060.

205 A. Rovisco, A. Dos Santos, T. Cramer, J. Martins, R. Branquinho, H. Águas, B. Fraboni, E. Fortunato, R. Martins, R. Igreja and P. Barquinha, Piezoelectricity Enhancement of Nanogenerators Based on PDMS and $ZnSnO_3$ Nanowires through Microstructuration, *ACS Appl. Mater. Interfaces*, 2020, **12**, 18421–18430, DOI: 10.1021/acsami.9b21636.

206 Z. L. Wang and J. Song, Piezoelectric nanogenerators based on zinc oxide nanowire arrays, *Science*, 2006, **312**, 242–246, DOI: 10.1126/science.1124005.

207 R. Guo, Y. Guo, H. Duan, H. Li and H. Liu, Synthesis of Orthorhombic Perovskite-Type $ZnSnO_3$ Single-Crystal Nanoplates and Their Application in Energy Harvesting, *ACS Appl. Mater. Interfaces*, 2017, **9**, 8271–8279, DOI: 10.1021/acsami.6b16629.

208 C. Cheng, U. J. Jung, W. Heo, W. Park and J. Park, Enhanced piezoelectric performance of $ZnSnO_3$@PVDF composite films by control of embedded contents of $ZnSnO_3$ nanoparticles, *Surf. Interfaces*, 2023, **41**, DOI: 10.1016/j.surfin.2023.103177.

209 Y. Fu, Y. Nie, Y. Zhao, P. Wang, L. Xing, Y. Zhang and X. Xue, Detecting liquefied petroleum gas (LPG) at room temperature using $ZnSnO_3$/ZnO nanowire piezo-nanogenerator as self-powered gas sensor, *ACS Appl. Mater. Interfaces*, 2015, **7**, 10482–10490, DOI: 10.1021/acsami.5b01822.

210 J. M. Wu, K. H. Chen, Y. Zhang and Z. L. Wang, A self-powered piezotronic strain sensor based on single $ZnSnO_3$ microbelts, *RSC Adv.*, 2013, **3**, 25184–25189, DOI: 10.1039/c3ra45027a.

211 A. Datta, D. Mukherjee, C. Kons, S. Witanachchi and P. Mukherjee, Evidence of superior ferroelectricity in structurally welded $ZnSnO_3$ nanowire arrays, *Small*, 2014, **10**, 4093–4099, DOI: 10.1002/smll.201401249.

212 S. M. A. Z. Shawon, Z. D. Carballo, V. S. Vega, C. Lin, M. S. Rafaqut, A. X. Sun, J. J. Li and M. J. Uddin, Surface modified hybrid $ZnSnO_3$ nanocubes for enhanced piezoelectric power generation and wireless sensory application, *Nano Energy*, 2022, **92**, 106653, DOI: 10.1016/j.nanoen.2021.106653.

213 P. Manchi, S. A. Graham, H. Patnam, M. V. Paranjape and J. S. Yu, rGO-$ZnSnO_3$ Nanostructure-Embedded Triboelectric Polymer-Based Hybridized Nanogenerators, *Adv. Mater. Technol.*, 2022, 2101460, DOI: 10.1002/admt.202101460.

214 K. Y. Lee, D. Kim, J. H. Lee, T. Y. Kim, M. K. Gupta and S. W. Kim, Unidirectional high-power generation via stress-induced dipole alignment from $ZnSnO_3$ nanocubes/polymer hybrid piezoelectric nanogenerator, *Adv. Funct. Mater.*, 2014, **24**, 37–43, DOI: 10.1002/adfm.201301379.

215 S. Paria, S. K. Karan, R. Bera, A. K. Das, A. Maitra and B. B. Khatua, A Facile Approach to Develop a Highly Stretchable PVC/$ZnSnO_3$ Piezoelectric Nanogenerator with High Output Power Generation for Powering Portable Electronic Devices, *Ind. Eng. Chem. Res.*, 2016, **55**, 10671–10680, DOI: 10.1021/acs.iecr.6b02172.

216 S. Paria, S. Ojha, S. K. Karan, S. K. Si, R. Bera, A. K. Das, A. Maitra, L. Halder, A. De and B. B. Khatua, Approach for Enhancement in Output Performance of Randomly Oriented $ZnSnO_3$ Nanorod-Based Piezoelectric Nanogenerator via p–n Heterojunction and Surface Passivation Layer, *ACS Appl. Electron. Mater.*, 2020, **2**, 2565–2578, DOI: 10.1021/acsaelm.0c00467.

217 S. N. Habisreutinger, L. Schmidt-Mende and J. K. Stolarczyk, Photocatalytic reduction of CO_2 on TiO_2 and other semiconductors, *Angew. Chem., Int. Ed.*, 2013, **52**, 7372–7408, DOI: 10.1002/anie.201207199.

218 D. Lian, B. Shi, R. Dai, X. Jia and X. Wu, Synthesis and enhanced acetone gas-sensing performance of $ZnSnO_3$/SnO_2 hollow urchin nanostructures, *J. Nanopart. Res.*, 2017, **19**, DOI: 10.1007/s11051-017-4094-1.